UNIVERSITY OF CALIFORNIA
RIVERSIDE

Bio-Resorbable Magnesium-Based Biomaterials for Neural and Orthopedic Applications

A Dissertation submitted in partial satisfaction
of the requirements for the degree of

Doctor of Philosophy

in

Materials Science and Engineering

by

Chaoxing Zhang

March 2020

Dissertation Committee:
Dr. Huinan Liu, Chairperson
Dr. Pingyun Feng
Dr. Hyle Park

The Dissertation of Chaoxing Zhang is approved:

_____

_____

_____

Committee Chairperson

University of California, Riverside

Acknowledgements

Firstly, I would like to thank my PhD advisor, Dr. Huinan Liu for her continuous support and guidance on my PhD study. I also want to thank the rest of committee, Dr. Pingyun Feng and Dr. Hyle Park, for their insightful and professional feedback on my dissertation. My sincere thanks also go to my colleagues in Liu lab, Dr. Qiaomu Tian, Dr. Naiyin Zhang, Dr. Wensen Jiang, Nhu Nguyen, Jiajia Lin and Changlu Xu for their kind help on my research. Specially, I want to thank my best friend in Liu lab, the visiting scholar from Peking University, Wenhao Zhou. We have built a deep friendship even he just stayed here for only one year. A confidant in a foreign country keeps me from being alone.

I want to send my sincere thanks to my whole family for their support during my PhD study. My mother chats with me every week since she always cares about my studies and life and I can feel how much she loves me. My father is not good at expressing emotions but he is the backing I can count on to overcome difficulties. My sister guides me forward since I was a child and I couldn't come to this step without her. All other family members also give me unbelievable support and I am so lucky and proud of being a member of such a wonderful family and I love all of you forever.

Also, I want to especially thank my dearest friends in junior high school, Rong Xu, Jiamin Wang, Xuewei Jia and Yifeng Xue, in high school, Song Zhang, Kai Zhao, Yifeng Li, Bintao Wang, Bingtao Zhang, Kangshun Zhang, Ze Zhang, Guosheng Zhang, Lei Duan and Zhuo Zhang and in college, Zhengtao Tian, Hongbo Zhang and Tongda Li, for without the support from all of you all my voyage in the sea of science will never be possible.

Lastly, I would like to give my greatest thanks to the unique one in my life, my princess, my love, my soul mate, my fiancée, Tianrui Yang. We came to the US together in 2015 to pursue higher education. We always support each other, encourage each other, help each other and love each other to face everything together. I am so lucky to know you, be familiar with you, understand you and be with you. Our true love will last forever.

The text of this dissertation, in part or in full, is a reprint of the material as it appears in "Electrochemical deposition of conductive polymers onto magnesium microwires for neural electrode applications. Journal of Biomedical Materials Research Part A 106.7 (2018): 1887-1895.", "Magnesium-based biodegradable microelectrodes for neural recording. Materials Science and Engineering: C (2020): 110614.", "Antimicrobial Bioresorbable Mg–Zn–Ca Alloy for Bone Repair in a Comparison Study with Mg–Zn–Sr Alloy and Pure Mg. ACS Biomaterials Science & Engineering (2019).". The co-authors listed in these three publications directed and supervised the research which forms the basis for this dissertation.

I would like to acknowledge financial support from the U.S. National Institutes of Health (NIAMS award 1R03AR069373), U.S. National Science Foundation (CBET award 1512764, 1125801), Burroughs Wellcome Fund (1011235), Hellman Faculty Fellowship (H.L.), and the University of California (UC) Regents Faculty Development Award (H.L.). The authors thank the California Alliance for Minority Participation (CAMP) program and Materials Connection (MaCREU) program (NSF DMR award 1359136) at the UCR for supporting the undergraduate student researcher (E.V.).

ABSTRACT OF THE DISSERTATION

Bio-Resorbable Magnesium-Based Biomaterials for Neural and Orthopedic Applications

by

Chaoxing Zhang

Doctor of Philosophy, Graduate Program in Materials Science and Engineering
University of California, Riverside, March 2020
Dr. Huinan Liu, Chairperson

Magnesium (Mg)-based biomaterials have attracted increasing attention in biomedical applications, such as neural and orthopedic applications because of the biocompatibility, biodegradability, antibacterial properties, and excellent mechanical properties. However, rapid degradation of Mg is the major concern for many clinical applications. To address the challenge, the present dissertation developed the two approaches, including engineering proper surfaces and alloying Mg with other elements to control the degradation of Mg-based biomaterials and enhance the overall performances of Mg for neural and orthopedic applications. The first part of the dissertation developed a method to deposit a conductive polymer coating, poly(3,4-ethylenedioxythiophene) (PEDOT) onto the surface of Mg microwire for potential neural recording and stimulation applications. The optimized parameters were found for the first time. It was found that the corrosion rate of PEDOT-coated Mg microwire was much slower than the non-coated Mg microwire. The second part of the research reported the fabrication, characterization, degradation and electrical properties of biodegradable magnesium (Mg) microwires coated with two functional polymers, and the first *in vivo* evidence on the feasibility

of Mg-based biodegradable microelectrodes for neural recording. The third part of the dissertation developed biocompatible, biodegradable Magnesium-zinc-calcium (Mg–Zn–Ca) alloys with similar mechanical properties to human bone for orthopedic applications. The objectives were to characterize Mg–2wt.% Zn–0.5 wt.% Ca (named ZC21) alloy pins microstructurally and mechanically, and determine their degradation and interactions with host cells and pathogenic bacteria *in vitro* and *in vivo*. Overall, the entire dissertation provided extensive knowledge regarding engineering proper surfaces and alloying Mg with other elements towards desired performances for neural and orthopedic applications.

Table of Contents

List of Figures

Introduction

Magnesium (Mg)-based biomaterials provide attractive properties for biomedical applications, such as orthopaedic [1, 4], cardiovascular [5], urological [6] and neural applications [7, 8]. In the human body, Mg reacts with water and naturally degrades, which eliminates the necessity of a secondary removal procedure for an implant [9]. The degradation products of Mg, i.e. Mg^{2+} ions, could activate or catalyse over 300 kinds of enzymes and are needed for many metabolic processes in the human body [5]. For orthopaedic device applications, Mg^{2+} ions could promote bone growth by accelerating the adhesion of bone cells to apatite [3]. Moreover, the density and mechanical properties of Mg are closer to those of cortical bone [10], which could reduce the stress-shielding associated issues and improve bone healing [11]. Excellent biodegradability, biocompatibility and mechanical properties also make Mg a good candidate material for cardiovascular stents. Furthermore, Mg alloys showed attractive antimicrobial properties for ureteral stent application [6]. Lastly, Mg could be used as an electrode material for neural recording and stimulation applications because of its conductivity and neuro-protective effect of Mg^{2+} ions [7].

However, the application of Mg-based materials as biomedical implants is limited by their corrosion behaviour [12-14]. The rapid degradation of Mg causes local pH increase and H_2 release in a short time after implantation and possible premature mechanical failure of the implants [15]. Thus, it is critical to improve the degradation behaviour of Mg-based materials for their potential biomedical applications [16, 17]. Generally, there are two ways to achieve the goal: (1) alloying and processing [18]; (2) surface treatments or coatings [9, 15, 19, 20].

The first part and second part of the dissertation focus on Mg-based microelectrodes for neural applications. Two functional polymers, specifically, conductive poly-3,4-

ethylenedioxythiophene (PEDOT) and insulating poly(glycerol sebacate) (PGS), were deposited onto Mg microwire substrates to create biodegradable, biocompatible, and implantable microelectrodes. The objectives of the study were to investigate the electrical properties, degradation and neural recording capability of Mg-based microelectrodes *in vitro* and *in vivo*. This is the first report on the feasibility of Mg-based biodegradable implantable electrodes for neural recording inside the brain. This study first demonstrated the capability of Mg-based microelectrode in recording multi-unit stimulus-evoked activity and spontaneous activity in auditory cortex *in vivo*.

The objectives of third part are to determine the degradation of Mg–2wt.% Zn–0.5 wt.% Ca (named ZC21) alloy pins, and their interactions with host cells and pathogenic bacteria *in vitro* and *in vivo* for orthopedic applications. To our knowledge, this is the first comparison study on characterization, mechanical properties, degradation behaviours, antibacterial properties, and biocompatibility of a promising Mg-Zn-Ca alloy *in vitro* and *in vivo*, which provides a comprehensive picture on the potential of Mg-Zn-Ca alloys for clinical translation.

Chapter 1 Electrochemical Deposition of Conductive Polymers onto Magnesium Microwires for Neural Electrode Applications

Abstract

Metals are widely used in electrode design for recording neural activities because of their excellent electrical conductivity and mechanical strength. However, there are still serious problems related to these currently used metallic electrodes, including tissue damage due to the mechanical mismatch between metals and neural tissues, fibrosis, and electrode fouling and encapsulation that lead to the loss of signal and eventual failure. In this study, a biocompatible, biodegradable, and conductive electrode was created. Specifically, pure magnesium (Mg) microwire with a diameter of 127 μm was used as the electrode substrate and the conductive polymer, i.e., poly(3,4-ethylenedioxythiophene) (PEDOT), was electrochemically deposited onto Mg microwires to decrease corrosion rate and improve biocompatibility of the electrodes for potential neural electrode applications. Both chronopotentiometry and cyclic voltammetry (CV) methods and the associated parameters for electrochemical deposition of PEDOT onto Mg microwires were investigated, such as deposition current, deposition temperature, voltage, sweep rate, cycle number and duration. The CV method from -2.0 V to 1.25 V for 1 cycle at a cycle duration of 600 s with a sweep rate of 5 mV/s at 65°C led to a consistent, uniform and complete PEDOT coating on Mg microwires. The surface conditions of Mg microwires also affected the quality of PEDOT coating. The corrosion rate of PEDOT-coated Mg microwire was 0.75 mm/year, much slower than the non-coated Mg microwire that showed a corrosion rate of 1.78 mm/year. The optimal Mg microwires with PEDOT coating could potentially serve as biodegradable electrodes for neural recording and stimulation applications.

1.1 Introduction

Neural electrodes have been widely used for monitoring neural signals such as electroencephalography (EEG), and for delivering electrical stimulation to treat injuries and disorders. Current electrodes are mostly fabricated from stiff inert conductive metals, including platinum (Pt) and stainless steel (SS) [21, 22]. In clinical practice, one key challenge related to the use of neural electrodes is to minimize damage to neural tissue [21, 23, 24], which is even more important for the implantable neural electrodes than surface electrodes. However, tissue damage and fibrosis often occur because of the mechanical mismatch between currently used metals and neural tissues. Moreover, biofouling of current implantable electrodes often leads to the loss of signal and electrode failure [21, 22, 25]. Additionally, for electrodes made from bioinert metals such as Pt and SS, secondary surgeries are required for their removal if failure occurs. Therefore, there is a clinical need for conductive, biodegradable and biocompatible electrodes for neural recording and stimulation.

In recent years, magnesium (Mg) has attracted increasing attention for medical implant applications, especially for bone repair because of its biodegradability and similar mechanical properties to cortical bone [26-29]. Pure Mg has an electrical conductivity of 22×10^6 S/m and Mg^{2+} ions could provide neuro-protective effect [30, 31]; and thus, Mg has also been explored for neural implant applications [32, 33]. However, in aqueous physiological environment, rapid degradation of Mg may cause an undesirable increase in local pH and accumulation of hydrogen (H_2) gas [27]. Therefore, it is necessary to perform surface treatment on Mg to moderate its degradation in order to satisfy the clinical requirement. A conductive polymer coating can potentially reduce the rate of Mg degradation and improve its biocompatibility, while retaining the conductivity. Poly(3,4-ethylenedioxythiophene) (PEDOT) is a conductive polymer which has been widely studied for neural applications due to its biocompatibility and electrical conductivity

[32, 34-40]. Moreover, the Young's modulus (E) of PEDOT (E_{PEDOT} = 1-5GPa [41]) is much lower than the Young's modulus of Mg (E_{Mg} = 41-45GPa [42]), suggesting that deposition of PEDOT onto Mg surface could potentially reduce the mechanical mismatch at the interface of electrode and neural tissue and thus reduce trauma. Therefore, PEDOT coated Mg could potentially combine the beneficial properties of Mg and PEDOT for neural electrode applications [32].

In our previous study, PEDOT coating was successfully deposited onto a Mg plate with a dimension of 5 mm × 5 mm × 250 μm using electrochemical deposition method; and the effects of some key parameters on PEDOT deposition, e.g., chronoamperometry versus cyclic voltammetry (CV), Pt versus SS as the counter electrode, and pristine versus recycled 3,4-ethylenedioxythiophene (EDOT, monomer form of PEDOT) in the electrolyte bath, were investigated [32]. Moreover, PEDOT-coated Mg showed slower degradation and improved cytocompatibility when compared with non-coated Mg [33]. However, optimal deposition parameters for achieving uniform and dense PEDOT coating on Mg-based microelectrodes are still unknown. Therefore, the objectives of this study were to optimize the key parameters for electrochemically depositing PEDOT onto Mg microwires with a diameter of 127 μm and to create a prototype of biodegradable microelectrodes using PEDOT-coated Mg microwires for potential neural recording or simulation *in vivo*.

1.2 Materials and Methods

1.2.1 Preparation of Mg microwires and design of working electrode

Commercially pure magnesium (Mg) microwires with a diameter of 127 μm (99.9% purity, Sigma Aldrich) were used as the microelectrode substrate. In this study, Mg microwires were cut into 1 cm in length and were then ultrasonically cleaned (Symphony, VWR) in acetone (Sigma Aldrich) for 15 min. Mg microwires were ground with 600, 800 and 1200 grit SiC paper

(Ted Pella) sequentially, except for the study on how polishing of Mg microwires affected PEDOT deposition. Finally, Mg microwires were ultrasonically cleaned in ethanol (200 proof; Koptec) for 15 min and dried in air for 30 min.

Figure 1-1 shows the design of working electrode for PEDOT deposition. A standard copper probe (Length: 0.212 in; Width: 0.032 in; A-M Systems) was used at the connector end of

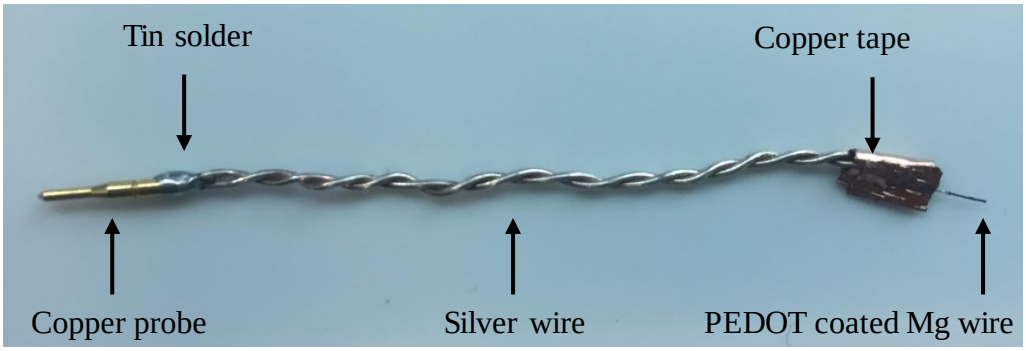

Figure 1-1. Design of working electrode for PEDOT deposition. Silver wire was attached to Mg wire by copper tape. Copper connector was welded with silver wire by tin solder and used for connecting to the potentiostat.

the electrode for easy connection with the Potentiostat (model 273A, EG&G Princeton Applied Research) for electrochemical deposition and corrosion testing, as well as for future connection with our electrical instruments for neural recording in the brains of mice or rats. Each Mg microwire was connected to each copper probe using a standard silver wire (99.99% purity; diameter: 0.025 in; A-M Systems) because of its excellent conductivity and minimal effects on electrode properties. Specifically, the silver wire was attached to Mg microwire securely using a copper tape and the copper probe was welded with silver wire using tin solder; all of these have been widely used in electrode design.

1.2.2 Electrochemical deposition of PEDOT on Mg microwires

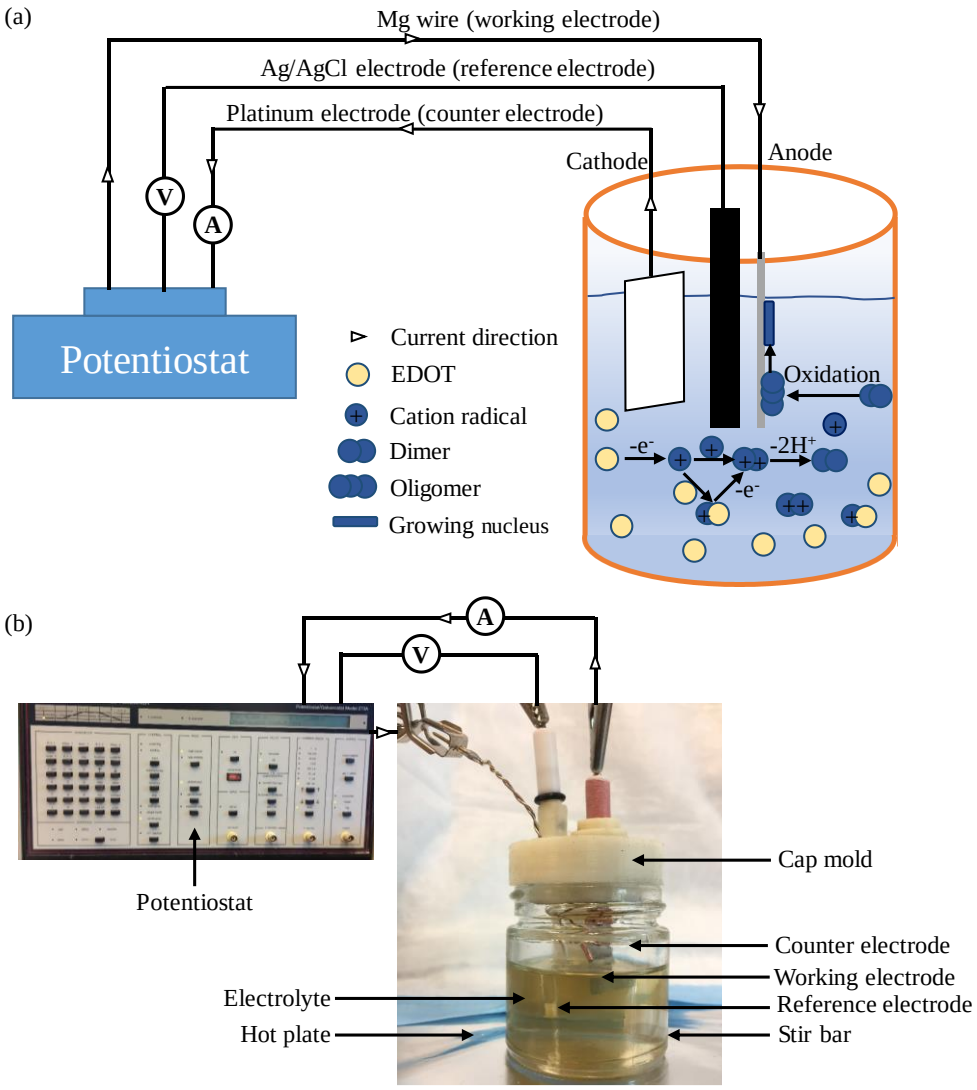

Figure 1-2. (a) Schematic illustration of experimental setup for electrochemical deposition of PEDOT on Mg wire. Reference electrode was silver/silver chloride (Ag/AgCl), counter electrode was platinum (Pt), and the working electrode was Mg wire. The optimal concentration of EDOT/1-ethyl-3-methylimidazolium bis(trifluromethylsulfonyl)imide was 1 M. (b) Photograph of electrochemical deposition setup.

Three electrodes and an electrolyte bath were included in the experimental setup for electrochemical deposition, as shown in Figure 1-2. Mg microwire prepared above was used as the working electrode, and silver/silver chloride (Ag/AgCl, CH Instruments) was used as

reference electrode. The counter electrode was a platinum plate (Pt, 25 mm×12 mm, CH Instruments). The electrolyte bath with 1 M 3,4-ethylenedioxythiophene (EDOT, Sigma-Aldrich) was prepared by adding 2.136 mL of EDOT to 17.863 mL of pristine 1-ethyl-3-methylimidazolium bis(trifluromethylsulfonyl)imide with a 99% purity (i.e. ionic liquid, Iolitec Inc.). The resulted 20 mL of electrolyte was put into a 25 mL glass vessel with a magnetic stir bar, which was placed on top of a magnetic hot plate for heating and stirring. A 3D-printed plastic cap mold was used to hold the three electrodes in place, and alligator clips were used to secure the electrodes and connect them to the Potentiostat, as shown in Figure 1-2. Mg microwire portion of the working electrode was carefully immersed in the electrolyte bath, to prevent the connecting copper tape from being exposed to the electrolyte and thus prevent copper contamination during PEDOT deposition.

The deposition current, voltage, sweep rate, and cycle parameters (number and duration) for electrochemical deposition, were controlled by the Potentiostat, and the temperature was controlled by the hot plate. When the voltage provided by Potentiostat was applied to the Mg microwire in the electrolyte bath, EDOT were first oxidized to form cation radicals [32, 43]. A dimer then formed by two coupled cation radicals or one EDOT monomer and one cation radical, with the removal of two protons [44-46]. Dimer was further oxidized, and oligomers formed and grew onto the surface of Mg microwire to form PEDOT coating [43-46]. After deposition, PEDOT-coated Mg microwires were suspended and dried horizontally in an oven at 37 °C for 48 h. Horizontal orientation is beneficial for uniform coating formation by minimizing the effect of gravity.

1.2.3 Parameters of interest for electrochemical deposition of PEDOT onto Mg microwires

The effects of key parameters on PEDOT deposition onto Mg microwires were investigated for the first time. Chronopotentiometry was performed at a constant current while

cyclic voltammetry (CV) involved a number of cycles between two different potentials. To achieve uniform PEDOT coating on Mg microwires, both chronopotentiometry and CV methods and associated key parameters were investigated. The deposition current was studied for chronopotentiometry method. The temperature of electrolyte bath, deposition voltage, sweep rate, cycle number and duration in CV method were studied to identify the optimal CV deposition parameters. The deposition parameters in both chronopotentiometry and CV methods are summarized in Table 1-1.

Table 1-1. List of deposition parameters studied in chronopotentiometry and cyclic voltammetry (CV) methods for depositing PEDOT onto Mg microwires.

Method	Chronopotentiometry	Cyclic Voltammetry (CV)			
Deposition Parameters	Deposition Current (μA)	Deposition Temperature (°C)	Deposition Voltage (Volts)	Sweep Rate (mV/s)	Cycle Number
	50	25	1.0	5	1
	100	50	1.25	50	30
	200	65	1.5	100	60

For the chronopotentiometry method, the deposition current was set to 50 μA, 100 μA, and 200 μA with a duration of 300 s; and the temperature of electrolyte was set at 25 °C. In the CV method, the deposition parameters were investigated as described below to determine their respective effects on PEDOT coating onto Mg microwires.

(1) Temperature of electrolyte: To test the effects of electrolyte temperature on PEDOT coating, the temperature was set to 25 °C, 50 °C and 65 °C, which were selected based on literature.[47] PEDOT was deposited onto Mg microwires using CV from -2.0 V to 1.5 V for 30 cycles at 20 s per cycle with a sweep rate of 100 mV/s.

(2) Deposition voltage: PEDOT was deposited onto Mg microwires using CV from -2.0 V to 1.0 V, 1.25 V and 1.5 V to determine the effects of deposition voltage on PEDOT coating.

The deposition had 30 cycles at 20 s per cycle with a sweep rate of 100 mV/s. The temperature of electrolyte was set to 25 °C constantly.

(3) Sweep rate: PEDOT was deposited onto Mg microwires using CV from -2.0 V to 1.5 V for 30 cycles at 20 s per cycle with a sweep rate of 5 mV/s, 50 mV/s and 100 mV/s to determine the effects of sweep rate. The temperature of electrolyte was set to 25 °C constantly.

(4) Cycle number and duration: PEDOT was deposited onto Mg microwires using CV from -2.0 V to 1.5 V for 1 cycle with a duration of 600 s, 30 cycles with a duration of 20 s per cycle, or 60 cycles with a duration of 10 s per cycle. The sweep rate was 100 mV/s and the temperature of electrolyte was set to 25 °C constantly.

The effects of polishing conditions of Mg microwires on the formation of PEDOT coating were also studied. Three different surface conditions of Mg microwires were investigated: (1) Non-polished Mg microwires; (2) Mg microwires that were polished with 1200 grit SiC paper; and (3) Mg microwires that were ground and polished with 600, 800 and 1200 grit SiC paper sequentially. For this purpose, PEDOT was deposited onto these Mg microwires using CV from -2.0 V to 1.25 V for 1 cycle of 600 s with a sweep rate of 5 mV/s; the temperature of electrolyte was set to 65 °C.

1.2.4 Surface characterization of PEDOT-coated and non-coated Mg microwires

PEDOT-coated Mg microwires and non-coated Mg microwires were examined and screened using optical microscopy (SE303R-P, Amscope) to identify the optimal processing parameters. ImageJ was used to calculate the diameter of samples. Each wire type was measured 5 times to get the average and standard deviation. The PEDOT coatings showed the most consistent and homogeneous morphology when they were deposited using CV from -2.0 V to 1.25 V for 1 cycle of 600 s with a sweep rate of 5 mV/s at the electrolyte temperature of 65 °C. PEDOT coatings provided consistent and complete coverage on the surface when the Mg

microwires were ground with 600, 800 and 1200 grit SiC paper sequentially. The optimal PEDOT-coated Mg microwires obtained under these processing parameters were selected for further surface characterization and electrochemical testing. Surface morphology and elemental composition of PEDOT-coated and non-coated Mg microwires were characterized using scanning electron microscopy (SEM; Nova NanoSEM 450, FEI Co.) at a 15 kV accelerating voltage under the high vacuum mode and energy dispersive X-ray spectroscopy (EDS; Aztec, Oxford instruments, Abingdon, UK), respectively.

Table 1-2. List of chemicals used for preparing artificial cerebrospinal fluid (aCSF) [49].

aCSF composition	**Concentration (mM)**
$CaCl_2$*$2H_2O$	2.5
Sucrose	138
NaCl	119
KCl	2.5
$MgSO_4$*$7H_20$	1.3
NaH_2PO_4	1
$NaHCO_3$	26.2
(D)-Glucose	11
Kynurenic acid	3

1.2.5 Electrochemical testing of PEDOT-coated and non-coated Mg microwires

The Mg microwires with the optimal PEDOT coatings and non-coated Mg microwires were tested electrochemically for their corrosion properties. A standard method for potentiodynamic polarization (PDP) testing was used, and the details have been described elsewhere [48]. Specifically, the PDP testing was performed with the potential ranged from -2.0 V to 1.0 V at the sweep rate of 5 mV/s in an artificial cerebrospinal fluid (aCSF) at 37 °C. The aCSF was used to mimic the cerebrospinal fluid (CSF) because the Mg microwire electrodes were designed and prepared for neural recording or stimulation in central nerve system *in vivo*. The chemicals and their concentrations used for aCSF preparation [49] are listed in Table 1-2; and the

pH of aCSF was adjusted to 7.4. The corrosion potential (E_{Corr}) and corrosion current density (J_{Corr}) were extrapolated from the potentiodynamic polarization (PDP) curves using the Tafel method according to ASTM standard G 102-89. The corrosion rates (CR) of PEDOT-coated microwires and non-coated Mg microwires were calculated according to the following equation:

$$CR = (J_{Corr} \times K \times W)/\rho \quad (1)$$

Where K is unit conversion constant, W is equivalent weight of Mg and ρ is density of Mg. Specifically, $K_1=3.27x10^{-3}$ (mm•g)/(μA•cm•year), EW=12.15, $\rho=1.74$ g/cm^3.

1.3 Results

1.3.1 The effects of deposition parameters on PEDOT coatings on Mg microwires

Figure 1-3 shows the optical images of PEDOT deposited on Mg microwires using chronopotentiometry or CV method with different parameters of interest. Figure 1-3a shows the optical images of PEDOT coating on Mg microwire at different deposition current using chronopotentiometry method. When the deposition current was 50 μA, there was no coating on Mg microwire surface. At the current of 100 μA, the PEDOT coating appeared smooth but thin. When the current increased to 200 μA, the PEDOT aggregated as islands on some surface regions of Mg microwires and did not fully cover the microwire surface. Figure 1-3b-e shows the optical images of PEDOT coatings deposited on Mg microwires using CV method under different deposition temperature, voltage, sweep rate, cycle number and duration. Specifically, as shown in Figure 1-3b, when the electrolyte temperature increased, the thickness of PEDOT coating increased and the coating coverage improved.

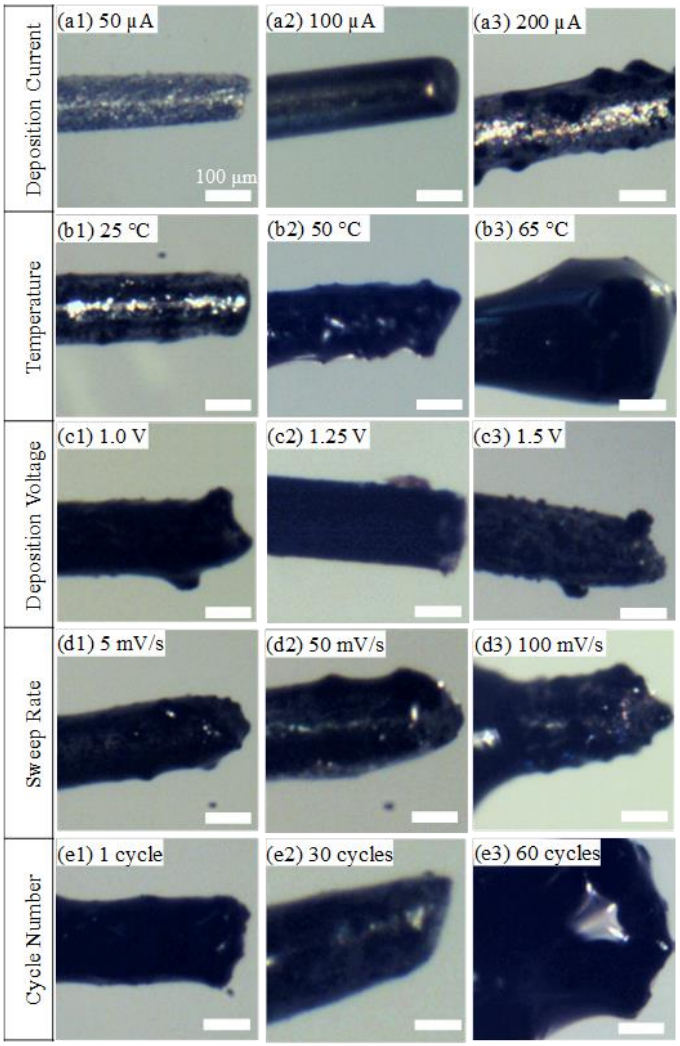

Figure 1-3. Optical images of PEDOT coating on Mg wire using chronopotentiometry or cyclic voltammetry methods with variable parameters. (a) Optical images of PEDOT coated Mg using chronopotentiometry method with different deposition current: (a1) 50 µA ; (a2) 100 µA ; (a3) 200 µA. (b) Optical images of PEDOT coated Mg using CV method under different deposition temperature: (b1) 25°C; (b2) 50°C; (b3) 65°C. (c) Optical images of PEDOT coated Mg using CV method with different deposition voltage: (c1) 1.0 V; (c2) 1.25 V; (c3) 1.5 V. (d) Optical images of PEDOT coated Mg using CV method with different sweep rate: (d1) 5 mV/s; (d2) 50 mV/s; (d3) 100 mV/s. (e) Optical images of PEDOT coated Mg using CV method under different cycles: (e1) 1 cycle for a duration of 600 seconds; (e2) 30 cycles for a duration of 20 seconds per cycle; (e3) 60 cycles for a duration of 10 seconds per cycle. All scale bars are 100µm.

At 25 °C, the PEDOT only sporadically covered some regions of surface and metallic Mg was still clearly visible. At 50 °C, the PEDOT coating completely covered Mg surface and the

coating thickness increased. When the temperature increased to 65 °C, the coating thickness continued to increase. As shown in Figure 1-3c, the deposition voltage influenced the morphologies of PEDOT coating, and PEDOT covered the microwire surface completely at all three voltages tested, i.e., 1.0 V, 1.25 V, and 1.5 V. At 1.25 V, PEDOT coatings appeared smooth and uniform with less aggregates when compared with 1.0 V and 1.5 V. As shown in Figure 1-3d, the sweep rate affected the homogeneity of PEDOT deposition. At the sweep rate of 5 mV/s, the PEDOT coatings appeared more homogenous in thickness and distribution when compared with the higher sweep rates of 50 mV/s and 100 mV/s. Figure 1-3e shows that the more the deposition cycles, the thicker the coating. The PEDOT coatings appeared homogenous and fully covered the microwire surface after in 1 cycle of deposition with a duration of 600 s. The thickness of coating increased but not uniform after 30 cycles of deposition with a duration of 200 s per cycle. After 60 cycles with a duration of 100s per cycle, the coating thickness continued to increase and the diameter of the microwire increased to 374.28 μm, which is not desirable. Collectively, CV deposition from -2.0 V to 1.25 V for 1 cycle of 600 s with a sweep rate of 5 mV/s at the electrolyte temperature of 65 °C was selected as the optimal condition for depositing PEDOT onto Mg microwires.

1.3.2 Surface polishing of Mg microwires affected PEDOT coating

Figure 1-4 shows the effects of microwire surface polishing on PEDOT deposition. The surface of non-polished Mg microwires showed inhomogeneous oxidation; and there was no visible coating on the surface after CV deposition with the optimal parameters (Figure 1-4a1, a2). Polishing with 1200 grit SiC paper improved the smoothness of microwire surface but still showed inhomogeneous distribution of oxides on the surface; and PEDOT coating was deposited on the surface but not uniform (Figure 1-4b1, b2). Grinding and polishing sequentially with 600, 800 and 1200 grit SiC paper removed surface oxides and the post-polishing Mg microwires

showed a more homogenous appearance (Figure 1-4c1). The PEDOT coating deposited on well-polished Mg microwires appeared homogenous and fully covered the entire microwire surface (Figure 1-4c2), which was selected for further characterization.

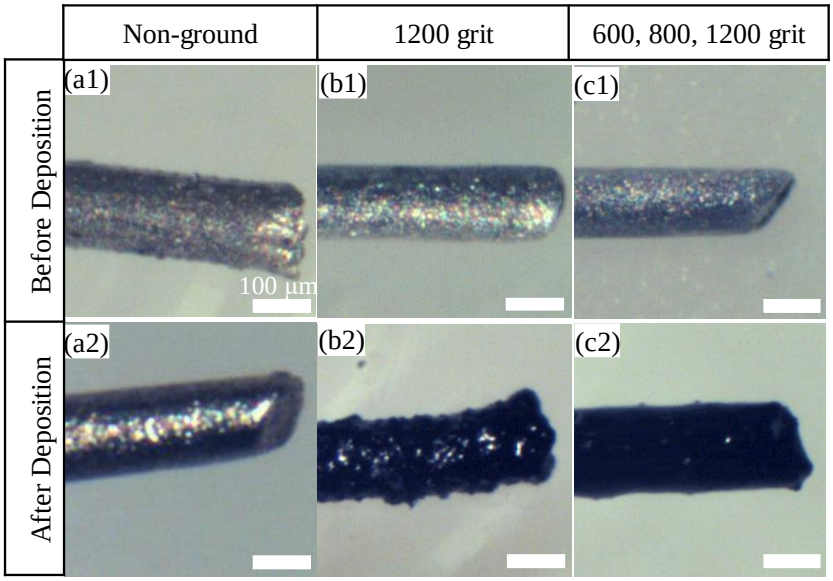

Figure 1-4. Optical images of non-polished Mg wire and polished Mg wires with different grinding conditions before and after PEDOT deposition with the optimized deposition parameters. The optimized deposition parameters were that Mg wires were coated from -2.0 V to 1.25 V for 1 cycle with a sweep rate of 5 mV/s. The duration of the cycle was 600 s and temperature of electrolyte bath was set to 65°C. (a1) Non-polished Mg wire; (a2) Mg wire in (a1) after the optimized PEDOT deposition; (b1) Mg wire ground with 1200 grit SiC paper; (b2) Mg wire in (b1) after the optimized PEDOT deposition; c) Mg wire grinded with 600, 800 and 1200 grit SiC paper sequentially; (c2) Mg wire in (c1) after the optimized PEDOT deposition. All scale bars are 100µm.

1.3.3 Surface microstructure and composition of PEDOT-coated and non-coated Mg microwires

Figure 1-5 shows SEM images and EDS analyses of PEDOT-coated and non-coated Mg microwires. As shown in Figure 1-5a, the polished Mg microwires showed a consistent and homogenous appearance. The deposited PEDOT coating was uniform and fully covered the Mg microwire surface (Figure 1-5b). Some PEDOT formed spherical aggregates on the coating surface and caused topographical roughness. Figure 1-5c shows EDS area and point analyses on

the non-coated and PEDOT-coated Mg microwires. Specifically, non-coated Mg microwire showed similar composition of Mg, carbon (C) and oxygen (O) in whole imaging area of (a3) and point 1; Mg was the main component (>88 wt%) with a small amount of C (<10 wt%) and O (<2 wt%). The presence of O indicated surface oxidation since Mg had a strong tendency to be oxidized. The EDS area and point analysis of PEDOT-coated Mg microwire all showed the presence of Mg, C, O, sulfur (S), fluorine (F) and nitrogen (N). Point 3 had less amount of Mg (1.98 wt%), F (0.77 wt%) and N (0 wt%) than point 2 (Mg 8.52 wt%, F 13.23 wt%, N 4.78 wt%) and point 4 (Mg 10.54 wt%%, F 21.22 wt%, N 9.44 wt%), while the amount of C detected in point 3 (72.88 wt%) was much higher than point 2 (40.37 wt%) and point 4 (34.67 wt%).

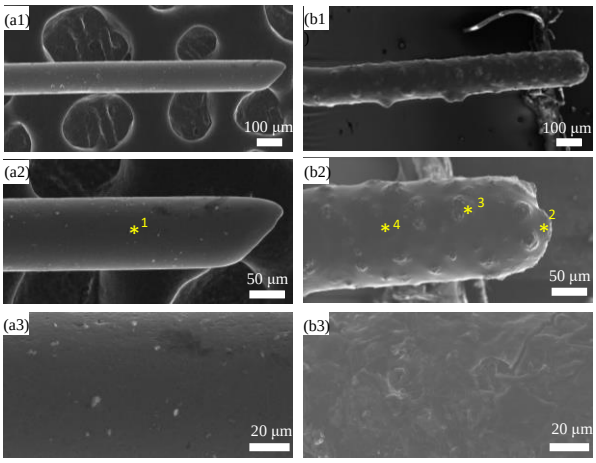

(c)

Element [wt. %]	Position 1	Non-coated Mg	Position 2	Position 3	Position 4	PEDOT coated Mg
Mg	88.7	89.3	8.52	1.98	10.54	7.9
C	9.8	9.0	40.37	72.88	34.67	38.6
O	1.5	1.7	17.78	11.50	15.90	31.9
S			15.31	12.87	8.23	7.9
F			13.23	0.77	21.22	9.6
N			4.78	0.00	9.44	4.0

Figure 1-5. Surface analysis of non-coated Mg wire and PEDOT coated Mg wire with the optimized deposition parameters. All Mg wires were ground with 600, 800 and 1200 grit SiC paper sequentially. (a1-a3) SEM image of the surface of non-coated Mg wire at an original magnification of (a1) 100x, (a2) 350x, and (a3) 1000x. (b1-b3) SEM image of the surface of PEDOT coated Mg wire at an original magnification of (b1) 100x, (b2) 350x, and (b3) 1000x. (c) EDS point analysis showing quantitative surface elemental composition (wt. %) of the highlighted points in (a2) and (b2) and EDS area analysis of (a3) and (b3) at 1000x magnification.

1.3.4 Improved corrosion behavior of PEDOT-coated Mg microwire

Figure 1-6 shows the PDP curves of PEDOT-coated and non-coated Mg microwires in aCSF; Table 1-3 shows corresponding values of corrosion current density, corrosion potential and corrosion rate after Tafel extrapolation. The results indicated that PEDOT coating decreased the corrosion rate of Mg microwires significantly. Specifically, the corrosion current density (J_{Corr}) of PEDOT coated and non-coated Mg microwires was 33.0 μA/cm^2 and 78.1 μA/cm^2, respectively; the corrosion potential (E_{Corr}) of PEDOT-coated Mg microwire (-0.40 V) was less negative than non-coated Mg microwire (-1.41 V). The corrosion rate of PEDOT coated Mg microwire was 0.75 mm/year, much slower than the non-coated Mg microwire that showed a corrosion rate of 1.78 mm/year.

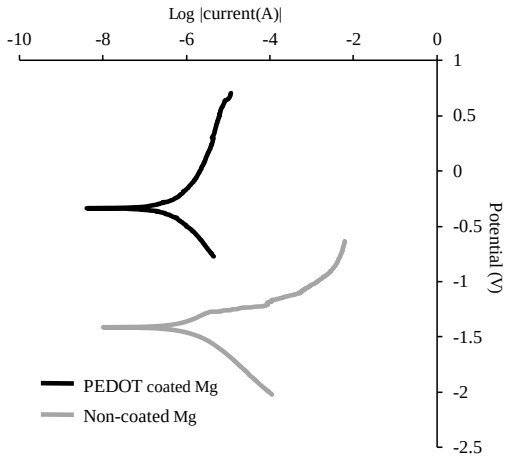

Figure 1-6. Potentiodynamic polarization curves of PEDOT coated Mg wire and non-coated Mg wire in artificial cerebrospinal fluid (aCSF) at pH 7.4 at 37 °C. The PEDOT coating was deposited using optimized parameters. Scanning parameters for the potentiodynamic polarization testing ranged from -2.0 V to +1.0 V at a sweep rate of 5 mV/s.

1.4 Discussions

1.4.1 The effects of electrochemical deposition parameters on PEDOT coatings

It has been reported that the morphology can affect the corrosion protection and performance of a conducting polymer coating [50, 51]. The CV method was reported to be superior than chronoamperometry method in terms of coating adhesion and corrosion protection [32]. In this study, we found that electrochemical deposition parameters have significant effects on the morphology and thickness of PEDOT coatings onto Mg microwires.

Table 1-3. Corrosion properties of PEDOT-coated and non-coated Mg microwires.

	Current Density ($\mu A/cm^2$)	Corrosion Potential (V)	Corrosion Rate (mm/year)
PEDOT-coated Mg	33.0	-0.40	0.75
Non-coated Mg	78.1	-1.41	1.78

Firstly, chronopotentiometry method was not optimal for depositing PEDOT coating. In chronopotentiometry method, the PEDOT coating formation was determined by the integrated charges in electrolyte bath that was controlled by the current density [43]. However, the higher current density caused PEDOT to form spherical aggregates on Mg microwire surface instead of forming uniform and consistent coating. Because deposition current was the most critical parameter in this method and we did not find an optimal current, and thus we did not study other parameters further, such as the temperature of electrolyte bath and deposition duration. The optimal deposition parameters were found using CV method. During CV deposition, the PEDOT coating thickness increased and coating coverage improved with higher electrolyte bath temperature. The increase in temperature accelerated the flow of ions in electrolyte. Therefore, more oligomers were formed and growing into PEDOT coating on Mg microwire. Deposition voltage was another key factor to determine the homogeneity of PEDOT coating. When the voltage was too low, there was no coating formed since EDOT monomers could not be

polymerized. In contrast, when the voltage was too high, too much rapid polymerization would cause non-uniform coating. Sweep rate should also be low enough (5 mV/s) to allow steady and continuous polymerization. The fast sweep rate (100 mV/s) created a more inconsistent coating thickness. In addition, 1 cycle with long duration (600 s) was enough to form homogenous PEDOT with moderate thickness. Repeated cycles would make the PEDOT coating on Mg microwire too thick. Collectively, CV deposition from -2.0 V to 1.25 V for 1 cycle of 600 s with a sweep rate of 5 mV/s at the electrolyte temperature of 65 °C was selected as the optimal condition for depositing PEDOT onto Mg microwires.

1.4.2 The effects of Mg microwire polishing condition on PEDOT coating

Surface polishing had a great influence on PEDOT deposition onto Mg microwires. The surface of non-polished Mg microwire had inhomogeneous oxide layer and contaminants that could prevent proper formation of PEDOT on Mg. The oxide layer and contaminants on Mg microwire surface cannot be fully removed if the microwire was polished with 1200 grit SiC paper only. In this case, PEDOT can grow onto the microwire surface but the coating was not uniform. The coating showed a more globular morphology and there were still some areas left non-covered. Grinding and polishing with 600, 800 and 1200 grit SiC paper sequentially, removed all contaminants, resulting in a smooth, uniform, homogenous and fully covered PEDOT coating on the microwire surface.

1.4.3 Surface morphology and element composition of PEDOT-coated Mg microwire

PEDOT-coated Mg microwire showed a uniform, packed and fully covered PEDOT coating after optimal deposition. The EDS area and point analysis both showed the presence of C, O and S, which proved the presence of PEDOT because PEDOT consists of C, O and S. The point on the small island (point 3) had less Mg than the other two points on smooth coating area

(point 2 and point 4) because the coating there was much thicker than the other regions. The presence of F indicated that F^- ions in the electrolyte was transferred onto the surface of Mg microwires during deposition.

1.4.4 PEDOT coated Mg microwire for potential neural stimulation and recording applications

This study further confirmed that the PEDOT coating could decrease the corrosion rate of Mg microwire in aCSF. Our optimal PEDOT-coated Mg microwire could potentially serve as an electrode for neural recording and stimulation applications. That is, the electrodes could provide readouts of electrical activity in central nervous system (CNS) as neural recording electrode, or could repair spinal cord injuries as a stimulating electrode. Since the Young's modulus (E) of neural tissues (E_{CNS} = 3.15−10kPa [40, 52], E_{PNS} = 400−700kPa [53, 54]) is still much lower than Mg-based electrodes, another polymer coating should be applied as an insulating layer to further reduce the mechanical mismatch between the electrodes and neural tissues. In the future *in vivo* studies, when inserting the electrodes into a brain, another layer of biodegradable polymer coating should be applied onto PEDOT-coated Mg microwires as an insulating layer, to improve the integration of electrodes and reduce trauma to surrounding neural tissues.

1.5 Conclusions

Mg microwire-based neural electrode was designed and built successfully. PEDOT coating was successfully deposited onto Mg microwires using electrochemical deposition, particularly the CV method. CV method produced more uniform coating than chronopotentiometry. Optimal deposition parameters and polished Mg microwire surface were crucial to produce homogenous and uniform PEDOT coatings. CV deposition from -2.0 V to 1.25 V for 1 cycle of 600 s with a sweep rate of 5 mV/s at the electrolyte temperature of 65 °C was identified as the optimal condition for depositing PEDOT onto Mg microwires. The optimal

PEDOT coating on Mg microwires showed uniform surface with the presence of S, C, and O. The corrosion rate of PEDOT-coated Mg microwire was 0.75 mm/year, much slower than 1.78 mm/year for the non-coated Mg microwire. Mg-based bioresorbable neural electrodes should be further studied for recording and stimulating neural activities *in vivo*.

Chapter 2 Magnesium-based Biodegradable Microelectrodes for Neural Recording

Abstract

This article reports fabrication, characterization, degradation and electrical properties of biodegradable magnesium (Mg) microwires coated with two functional polymers, and the first *in vivo* evidence on the feasibility of Mg-based biodegradable microelectrodes for neural recording. Conductive poly(3,4-ethylenedioxythiophene) (PEDOT) coating was first electrochemically deposited onto Mg microwire surface, and insulating biodegradable poly(glycerol sebacate) (PGS) was then spray-coated onto PEDOT surface to improve the overall properties of microelectrode. The assembled PGS/PEDOT-coated Mg microelectrodes showed high homogeneity in coating thickness, surface morphology and composition before and after *in vivo* recording. The charge storage capacity (CSC) of PGS/PEDOT-coated Mg microwire (1.72 mC/cm^2) was nearly 5 times higher than the standard platinum (Pt) microwire widely used in implantable electrodes. The Mg-based microelectrode demonstrated excellent neural-recording capability and stability during *in vivo* multi-unit neural recordings in the auditory cortex of a mouse. Specifically, the Mg-based electrode showed clear and stable onset response, and excellent signal-to-noise ratio during spontaneous-activity recordings and three repeats of stimulus-evoked recordings at two different anatomical locations in the auditory cortex. During 10 days of immersion in artificial cerebrospinal fluid (aCSF) *in vitro*, PGS/PEDOT-coated Mg microelectrodes showed slower degradation and less change in impedance than PEDOT-coated Mg electrodes. The biodegradable PGS coating protected the PEDOT coating from delamination, and prolonged the mechanical integrity and electrical properties of Mg-based microelectrode. Mg-based novel microelectrodes should be further studied toward clinical translation because they can potentially eliminate the risks and costs associated with secondary surgeries for removal of failed or no longer needed electrodes.

2.1 Introduction

Microelectrodes have been widely used in electrophysiology for studying the electrical properties and signaling pathways of neurons and neural networks in brain slices *in vitro* and live animals *in vivo*, enabling new discoveries on neural functions and new therapies for neural injuries and disorders [55-57]. Microelectrodes typically have compatible dimensions to neuronal structures and desirable electrical properties for neural recording and stimulation [56]. For research, glass pipettes with Ag/AgCl wire and electrolyte solution inside have been used extensively *in vitro* and *in vivo* [55]. The pipette tip is normally drawn to a submicron diameter and then inserted next to the target neuron or networks of neurons. Even though the glass pipette electrodes have stable electrode potential for reliable measurements of neural activities and are easy to make in a research laboratory, they are too fragile to serve as implantable electrodes in clinical applications for human neural recording or stimulation, or for performing high-frequency recording [58]. Therefore, the use of glass pipette electrodes is usually limited to *in vitro* and *in vivo* models for acute single-neuron recording in research, but not suitable for clinical applications on human patients.

In contrast, microelectrodes made of stiff and conductive metals such as inert platinum (Pt), stainless steel (SS), and tungsten are widely used for human clinical applications, because they are more robust than glass pipettes for implantation [21, 22, 55]. However, these metallic implantable electrodes exhibit poor stability after implantation and their performance deteriorates over the service period, mainly because of tissue damage and biofouling [58]. The mechanical mismatch between these metals and neural tissues also contributes to tissue damage and fibrosis [23]. Biofouling of the electrodes after inserted or implanted into tissue is a major problem, because it leads to the loss of electrical signals and alters the impedance and charge density of

electrodes, thus causing electrode failure *in vivo* [23-25]. Considering that these metals are inert and non-degradable in the body, in the event of electrode failure or when the electrodes are no longer needed, secondary surgeries or procedures are required for their removal, which cause clinical complications and increase healthcare costs. In recent years, some new electrode materials with unique properties have been studied but they still have drawbacks that are challenging to resolve. For example, tantalum oxide reduces electrode damage and shows high stability, but the charge storage capacity (CSC) is too low [25]. Carbon-based materials [57, 59-64] and iridium oxide [65, 66] have large CSC due to high electrochemical surface area, but their stability in biological systems and biocompatibility are questionable. Doped diamond [67] has shown good biocompatibility, large CSC, and low fouling during recording, but it is difficult to fabricate and relatively expensive. Moreover, these electrodes still require surgical removal when they fail *in vivo*.

To eliminate the necessity of surgical removal and address the complications and infections associated with current non-degradable electronics, biodegradable and biocompatible electronics have been actively pursued for medical applications in recent years [68-74]. The ultimate goal is to use naturally-originated and/or synthetic materials that are environmentally safe, biodegradable, and biocompatible for the integration of electronics with living tissues in particular. For example, silk and other biodegradable polymers, such as polyvinyl alcohol (PVA) and poly(lactic-co-glycolic acid) (PLGA), have been employed as substrates for fabricating biocompatible and biodegradable electronics [70-73]. Ideally, an implantable electrode should be biodegradable and have controllable degradation rates to eliminate the need for removal [68]. That is, the implanted electrodes should harmlessly degrade and completely disappear from the body after they have fulfilled their functions in the body. The mechanical and electrical properties of the electrodes should be retained for days to months to provide reliable recordings of neural

activities and/or neural stimulation based on specific clinical needs. Therefore, biodegradable, biocompatible, regenerative, conductive implantable microelectrodes with suitable mechanical properties are engineered in this study to meet the unmet clinical needs for neural recording, stimulation, and regeneration in clinical applications.

Magnesium (Mg) microwires were used as the substrate for the electrode design because of its attractive biodegradability, biocompatibility, conductivity, and mechanical properties [8, 15, 32, 75, 76]. Mg could degrade naturally in aqueous physiological environment, which eliminates the need for surgical removal when it is no longer needed in the body [77-82] and reduces tissue trauma and cost. Moreover, Mg^{2+} ions, which are the degradation products of Mg, could provide neuro-protective effect [30, 83]. Thus, Mg-based bioresorbable metals have great potential for implantable neural electrode applications. However, the major concern is that rapid degradation of Mg may cause local pH increase in a short time after implantation and lead to premature failure [75]. Suitable surface treatment on Mg is necessary to control the degradation rate of Mg, and further enhance the key electrical properties and stability of Mg-based electrodes for neural recording. Thus, two functional polymers, specifically, conductive poly-3,4-ethylenedioxythiophene (PEDOT) and insulating poly(glycerol sebacate) (PGS), were deposited onto Mg microwire substrates to create biodegradable, biocompatible, and implantable microelectrodes. The Mg-based novel microelectrodes captured synergistic properties of Mg microwire substrate, PEDOT coating, and PGS coating as shown in Table 2-1. The mechanical, biological and electrical properties of Mg, PEDOT and PGS in comparison with neural tissue are also summarized in Table 2-1.

Table 2-1. Illustration of the mechanical, biological, electrical properties and the complementary properties that Mg substrate, PEDOT coating, and PGS coating provide for the overall design of biodegradable microelectrodes.

Property	**Mg**	**PEDOT**	**PGS**	**Neural tissue**
Young's modulus	41-45 GPa [42]	1-5 GPa [84]	20-1200 kPa [85, 86]	3-700 kPa [40, 52-54]
Ultimate tensile strength	263 MPa [10]	30 MPa [84]	0.5-1 MPa [86]	400-800 kPa [53]
Degradation mode	Surface corrosion	Particle dispersion	Surface degradation	N/A
Degradation rate	1-3 months [87]	2-3 months [88]	1-2 months [86]	N/A
Degradation product	Mg^{2+}, OH^-, H_2 [87]	PEDOT particle [88]	Glycerol, sebacic acid [86]	N/A
Conductivity	2.3×10^7 S/m	1×10^5-8×10^5 S/m [89]	N/A	N/A
Complementary properties of Mg, PEDOT, and PGS	-Mg microwire substrate provides mechanical strength and stiffness for electrodes -PEDOT coating reduces Mg degradation and improves electrical properties of electrodes -PGS coating protects PEDOT coating from delamination, reduces mechanical mismatch between tissue and electrodes, reduces noise in recordings, provides insulation and reduces Mg degradation, and enhances biocompatibility			

The objectives of this study were to investigate the electrical properties, degradation and neural recording capability of Mg-based microelectrodes *in vitro* and *in vivo*. The optimal coating method, that is, cyclic voltammetry (CV) and its parameters for depositing uniform and dense PEDOT coatings onto Mg substrates, was reported previously [32, 90]. PEDOT-coated Mg microwires showed slower corrosion than non-coated Mg microwires during electrochemical

testing. In this study, Mg-based microwires with PEDOT and PGS coatings were designed and fabricated for the first time to study their properties in neural recording in the auditory cortex of a mouse. Pt microelectrode was included as a model control because it has been widely used in current neural electrodes and implants for human. Glass microelectrode was also included as a reference because it has been widely used in neural electrophysiology research in animals. This is the first report on the feasibility of Mg-based biodegradable implantable electrodes for neural recording inside the brain. This study first demonstrated the capability of Mg-based microelectrode in recording multi-unit stimulus-evoked activity and spontaneous activity in auditory cortex *in vivo*.

2.2 Materials and Methods

2.2.1. Preparation of Mg and Pt microwires

Pure Mg microwires with a diameter of 127 µm (99.9% purity, Sigma Aldrich) were used as the microelectrode substrate. Pt microwires (127 µm, 99.9% purity, Sigma Aldrich) were used as a control because it is the current gold standard material for implantable neural electrodes. In this study, Mg and Pt microwires were cut into 1 cm in length and were then ultrasonically cleaned (Symphony, VWR) in acetone (Sigma Aldrich) for 15 min. Mg microwires were then ground with 600, 800 and 1200 grit SiC paper (Ted Pella) sequentially to remove the oxidized layer. Finally, Mg and Pt microwires were cleaned in ethanol (200 proof; Koptec) for 15 min and dried in vacuum for 30 min.

2.2.2. Design of microelectrodes for electrochemical deposition, testing, and neural recording

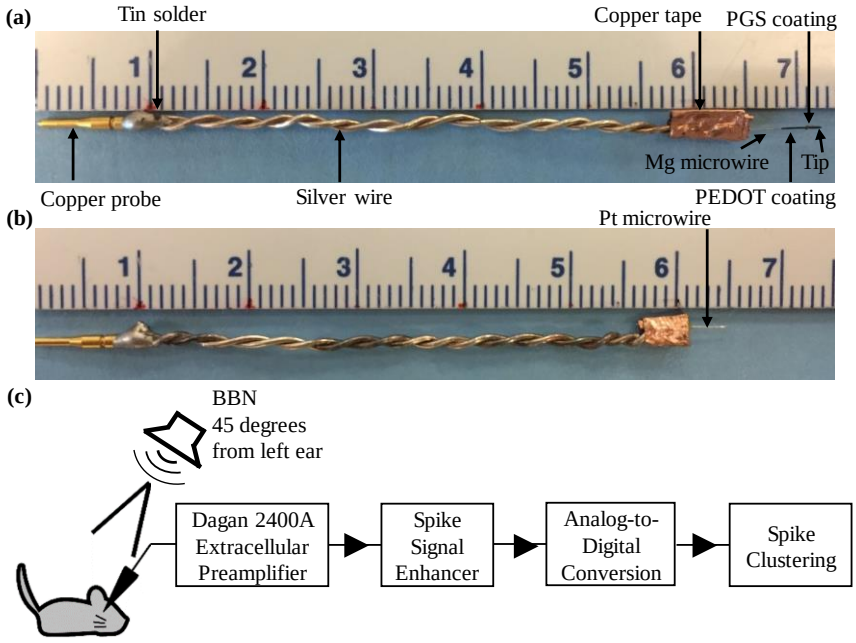

Figure 2-1. (a-b) The assembly, morphology and dimension of Mg-based microelectrode and Pt control microelectrode for neural recording. Silver wire was attached to Mg microwire using copper tape. Copper probe was welded with silver wire by tin solder and used for connecting to the neural recording setup. (a) Macroscopic image of PGS/PEDOT-coated Mg microwire electrode. Conductive poly(3,4-ethylenedioxythiophene) (PEDOT) coating was uniformly deposited onto Mg microwire by electrochemical deposition. Insulating Poly(glycerol sebacate) (PGS) was spray-coated onto the PEDOT surface except the very tip of microelectrode that was left to be conductive. (b) Macroscopic image of platinum (Pt) microwire electrode that was used as a control. (c) Schematic neural recording setup. Anesthetized mouse was placed in a stereotaxic apparatus and right auditory cortex was exposed. The electrodes were placed orthogonal to cortical surface. Neurons were stimulated by 50-ms broadband noise (BBN) played by a speaker placed at 45 degrees and 7 inches from the left ear of mouse. Neuronal activity was amplified via an extracellular preamplifier, enhanced with a signal enhancer, and then converted to digital signals.

As shown in Figure 1a-b, a standard copper probe (Length: 0.212 inch; Width: 0.032 inch; A-M Systems) was used as the connector at one end of the Mg-based or Pt-based microelectrodes for easy connection with the Potentiostat (model 273A, EG&G Princeton Applied Research) for electrochemical deposition, charge storage capacity and impedance testing, as well as for the connection with the instruments for neural recording in the mouse brain. Each Mg-based microwire was connected to each copper probe using

a standard silver wire (99.99% purity; diameter: 0.025 in; A-M Systems) because of its excellent conductivity and minimal effects on electrode properties. Specifically, the silver wire was attached to Mg-based microwire securely using a copper tape and the copper probe was welded with silver wire using tin solder; all of these have been commonly used in electrode design and fabrication. Pt microwire was connected to the standard copper probe in the same way as Mg-based microwire, and served as a control. A standard glass pipette with Ag/AgCl wire and electrolyte solution inside was used as a reference electrode for neural recording in the mouse brain.

2.2.3. Electrochemical depositions of conductive PEDOT onto Mg microwires

PEDOT($[C_2H_4O_2C_4S]_n$) coating on Mg microwires was prepared following a method optimized previously [90]. The description of methods [90] was adapted for this study with copyright permission from John Wiley and Sons. Specifically, three electrodes and an electrolyte bath were used for electrochemical deposition. Mg microwire prepared above was used as the working electrode, and silver/silver chloride (Ag/AgCl, CH Instruments) was used as the reference electrode. The counter electrode was a Pt plate (Pt, 25 mm×12 mm, CH Instruments). The electrolyte bath with 1 M 3,4-ethylenedioxythiophene (EDOT, Sigma-Aldrich) was prepared by adding 2.136 mL of EDOT to 17.863 mL of pristine 1-ethyl-3-methylimidazolium bis (trifluromethylsulfonyl) imide with a 99% purity (i.e. ionic liquid, Iolitec Inc.). The resulted 20 mL of electrolyte was put into a 25 mL glass vessel with a magnetic stir bar, which was placed on the top of a magnetic hot plate for heating and stirring. A 3D-printed plastic cap mold was used to hold the three electrodes in place, and alligator clips were used to secure the electrodes and connect them to the Potentiostat. Mg microwire portion of the working electrode was carefully

immersed in the electrolyte bath, to prevent the connecting copper tape from being exposed to the electrolyte and thus prevent copper contamination during PEDOT deposition.

The optimal condition found in our previous study, i.e., cyclic voltammetry (CV) deposition from -2.0 V to 1.25 V for 1 cycle of 600 s with a sweep rate of 5 mV/s at the electrolyte temperature of 65 °C, was used to deposit PEDOT onto Mg microwires. After deposition, PEDOT-coated Mg microwires were suspended horizontally in air and dried in an oven at 37 °C for 48 h. Horizontal orientation is beneficial for uniform coating formation by minimizing the effect of gravity.

2.2.4. Spray coating of insulating poly(glycerol sebacate) (PGS) onto microelectrodes

Spray coating method was used to deposit insulating PGS on conductive PEDOT surface and only the very tip of microwire was kept conductive without PGS coating. PGS could be synthesized by a two-step synthesis via prepolycondensation and crosslinking by glycerol ($CH_2(OH)CH(OH)CH_2OH$) and sebacic acid ($HOOC(CH_2)_8COOH$) [91]. Specifically, 0.4 g PGS precursor (Secant group) was first dissolved in 2 mL ethanol to achieve a 20% w/v concentration. The tube containing PGS precursor in ethanol was placed in an Incu-shaker (Setting: 120 RPM; Benchmark Scientific) at 50 °C for 30 min to accelerate the dissolving process and make the solution homogeneous. The solution was then transferred into the fluid cup of a spray gun (0.3 mm tip, AGPtek). The assembled microelectrode was held horizontally and the very tip was shielded from spray coating of PGS using a glass slide. The setup was examined and screened using optical microscopy (SE303R-P, Amscope) to obtain a conductive tip of 50 μm in length; that is, the conductive tip had the PEDOT coating but not the PGS coating. The distance between the tip of microelectrode and the nozzle of spay gun was set to 5 cm. Spray coating was performed for 6 seconds under the pressure of 20 psi. After that, PGS/PEDOT coated Mg

microwires were placed vertically into the oven (Thermo Scientific) to cure the PGS at 120 ℃ for 48 h in a vacuum environment. Vertical orientation took advantage of the gravity effect to control the distribution of PGS on PEDOT surface. After curing, the surface of the Mg-based microelectrode was fully covered by PGS, but the very tip of microelectrode was left as PEDOT-coated Mg to be conductive, that is, without PGS.

2.2.5. Measurement of charge storage capacity for PGS/PEDOT-coated Mg and Pt microwires

For charge storage capacity (CSC) measurements, CV was performed on the microelectrodes of interest using the Potentiostat at the sweep rate of 5 mV/s in an artificial cerebrospinal fluid (aCSF; pH 7.4, 37°C) at 37 °C. The aCSF was used to mimic the cerebrospinal fluid (CSF) because our microelectrodes were intended for neural recording in central nerve system *in vivo* [90]; the composition of aCSF is listed in the reference [90]. The CV potential ranged from -0.3 V to 0.6 V and -0.2 V to 0.8 V for PGS/PEDOT-coated Mg and Pt microwires, respectively. The CV scan range for different electrodes was different because of different electrochemical stability. CV curves were obtained from the PowerSuite 2.50.0 software (Princeton Applied Research). All potentials were measured in reference to Ag/AgCl electrode. CSC of both microelectrode types can be calculated using the following equation:

$$CSC = \frac{1}{v}\int J_a dV \quad (1)$$

Where v is the sweep rate, J_a the anodic current density and V is the scanning potential. Here, v was 5 mV/s for both microelectrodes; V was -0.3 V to 0.6 V and -0.2 V to 0.8 V for PGS/PEDOT-coated Mg and Pt microwires, respectively; J_a was the series of values on the CV curve. Even when the PGS/PEDOT-coated Mg microwires and Pt microwires were immersed in aCSF for the same length for CV scan, the conductive tip surface areas were different. Specifically, the conductive tip areas for PGS/PEDOT-coated Mg were 0.00043 cm^2, and they

were 0.02 cm^2 for Pt microwires. The current densities for each group were normalized by their respective conductive tip areas. The conductive tip areas were calculated based on the respective tip diameter and the conductive length of 50 μm and 5 mm for PGS/PEDOT-coated Mg and Pt microwires, respectively.

2.2.6. Measurement of electrochemical impedance for PGS/PEDOT-coated Mg and Pt microwires

Electrochemical impedance spectroscopy (EIS) was performed on the microelectrodes of interest in aCSF over a frequency range from 0.1 Hz to 1 MHz with logarithmic point spacing. The EIS was performed using a Potentiostat (Interface 1000, Gamry Instruments) in a three-electrode setup where the studied microelectrode was the working electrode, Ag/AgCl was the reference electrode, and a Pt plate was the counter electrode. The conductive tip that was immersed in aCSF had a length of 50 μm for both PGS/PEDOT-coated Mg microwire and Pt microwire.

2.2.7. Surface characterization of PGS/PEDOT-coated Mg and Pt microwires before and after *in vivo* neural recording

Prior to *in vivo* neural recording, PGS/PEDOT-coated Mg and Pt microwires were examined and screened using optical microscopy (SE303R-P, Amscope). The surface microstructure of PGS/PEDOT-coated Mg and Pt microwires were further characterized using scanning electron microscope (SEM; Nova NanoSEM 450, FEI Co.) under the high vacuum mode. The diameter of each sample was quantified on the respective SEM images using analysis tools in ImageJ. The diameter measurements were repeated 5 times at 5 different spots in the regions of interest to calculate the average diameter and standard deviation. Surface elemental composition and distribution were analyzed using energy dispersive X-ray spectroscopy (EDS;

Aztec, Oxford instruments, Abingdon, UK). An accelerating voltage of 15 kV was used to obtain SEM images and perform EDS analysis. PGS/PEDOT-coated Mg microwires were sputter-coated (Model 108, Cressington Scientific Instruments Ltd., Watford, UK) with Pt/Pd at 20 mA and 40 seconds of sputter time before SEM and EDS analyses.

After neural recording, the PGS/PEDOT-coated Mg and Pt microwires were examined again using optical microscopy (SE303R-P, Amscope) to identify surface change. Further, the surface microstructure and elemental composition of PGS/PEDOT-coated Mg and Pt microwires were characterized using SEM and EDS at an accelerating voltage of 15 kV under high vacuum mode. PGS/PEDOT-coated Mg microwires were sputter coated with Pt/Pd at 20 mA and 40 s sputter time before SEM and EDS analyses.

2.2.8. PGS/PEDOT-coated Mg-based microelectrodes for multi-unit neural recording *in vivo*

The procedures performed on mice were approved by the Institutional Animal Care and Use Committee (IACUC) at the University of California, Riverside. Specifically, FVB.129P2-Pde6b+Tyrc-ch/AntJ mice were obtained from Jackson laboratories and housed and bred in an accredited vivarium on a 12-hour light/dark cycle. Food and water were provided *ad libitum*. Briefly, a 2-month-old FVB WT mouse was anesthetized with isoflurane inhalation (2% in air) and secured on a bite bar and placed in a stereotaxic apparatus (model 930; Kopf, Tujunga, CA). Toe pinch reflex was monitored during the experiment and isoflurane levels were adjusted as needed. Once the mouse was sufficiently anesthetized, a midline incision was used to expose the skull and a dental drill was used to expose the auditory cortex after reflecting the temporalis muscle. Auditory cortex was identified using coordinates and vasculature [92]. At the end of the experiment, the mouse was euthanized using a lethal dose of 125 mg/kg sodium pentobarbital.

Recordings from the auditory cortex were obtained using previously published methods [92, 93]. Figure 2-1c shows the schematic setup. Electrophysiological recordings were conducted in a sound-attenuated chamber lined with anechoic foam (Gretch-Ken Industries, OR). Specifically, anesthetized mouse was placed in a stereotaxic apparatus and right auditory cortex was exposed. The electrodes were placed orthogonal to cortical surface. Neurons were stimulated by 50 millisecond (ms) of broadband noise (BBN) played by a free field speaker (Player BL Light; Avisoft, Gleinicke, Germany) placed at 45 degrees and 7 inches from the left ear of mouse. Neuronal activity was amplified via an extracellular preamplifier (Dagan 2400A), enhanced with a signal enhancer (FHC Co., USA), and then converted to digital signals. The band-pass filter on the preamplifier was set to record signals with frequencies between 300 and 3000 Hz, similar to most single/multi-unit recording experiments. The sampling rate of the acquisition set up was 32 kHz. Acoustic stimulation and data acquisition were performed using a custom-written software (Batlab, Dr. Dan Gans, Kent State University, OH) and a Microstar digital signal processing board. Sound intensity was controlled by programmable attenuators (PA5; Tucker-Davis Technologies, Gainesville, FL).

Recordings were obtained using the PGS/PEDOT-coated Mg microelectrode, Pt microelectrode, and glass reference electrode filled with 1M NaCl (impedance 2–10 MΩ). Electrodes were maintained orthogonal to the auditory cortex and driven into the cortex using a Kopf direct drive 2660 micro-positioner with 10-30 µm of insertion per move. The depth of recordings was ~500-600 µm corresponding to cortical layer IV and layer V. Glass reference electrode was first inserted into location L0 of the cortex (referred to as glass@L0) for neural recording and taken out. PGS/PEDOT-coated Mg microwire was inserted into a different location L1 (referred to as Mg@L1) and taken out after recording. Subsequently, the same PGS/PEDOT-coated Mg microwire was inserted into another location L2 (referred to as Mg@L2) to perform

recording and then taken out. Finally, Pt microwire was inserted in a different location L3 (referred to as Pt@L3) to perform recording and taken out. Neurons located in core auditory cortex were identified using short latency responses to pure tone stimuli, as well as tonotopy and vasculature landmarks. Sound level was changed with 5 dB resolution to determine the threshold of the neuron's response. Multi-unit activity was obtained for all three types of electrodes during an initial 10 minutes of silence to characterize spontaneous-activity levels. Next, stimulus-evoked activity was recorded during presentation of 50-ms BBN stimulus (600 repetitions, 1 Hz repetition rate, 300-ms recording window from stimulus onset) in three 10-minutes intervals interspersed with three 10-minutes rest periods of silence. Neural recording setup parameters for Mg@L1, Mg@L2, Pt@L3 and Glass@L0 were summarized in Table 2-2.

Example waveforms of multi-unit spikes that crossed thresholds and representative raw waveforms with each electrode during neural recording were recorded and drawn manually based on the raw data. The magnitude of responses was compared by generating a post-stimulus time histogram (PSTH) of responses to the 50-ms BBN stimulus presented at 35 dB above threshold. The average spontaneous activity was calculated by dividing the total number of spikes recorded in silent windows by the number of repetitions of the silent window. The average spikes in response to the 50-ms BBN stimulus was calculated by dividing the total number of spikes recorded in active windows by the number of repetitions of the active window. Stimulus-to-spontaneous ratio was calculated as follows, that is, dividing the average spikes in stimulus recording by the average spikes in the spontaneous-activity recording, to represent signal-to-noise ratio for quantitative analyses. Average first spike latency in response to the 50-ms BBN stimulus was found by recording the time of first spike relative to stimulus onset during each repetition of the active window.

Table 2-2. Parameters for neural recording setup for the 3 different electrodes of PGS/PEDOT-coated Mg microwire electrode, the Pt microwire electrode and the glass reference electrode at 4 different locations of L1, L2, L3 and L0 in the auditory cortex of a mouse brain.

Samples	**Mg@L1**	**Mg@L2**	**Pt@L3**	**Glass@L0**
Recording window	300 ms			
System Gain	5K	5K	5K	2K
Signal Gain	9	5	8	4
Recording Method	50-ms Broadband Noise (BBN) Bursts			
Threshold	50 dB SPL	45 dB SPL	50 dB SPL	35 dB SPL
Recording parameters	85 dB SPL 600 repetitions RR: 1 Hz	80 dB SPL 600 repetitions RR: 1 Hz	85 dB SPL 600 repetitions RR: 1 Hz	70 dB SPL 600 repetitions RR: 1 Hz
Recording sequence	• 10-min spontaneous-activity recording • 1st: 10-min stimulus recording • 10-min rest • 2nd: 10-min stimulus recording • 10-min rest • 3rd: 10-min stimulus recording			

2.2.9. *In vitro* immersion study for Mg-based microelectrodes in artificial cerebrospinal fluid (aCSF)

A 10-day immersion study was performed to investigate the degradation properties of PGS/PEDOT-coated Mg microwires (abbreviated as PP_Mg) in aCSF. PEDOT-coated Mg microwires (abbreviated as P_Mg) and pure Mg microwires (referred to as Mg) were included as controls. The immersion study was conducted in triplicate for each type of samples. Before the immersion, the samples were imaged using an optical microscope (Amscope) and then

disinfected by exposure under ultraviolet (UV) light for 2 hours. Each sample was immersed in a well of 48-well plate containing 0.9 mL of aCSF per well, under standard cell culture conditions (i.e., a sterile environment with controlled humidity and 5% CO_2/95% air at 37 °C). The microwires of PP_Mg, P_Mg, and Mg were all placed vertically in each respective well; only 3 mm of microwire from the tip was immersed in aCSF to be consistent with the length exposed for neural recording *in vivo*.

The periods of immersion were set to be 4 hours, 1 day, 3 days, 5 days, 7 days, and 10 days. Each day of immersion is considered to be 24 hours. At each time point, the immersion aCSF was collected for analyses and fresh aCSF was added into each well. At the time points of 4 hours, 5 days and 10 days, the samples were removed from the aCSF and imaged using an optical microscope (Amscope). The pH of the aCSF was measured immediately after collecting at each time point. The aCSF collected at each time point was also diluted by 1:100 in DI water to measure the ionic concentrations of [Mg^{2+}] and [Ca^{2+}] using inductively coupled plasma optical emission spectrometry (ICP-OES; Optima 8000, Perkin-Elmer). The ICP-OES system was calibrated using 0.5-5.0 mg/L Mg^{2+} standards and 0.1-1.0 mg/L Ca^{2+} standards.

After 10 days of immersion, the samples were characterized using scanning electron microscopy (SEM; Nova NanoSEM 450, FEI Co.) and energy dispersive x-ray spectroscopy (EDS) attached to SEM, both at a 10kV accelerating voltage. All samples were sputter-coated with Pt/Pd at 20 mA for 60 seconds (Cressington; Sputter Coater 108 Auto) before SEM and EDS analyses. Electrochemical impedance spectroscopy (EIS) was performed on PP_Mg, P_Mg and Mg in aCSF over a frequency range of 0.1 Hz to 1 MHz before immersion, after 4 hours of immersion, and after 10 days of immersion. The conductive tip that was immersed in aCSF had a length of 50 μm for all the samples tested using EIS.

2.2.10. Statistical analyses

The neural recording data were examined using one-way analysis of variance (ANOVA) followed by a post-hoc test. The numerical data of the pH, and the concentrations of Mg^{2+} ions and Ca^{2+} ions in aCSF at different immersion time points were examined using two-way analysis of variance (2-way ANOVA) considering group and immersion time points as two factors, followed by post-hoc tests of different groups at the same time points. The statistical analysis was performed using GraphPad Prism 7 software. Statistical significance was considered at $*p < 0.05$, $**p < 0.01$, and $***p < 0.001$. Stimulus-evoked activity was recorded 3 times during presentation of 50-ms BBN stimulus in the experiments for neural recording. All immersion data were obtained from the sample groups that were run in triplicates.

2.3 Results and Discussions

2.3.1. Characterization of PGS/PEDOT-coated Mg microelectrode and Pt control microelectrode

Figure 2-1a-b shows the assemblies, morphologies, and dimensions of Mg-based microelectrode and Pt control microelectrode for the *in vivo* neural recording in the mouse brain. In Figure 2-1a, macroscopically, the total length of Mg-based electrode assembly was 72 mm. The length of Mg microwire was 7 mm; PEDOT coating on Mg microwire appeared in black color and covered the 4 mm end of Mg microwire; PGS coating was sprayed onto the PEDOT coating and appeared transparent. As shown in Figure 2-1b, the total length of Pt microwire electrode was 65 mm and the length of Pt microwire was 4 mm, serving as a control for PGS/PEDOT-coated Mg microwire.

PGS/PEDOT-coated Mg microwire showed desirable homogeneity in coating coverage and thickness before neural recording. As shown in Figure 2-2a, PEDOT coating had an average diameter of 153.7 μm with a small standard deviation of 4.1 μm, which indicated that PEDOT

coating was uniform generally. The thickness of PGS coating increased slowly and smoothly from the tip to the center to provide a desirable cone shape for the tip of microelectrode, which is beneficial for reducing neural trauma during insertion. The average length of PGS coating was 1473.1 μm, which was longer than the depth of implantation into auditory cortex in the brain of a mouse. The diameter of the thickest part of PGS/PEDOT-coated Mg microwire was 389.6 ± 6.2 μm and the diameter of the tip of PGS/PEDOT-coated Mg microwire was 155.2 ± 6.2 μm. The very tip of the microelectrode in a length of 50 μm was left as PEDOT-coated Mg without PGS to be conductive. Based on the length and diameter of the conductive tip, the surface area of conductive tip was calculated to be 43265 μm^2 for both EIS testing *in vitro* and neural recording *in vivo*. Essentially, only the PGS coated region and PEDOT coated tip was exposed to the brain tissue during neural recording, which reduced tissue trauma and protected the microelectrode. The Pt control microwire had an average diameter of 128.4 ± 3.3 μm and appeared smooth; its conductive tip of 50 μm in length was immersed in aCSF for EIS testing, as calculated to have a surface area of 33117 μm^2 (Figure 2-2b).

2.3.2. Electrical properties of PGS/PEDOT-coated Mg microelectrode and Pt control microelectrode

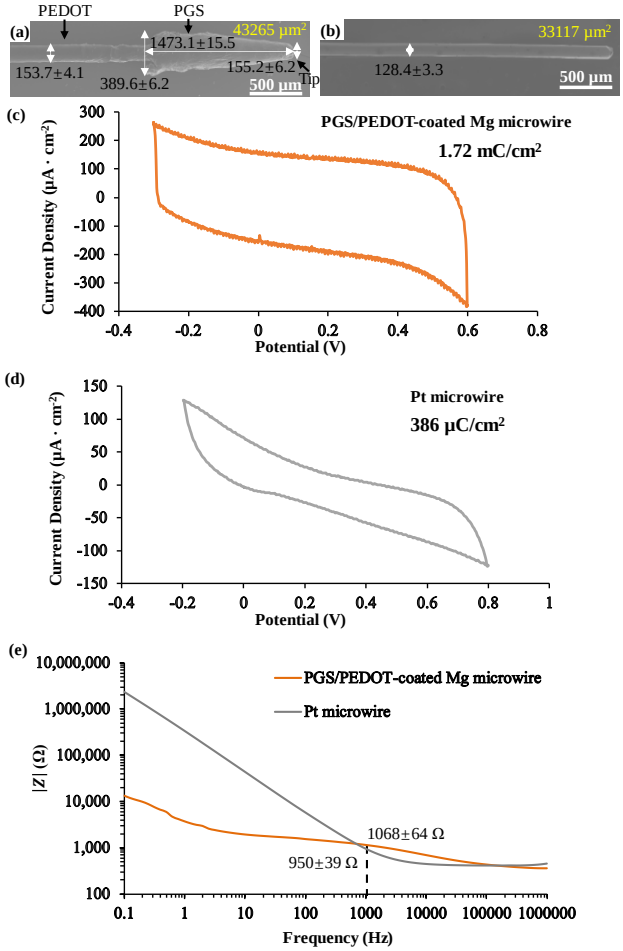

Figure 2-2. The morphology, dimension and electrical properties of Mg-based microelectrode and Pt control microelectrode for neural recording. (a) SEM image of PGS/PEDOT-coated Mg microwire at an original magnification of 50x. The diameters (µm) of PGS/PEDOT-coated Mg microwire at different regions and the length (µm) of PGS/PEDOT-coated region are labeled. The conductive tip area of PGS/PEDOT-coated Mg microwire for EIS testing was 43265 µm2. (b) SEM image of Pt microwire at an original magnification of 50x. The diameter (µm) of Pt microwire is labeled. The conductive tip area of Pt microwire for EIS testing was 33117 µm2. Scale bars in (a,b) are 500µm. (c-d) The charge storage capacity (CSC) for PGS/PEDOT-coated Mg and Pt microwires as measured by cyclic voltammetry (CV) in the artificial cerebrospinal fluid (aCSF). (c) The CSC of PGS/PEDOT-coated Mg microwire was 1.72 mC/cm2 for CV scanning from -0.3 V to 0.6 V at 100 mV/s. (d) The CSC of Pt microwire was 386 µC/cm2 for CV scanning from -0.2 V to 0.8 V at 100 mV/s. (e) Bode representation of the typical impedance spectra for PGS/PEDOT-coated Mg and Pt microwires in aCSF. The dot line indicated that the median impedance at 1000 Hz was found to be 1068±64 Ω for PGS/PEDOT-coated Mg microwire and 950±39 Ω for Pt microwire.

For a potential window of 1.0 V in the CV measurement, our results showed a CSC of 1.72 mC/cm^2 for PGS/PEDOT-coated Mg microwire in Figure 2-2c. Non-coated Mg microwire was not tested using CV because of its rapid oxidation and irreversible reactions in aqueous aCSF. Pt microwire showed a CSC of 386 μC/cm^2 for a potential window of 1.1 V in Figure 2-2d, which is close to the previously reported CSC of Pt (50-300 μC/cm^2) [39, 94]. PEDOT was reported to have a charge storage capacity (CSC) of 10-100 mC/cm^2 [39, 95]; and, PEDOT coating could significantly improve the CSC of microelectrode when compared with non-coated microwire. The CSC of PGS/PEDOT-coated Mg microwire was nearly 5 times higher than the Pt microwire. High conductivity of PEDOT coating and increased surface area contributed to the high CSC of PGS/PEDOT-coated Mg microwire, which is beneficial for neural stimulation. Moreover, excellent conductivity of PGS/PEDOT-coated Mg and Pt microwire corresponded well with their low impedance in Figure 2-2e. The impedance of PGS/PEDOT-coated Mg microwire ranged from 355 Ω to 13.4 kΩ at 1 MHz to 0.1 Hz, while the impedance of Pt microwire ranged from 454 Ω to 2336 kΩ at 1 MHz to 0.1 Hz. The impedance of PGS/PEDOT-coated Mg microwire at 1 kHz was 1068±64 Ω, similar to that of Pt microwire (950±39 Ω). It has been shown that the impedance measured in EIS had an inverse relationship with the conductive tip area of electrode [96]; and, thus, it is crucial to keep the conductive tip area immersed in aCSF for EIS to be similar for both PGS/PEDOT-coated Mg microwire and Pt microwire in order to compare them. The conductive tip that was immersed in aCSF for EIS had the same length of 50 μm for both PGS/PEDOT-coated Mg and Pt microwires; the difference in tip area is mainly caused by the difference in the tip diameter of microwires.

Importantly, considering the impedance has an inverse relationship with conductive surface area, the impedance of PGS/PEDOT-coated Mg microwire at 1 kHz (1068±64 Ω) was consistent with its conductive tip area of 43265 μm^2. In literature, the impedance of PEDOT-

coated electrodes varied from 2 kΩ to 130 kΩ at 1kHz, depending on their dimension, shape, and substrate materials. Sessolo et al. [97] prepared the PEDOT:poly(styrenesulfonate) (PEDOT:PSS) microelectrode arrays with 16 square-shaped electrodes; and each electrode had a cross-section of 20x20 μm (i.e., surface area of 400 μm^2) and showed the impedance of 23 kΩ at 1 kHz. Ludwig et al. [98] deposited PEDOT coating onto silicon (Si) microelectrodes that had sixteen-channel chronic probes; and, each probe had an area of 703 μm^2 as recording sites. The mean impedance at 1 kHz for the non-coated Si sites was 0.98 MΩ ± 0.08 MΩ, while the mean impedance at 1 kHz for the PEDOT-coated Si recording sites was 0.13 MΩ ± 0.06 MΩ. In another study, the impedance of PEDOT-coated gold electrodes at 1 kHz dropped two orders of magnitude to 10 kΩ when compared with non-coated gold electrodes; both coated and non-coated electrodes had a surface area of 1200 μm^2 [37]. Cui et al. electrochemically deposited PEDOT on Pt microwire arrays on a thin film, and each electrode had a circular shape with a diameter of 100 μm (i.e., surface area of 7854 μm^2) [99]. The PEDOT-coated Pt electrodes showed the mean impedance of 2 kΩ at 1 kHz, while the mean impedance at 1 kHz for the non-coated Pt electrodes was 100 kΩ. Therefore, PEDOT coating is expected to decrease the impedance of Mg-based microelectrodes; moreover, the impedance of PEDOT-coated electrodes would increase when the conductive surface area of electrodes decreases, which could be used to improve the performance of microelectrodes for neural recording.

2.3.3. Surface characterization of PGS/PEDOT-coated Mg microwires before and after *in vivo* neural recording in the mouse brain

Figure 2-3 shows the optical micrographs and surface characterization of the PGS/PEDOT-coated Mg and Pt microwires before and after *in vivo* neural recordings. PGS/PEDOT-coated Mg microwire showed desirable homogeneity in morphology and composition before neural recording. Specifically, the optical image of PGS/PEDOT-coated Mg

microwire in Figure 2-3a1 confirmed the cone-shaped transparent PGS coating on black-colored PEDOT coating before recording. The diameter of PGS coating increased from the tip of microwire toward the center to form the cone shape, in agreement with the SEM image in Figure 2-2a. As expected, Pt microwire showed a shiny metallic surface before recording in Figure 2-3a3. In SEM images, the PEDOT coating on Mg microwire showed a homogenous and uniform appearance in Figure 2-3b1. The PEDOT coating on the tip of Mg microwire in Figure 2-3b2 showed similar morphology as the other region of PEDOT coating on Mg microwire. PGS coating in Figure 2-3b3 showed a homogenous and fairly smooth surface. Pt microwire showed a smooth metallic surface as expected, in Figure 2-3b4.

The optical (Figure 2-3a1) and SEM images (Figure 2-3b1-b2) confirmed that PEDOT coating fully covered Mg surface, which is important for the stability of microelectrode during neural recording. The surface of PGS coating appeared smooth in Figure 2-3b3, which could reduce friction between tissue and microelectrode during insertion and neural recording and thus further ensure the stability and conductivity of microelectrodes. Both the region of PEDOT coating and the very tip of microwire showed C, O, N, F and S in their EDS area analyses in Figure 2-3c, which confirmed the presence of PEDOT, because PEDOT consists of C, O and S (Figure 2-3e). The presence of N and F could come from ionic liquid which contains N and F, because they could be transferred as dopants into the PEDOT coating. There was no Mg content detected on microwire surface, confirming that PEDOT coating was dense and packed, and fully covered Mg surface. The tip of Mg-based microelectrode showed less S and more C than the other region of PEDOT coating, confirming the presence of PEDOT, because PEDOT contains S and C but PGS contains only C without S (Figure 2-3f). The EDS results for PGS coating on Mg microwire showed C, O and N. There was no S and F detected on PGS coating, which indicated that PGS coating was dense and fully covered the surface of PEDOT coating.

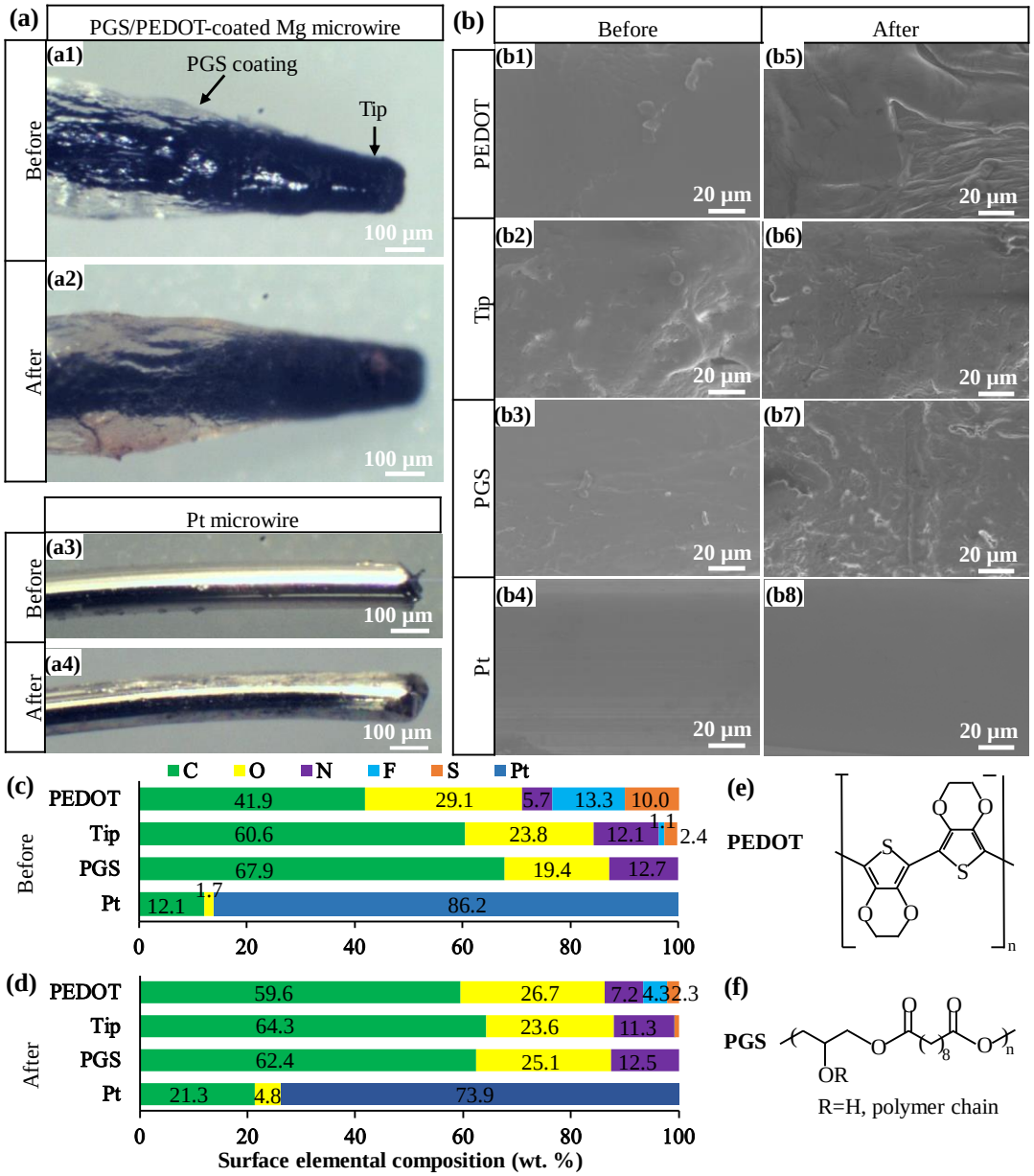

Figure 2-3. Surface characterization of PGS/PEDOT-coated Mg and Pt microwires before and after in vivo neural recording. (a) Optical images of (a1-a2) PGS/PEDOT-coated Mg and (a3-a4) Pt microwires before and after neural recording in the mouse brain. (b) SEM images of PGS/PEDOT-coated Mg microwire and Pt microwire. (b1-b4) before neural recording and (b5-b8) after neural recording. All SEM images were taken at an original magnification of 1000x. (c) Surface elemental compositions (wt.%) analyzed on the SEM images of b1-b4, respectively, using EDS. (d) Surface elemental composition (wt.%) analyzed on the SEM images of b5-b8, respectively, using EDS. (e) Chemical structure of PEDOT. (f) Chemical structure of PGS.

After two hours of repeated neural recordings at two different locations of brain, the PGS/PEDOT-coated Mg microwire was still robust without significant changes in coating morphology, microstructure, and composition as before, as shown in Figures 2-3. Specifically, the PEDOT and PGS coatings on Mg microwire retained the shape and surface morphology as compared to the same microwire before recording (Figure 2-3a2); and, the color of PGS/PEDOT-coated Mg microwire surface appeared brownish with some blood residue. The surface of Pt microwire (Figure 2-3a4) still appeared mostly metallic shiny, but the color of some regions became dull, likely because of protein deposition during *in vivo* neural recording. After *in vivo* neural recording, the surfaces of PEDOT coating on Mg microwire (Figure 2-3b5), PEDOT coating on the tip of Mg microwire (Figure 2-3b6), PGS coating (Figure 2-3b7), and Pt microwire (Figure 2-3b8) all appeared similar to the respective microwire before recording.

Figure 2-3d shows the elemental compositions quantified on the surfaces of PGS/PEDOT-coated Mg microwire and Pt microwire at the low magnification of 1000x after neural recording. The PEDOT coating on Mg microwire showed the same elements as before recording, including C (59.6wt.%), O (26.7 wt.%), N (7.2 wt.%), F (4.3 wt.%) and S (2.3 wt.%); however, the C and N content increased while the O, F, and S content decreased after recording, indicating adsorption of proteins. The EDS area analyses on the tip of Mg microwire showed the same elements as those before recording, including C (64.3 wt.%), O (23.6 wt.%), N (11.3 wt.%), F (0.1 wt.%) and S (0.7 wt.%); however, the C content increased slightly while N, F, and S content decreased after recording. The EDS results for PGS coating on Mg microwire still showed C (62.4 wt.%), O (25.1 wt.%) and N (12.5 wt.%); the C and N content increased slightly while O content decreased after recording when compared with those before recording. Generally, the PGS-coated region appeared to have less compositional change after recording, indicating less deposition of proteins on its surface in the brain. The EDS analyses on Pt microwire surface

showed Pt (73.9 wt.%) and a small amount of C (21.3 wt.%) and O (4.8 wt.%); the C and O content increased after recording when compared with those before recording, indicating deposition of proteins.

The PGS-coated region and the tip of microwire showed little change in elemental compositions after recording when compared to its counterpart before recording, which confirmed the chemical stability of PGS/PEDOT-coated Mg microwire (Figure 2-3d). The PGS coating protected the PEDOT coating and Mg microwire underneath during recording, in addition to serving as an insulating layer. Both PGS and PEDOT coatings showed excellent adhesion without detectable damages after neural recording *in vivo*. Collectively, the PGS/PEDOT-coated Mg microwire electrode was not only consistent and stable in microstructure and composition, but also able to retain its electrical properties and functionalities in repeated recordings at different anatomical locations of auditory cortex in the mouse brain. Thus, the Mg-based microelectrodes are suitable for repeated recordings in brain.

2.3.4. Performance of the Mg-based biodegradable microelectrode for *in vivo* neural recording

2.3.4.1. Capabilities of the Mg-based biodegradable microelectrode for neural recording

For our multi-unit neural recording, the band-pass filter on the Dagan amplifier was set to record signals with frequencies between 300 and 3,000 Hz and remove high-frequency noise, local field potential and other low-frequency signals. The signal was first amplified by a Dagan preamplifier, and then by a FHC spike enhancer, which further enhanced the spike amplitude over the noise baseline. Example waveforms of stimulus-evoked spikes that crossed thresholds for PGS/PEDOT-coated Mg microwire electrode and glass reference electrode are shown in Figure 2-4a-b. PGS/PEDOT-coated Mg microelectrode (Figure 4a) showed stable and consistent spike interval that was auto-correlative like glass reference electrode (Figure 2-4b). Representative raw

waveforms with each electrode during stimulus-evoked neural recording are shown in Figure 2-4c-e. The red line sets the threshold for acquiring spike timing data; the red spikes indicate those

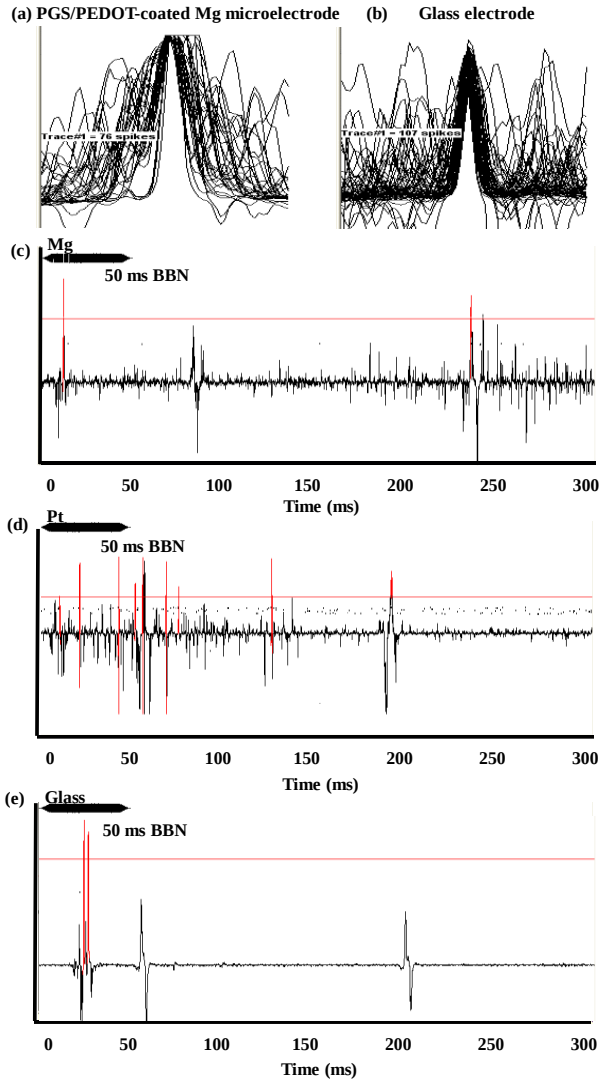

Figure 2-4. Example waveforms of multi-unit spikes that crossed thresholds for (a) PGS/PEDOT-coated Mg microelectrode and (b) glass reference electrode. (c-e) Representative raw waveforms for respective electrodes of (c) PGS/PEDOT-coated Mg, (d) Pt, and (e) glass during neural recording. The red line sets the threshold for acquiring spike timing data; red spikes indicate those counted and black spikes indicate those not counted. Some black spikes that crossed threshold were not counted because they were within the window discriminator settings. The stimulus onset was at 0 ms. The time axis in (c-e) was drawn manually over the raw traces for illustrations.

counted and black spikes indicate those not counted. Some black spikes that crossed threshold were not counted because they were within the window discriminator settings. For PGS/PEDOT-coated Mg microelectrode (Figure 2-4c), the signals were successfully recorded and not affected by the black line noise. For Pt microelectrode (Figure 2-4d), there were more black line noise than PGS/PEDOT-coated Mg microelectrode. Glass reference electrode (Figure 2-4e) exhibited minimal black line noise. Quality of multi-unit neural recording was confirmed by the raw waveforms. Collectively, the PGS/PEDOT-coated Mg microelectrode showed lower line noise level and higher signal-to-noise ratio than Pt microelectrode.

The PGS/PEDOT-coated Mg microelectrode showed excellent neural recording capability at different locations during repeated recordings of both spontaneous activity and stimulus-evoked responses, as shown in Figure 2-5. Figure 2-5a shows the spontaneous-activity recording histogram (SARH) for Mg@L1, Mg@L2, Pt@L3 and glass@L0 at 4 different locations (i.e., L0, L1, L2, and L3) in the 300-ms recording windows. Glass@L0 recorded low levels of spontaneous activity. Spontaneous activity was the largest for the Pt@L3. The PGS/PEDOT-coated Mg microwire was tested in two different locations and recorded varying levels of spontaneous activity. Mg@L1 recorded high levels of spontaneous activity and was comparable to the activity recorded using Pt@L3. However, Mg@L2 showed similar capability for recording the spontaneous activity as compared to glass@L0. Overall, during spontaneous-activity recordings, the levels of spontaneous activity recorded from high to low were (Pt@L3 > Mg@L1) >> (Mg@L2 > glass@L0), where ">" indicates slightly higher and ">>" indicates significantly higher. Not surprisingly, the glass reference electrode showed the lowest level of spontaneous activity, because the small diameter (5-10 μm) of its pipette tip resulted in less trauma and the lowest noise acquisition. Considering that the tip diameter of microelectrode strongly affects recording results [100], the PGS/PEDOT-coated Mg microelectrode was more

comparable with Pt microelectrode because of similar diameters. Obviously, the recording results would not be identical at different recording locations, even when the same electrode was used, mainly because the neural populations tested were different at different anatomical locations. This explained why Mg@L1 and Mg@L2 showed significant differences during spontaneous-activity recordings. However, both of them recorded lower noise than Pt@L3. More interestingly, the level of spontaneous activity for Mg@L2 was low and similar to glass@L0, even though the PGS/PEDOT-coated Mg microelectrode had a larger diameter than the glass reference electrode. In general, the PGS/PEDOT-coated Mg microelectrode acquired relatively low level of noise at two different locations during spontaneous-activity recording.

Figure 2-5b shows the post-stimulus time histogram (PSTH) using the 3 different electrodes at the respective 4 locations of L0, L1, L2, and L3 in response to a 50-ms duration of BBN tone. The glass@L0 exhibited the largest onset response within 50 ms of stimulus onset and the lowest spontaneous-activity recording, which indicated the highest signal-to-noise ratio. The top of the PSTH peak for glass@L0 almost reached 600 spikes. Pt@L3 also exhibited relatively high signal-to-noise ratio, demonstrating clear stimulus-evoked responses. The PSTH peak for Pt@L3 was ~340 spikes; and high level of spontaneous activity was still recorded by Pt@L3. Mg@L1 showed a relatively strong stimulus-evoked response with a PSTH peak of ~200 spikes. Mg@L2 exhibited stronger onset response and reduced spontaneous activity. The PSTH peak for Mg@L2 was ~220 spikes. Overall, during stimulus-evoked recordings, the stimulus-evoked responses recorded for all electrodes were glass@L0 >> (Pt@L3 > Mg@L2 > Mg@L1), while the levels of spontaneous activity were (Pt@L3 ≈ Mg@L1) >> (Mg@L2 ≈ glass@L0), where "≈" means similar and ">>" indicates significantly higher. During stimulus-evoked recording in Figure 2-5b, the PGS/PEDOT-coated Mg microelectrode showed clear onset response and low noise acquisition. Even though the PSTH peak for Mg@L1 and Mg@L2 was lower than that of

Pt@L3 (200-220 spikes versus 340 spikes), stimulus-evoked responses for Mg@L1 and Mg@L2 were still distinct and clear. Moreover, the levels of spontaneous activity for Mg@L1 and Mg@L2 were lower than Pt@L3. Collectively, Mg@L1 and Mg@L2 demonstrated successful recordings of both spontaneous and stimulus-evoked neural activities using the Mg-based biodegradable microelectrode for the first time (Figure 2-5c), which was confirmed by the quantitative analyses of stimulus-to-spontaneous ratio (Figure 2-5d). Specifically, average spike counts in spontaneous-activity recording were 9.40, 3.49, 11.71 and 1.87 for Mg@L1, Mg@L2, Pt@L3 and glass@L0, respectively. Average spikes for each electrode showed significant differences when compared with all the other electrodes, which confirmed that the levels of spontaneous activity during spontaneous-activity recordings were (Pt@L3 > Mg@L1) >> (Mg@L2 > glass@L0). Average spike counts in stimulus-evoked recording were 14.09, 4.44, 11.05 and 8.36 for Mg@L1, Mg@L2, Pt@L3 and glass@L0, respectively; the average spikes for each electrode showed significant differences when compared with all the other electrodes. When comparing the average spikes between spontaneous-activity recordings and stimulus-evoked recordings, the average spikes in the stimulus-evoked recordings for Mg@L1, Mg@L2 and glass@L0 were all significantly higher than the average spikes in spontaneous-activity recording, indicating a large signal-to-noise ratio. For Pt@L3, stimulus-evoked response was not significantly different from average spontaneous activity. As summarized in Figure 2-5d, Mg@L1, Mg@L2, Pt@L3 and glass@L0 showed a stimulus-to-spontaneous ratio of 1.50, 1.27, 0.94 and 4.48, respectively. Obviously, it is desirable if the stimulus-to-spontaneous ratio is larger than 1. As shown in Figure 5d, the ratio for glass@L0 (4.48) was the largest, indicating that glass reference electrode was the most sensitive in picking up neural responses to stimulus. The ratio for Mg@L1 (1.50) and Mg@L2 (1.27) were both larger than 1, indicating clear signal-to-noise ratio during stimulus-evoked recordings. However, the ratio for Pt@L3 (0.94) was smaller than 1,

which was caused by the big shift and change in the spontaneous activity level during spontaneous-activity recordings and subsequent stimulus-evoked recordings. This is related to the recording stability and biological stability of electrodes.

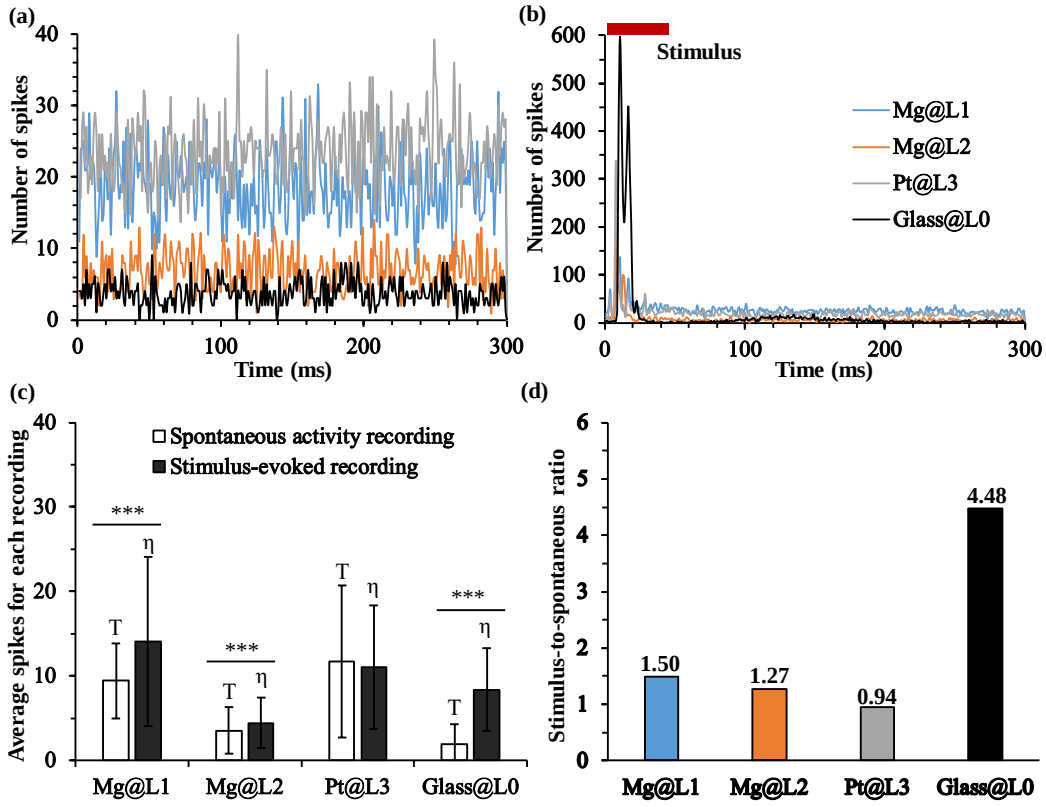

Figure 2-5. Comparison and analysis of spontaneous-activity recording and stimulus-evoked recording of Mg@L1, Mg@L2, Pt@L3 and glass@L0 in 300-ms recording window. Recording took 10 mins (600 times) and the repetition rate (RR) was 1 Hz. (a) Spontaneous-activity recording histogram (SARH). (b) Post-stimulus time histogram (PSTH) in response to a 50-ms BBN tone. (c) Average spikes in spontaneous-activity recording and average spikes in stimulus recording in response to a burst of 50-ms broadband noise (BBN) in mouse neurons in a 300-ms recording window. (d) Stimulus-to-spontaneous ratio. Values are mean ± standard deviation, n = 600; *** $p < 0.001$ when comparing the spikes of spontaneous-activity recording versus stimulus recording using the respective electrode at the respective location. T ($p < 0.001$) when comparing Mg@L1, Mg@L2, Pt@L3, and glass@L0 with each other in spontaneous-activity recording; η ($p < 0.001$) when comparing Mg@L1, Mg@L2, Pt@L3 and glass@L0 with each other in stimulus-evoked recording.

2.3.4.2. Stability of the Mg-based biodegradable microelectrode for neural recording

It is crucial for implantable microelectrodes to perform stable neural recordings in a specific period required for different clinical applications. When compared with the first 10 minutes of spontaneous-activity recording after insertion, the level of spontaneous activity for Pt@L3 significantly decreased during stimulus-evoked recording, which was probably caused by the mechanical mismatch between Pt and neural tissues and subsequent biofouling after insertion. In comparison, the PGS/PEDOT-coated Mg microelectrode exhibited consistent noise acquisition at different locations during both spontaneous activity and stimulus-evoked recordings. For both recordings with or without stimulus, Mg@L1 showed consistently higher levels of spontaneous activity, and Mg@L2 showed consistently lower levels of spontaneous activity, most likely because the neuronal groups at two different anatomical locations are different.

The stimulus-evoked recordings were repeated for three times (10 mins per recording) at each anatomical location using the respective electrodes of interest, to further evaluate their neural recording stability, as shown in Figure 2-6a-d. Stimulus-evoked responses and levels of spontaneous activity in all three recordings were consistently similar for Mg@L1 (Figure 2-6a) and Mg@L2 (Figure 2-6b), respectively, indicating excellent recording stability of the PGS/PEDOT-coated Mg microelectrode for repeated neural recordings at different locations in brain. However, for Pt@L3, during the third recording, spontaneous activity levels increased significantly (Figure 2-6c), which was possibly caused by the biofouling of Pt microelectrode, fluctuation of the anesthesia level, and the insertion-induced trauma. Moreover, considering that the repeated insertion of microelectrodes into the brain and withdrawal might affect the recording results, the order for each electrode being tested might also be a contributing factor.

The conductive tip surface area of microelectrodes that were inserted in the mouse brain is another critical factor to consider, because it can play an important role in neural recording

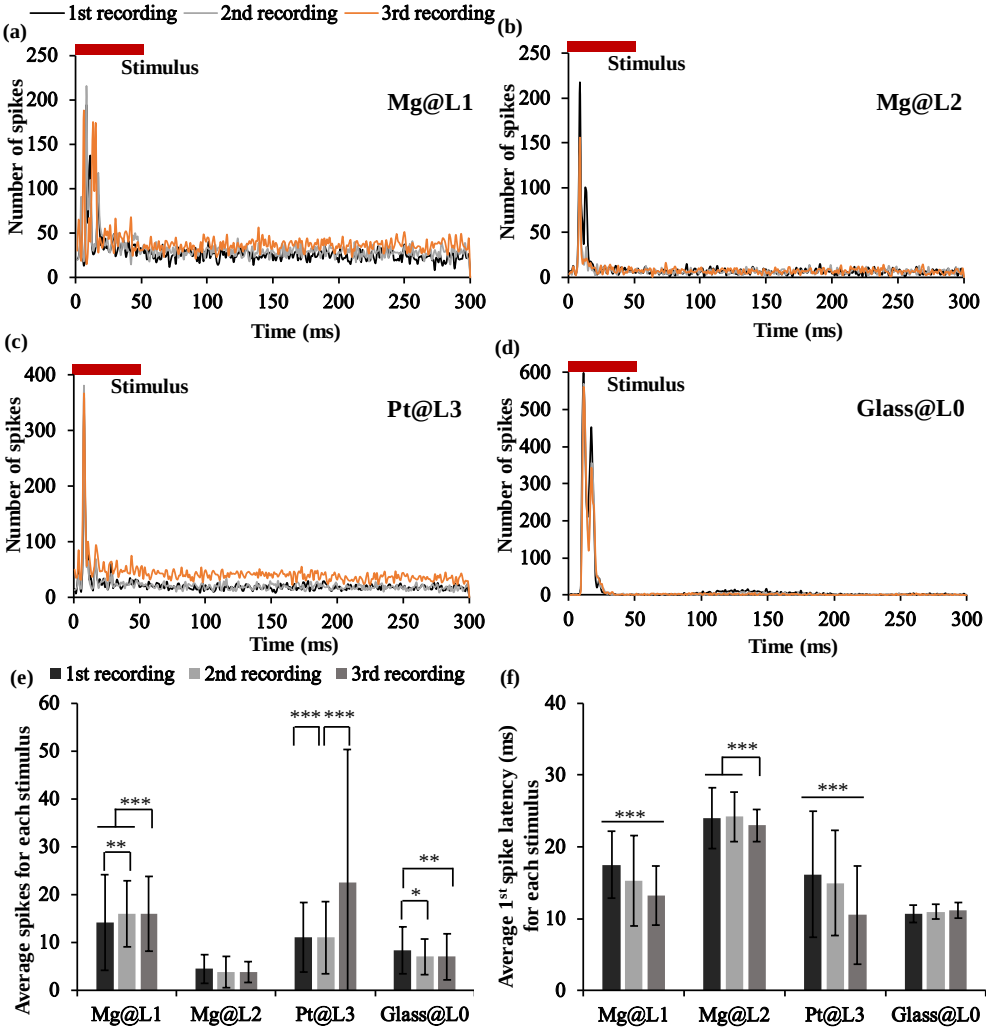

Figure 2-6. Stimulus-evoked recording of Mg@L1, Mg@L2, Pt@L3 and glass@L0 in response to a 50-ms BBN tone with intensity of 30 dB att in a 300-ms recording window. For each electrode at each location, recordings were repeated for 3 times. Each recording took 10 mins with 10 mins of rest between each recording. Repetition rate (RR) was 1 Hz and each recording had 600 times of stimuli. (a-d) Post-stimulus time histogram (PSTH) of (a) Mg@L1, (b) Mg@L2, (c) Pt@L3, and (d) Glass@L0. (e-f) Average spikes for each stimulus and average latency of first spike for each stimulus for Mg@L1, Mg@L2, Pt@L3 and glass@L0. (e) Average spikes for each stimulus. (f) Average latency of first spike for each stimulus. Values are mean ± standard deviation, n = 600; *$p < 0.05$, ** $p < 0.01$, *** $p < 0.001$.

results. The PGS/PEDOT-coated Mg microwire and Pt microwire had a similar diameter and their length immersed in aCSF for EIS testing was the same, and their impedance at 1kHz was similar. However, the PGS/PEDOT-coated Mg microwire had a much smaller conductive tip area than that of Pt control, because the Pt control was not coated with any insulating materials when it was inserted in the mouse brain for neural recording. Higher conductive tip surface area of Pt control could have led to lower impedance in the mouse brain and higher noise signals. Therefore, it is more desirable to insulate Pt control so that it has a similar conductive tip area as PGS/PEDOT-coated Mg microelectrodes. This will be taken into consideration in our future study on *in vivo* neural recording for a longer period of time.

The average spikes for each stimulus and the average latency of the first spike during stimulus-evoked recording were another two important indicators for the recording stability of microelectrodes in the brain. As shown in Figure 2-6e, Mg@L1, Mg@L2 and glass@L0 all exhibited consistent and stable average spikes for each stimulus among three repeated recordings even though some statistically significant differences were found in Mg@L1 and glass@L0 groups, confirming the analysis in Figure 2-6a-d. For Pt@L3, average spikes significantly increased with greater deviation during the third recording, accompanied by increased spontaneous-activity levels, when compared with the first two recording. Figure 2-6f shows the average latency of the first spike for each stimulus for Mg@L1, Mg@L2, Pt@L3 and glass@L0. Only glass@L0 showed no statistically significant difference. The average first spike latency of Mg@L1 was less than 18 ms and decreased during the three recordings. For Mg@L2, the average first spike latency was about 24 ms for all three recordings, and only slight decrease in the average first spike latency was observed from the first two recordings to the third recording. The average first spike latency for Pt@L3 was less than 17 ms and showed a decreasing trend from the first, second to the third recordings. The first spike latency for glass@L0 was ~10 ms and was

consistent and stable with relatively small deviation among the three recording periods. Overall, Mg-based microelectrodes showed better stability than Pt control for neural recording.

Collectively, our PGS/PEDOT-coated Mg microelectrode showed excellent capability and stability for neural recording in brain. The Mg-based microelectrode showed clear onset response and low noise acquisition during 10 mins of spontaneous-activity recording and three repeated 10-min stimulus-evoked recordings at two different recording locations. After multiple neural recordings in the mouse brain *in vivo*, our PGS/PEDOT-coated Mg microwire still well retained surface morphology and composition, and showed stable recordings. This study provided the first *in vivo* evidence on the feasibility of PGS/PEDOT-coated Mg microwire for biodegradable neural electrode applications.

2.3.5. Degradation behaviors of Mg-based microelectrodes in artificial cerebrospinal fluid (aCSF) *in vitro*

2.3.5.1. Microstructural characterization of Mg-based microelectrodes after immersion degradation

It is important to evaluate the degradation behavior of Mg-based microelectrodes after verifying their feasibility for *in vivo* neural recording. Figure 2-7 shows the optical images of Mg-based microelectrodes before and after immersion degradation for 10 days. Degradation was visible for all the samples, but the degradation rates differed. PP_Mg retained its structure after 4 hours of immersion, and appeared to have rougher surfaces as the immersion time increased. After 10 days of immersion, coating delamination occurred on PP_Mg, but the microelectrodes retained their structural integrity. In contrast, P_Mg showed visible loss of PEDOT coating in several areas and its surface became heterogeneous after 4 hours of immersion. After 5 and 10 days of immersion, P_Mg sample showed more coating loss than the PP_Mg sample; and two of

P_Mg triplicates fractured to 2 pieces. Pure Mg control exhibited a dark surface after 4 hours of immersion, indicating oxidation; and Mg microwire retained its shape and structure after 10 days

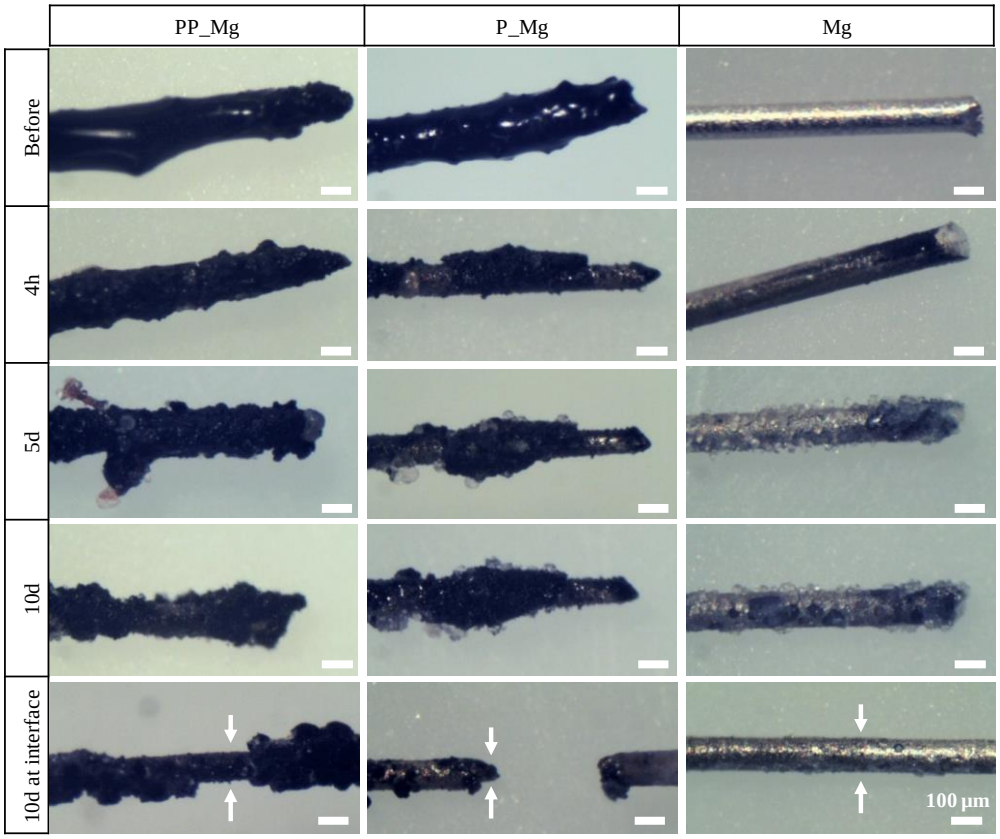

Figure 2-7. Optical images of PP_Mg, P_Mg and Mg control at each prescribed time point for 10 days of immersion in aCSF. The sample areas shown in all images were submerged in aCSF during immersion except the bottom row for the images at the interface after 10 days of immersion. The white arrow indicated the sample region at the interface between media and gas environment during immersion. The left part of the white arrow was immersed in aCSF and the right part was exposed to the gas environment in a standard incubator. The scale bar was 100 µm for all images.

of immersion. In addition, severe degradation and coating loss were observed at the liquid-gas interface for PP_Mg and P_Mg samples, where the microelectrodes crossed from the immersion media to the gas environment (i.e., 5% CO_2 and 95% air in a standard incubator). Specifically, after 10 days of immersion, P_Mg fractured at that interface; the coatings on PP_Mg delaminated

at that interface but the PP_Mg microelectrodes did not fracture. Clearly, PGS coating protected PEDOT coating from delamination and decreased the overall electrode degradation.

Surface topography and elemental composition of PP_Mg, P_Mg and Mg control after 10 days of immersion in aCSF were further characterized using SEM and EDS, as shown in Figure 2-8. More calcium (Ca) and phosphorus (P) were detected on the surface of Mg, indicating more

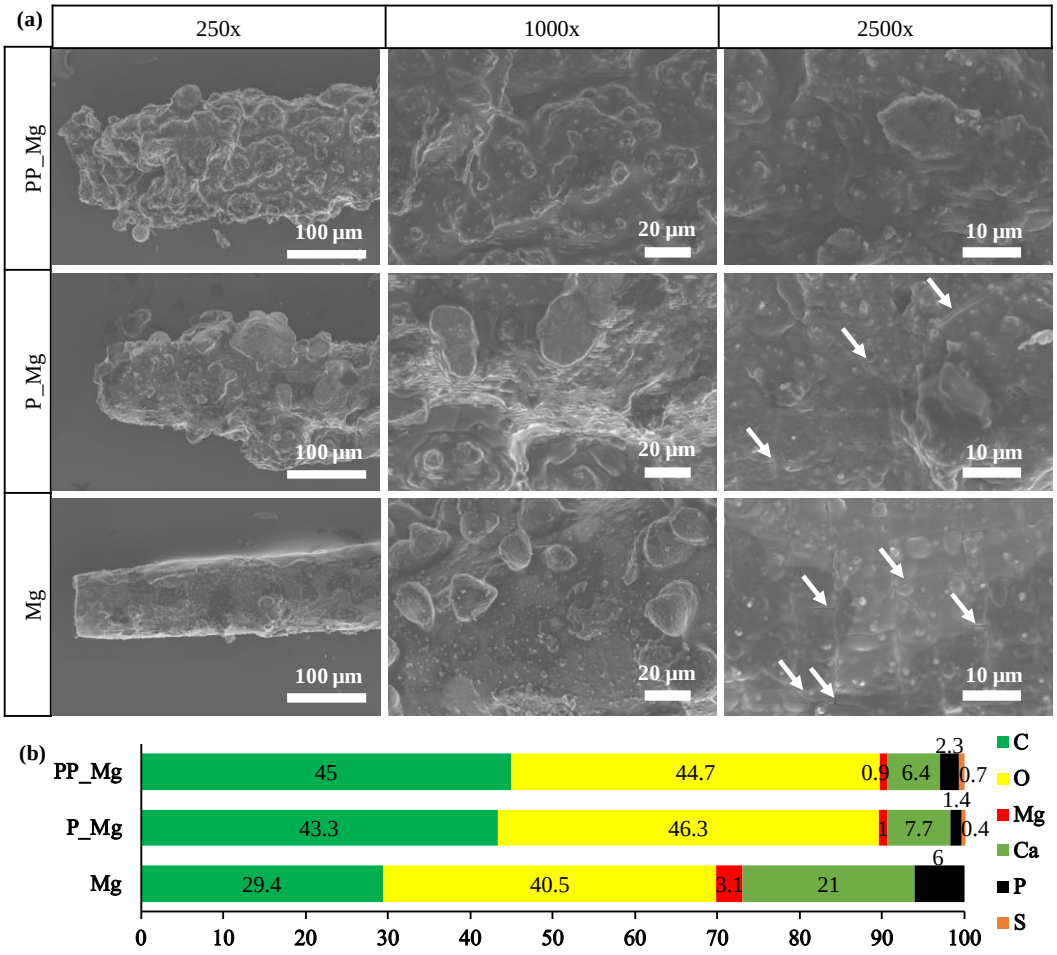

Figure 2-8. Surface topographies and elemental compositions of PP_Mg, P_Mg and Mg control after 10 days of immersion in aCSF. (a) SEM images of all samples at original magnification of 250x, 1000x and 2500x. The white arrow indicated the corrosion cracks on the sample surfaces. (b) EDS area analysis of all samples at original magnification of 1000x in (a).

mineral deposition on pure Mg control than on the surfaces of PP_Mg and P_Mg. Moreover, in the SEM images from low to high magnifications, PP_Mg did not show visible cracks, but P_Mg showed some visible cracks. Not surprisingly, the surface of pure Mg control exhibited even more cracks than that on the surface of P_Mg. Generally, the polymer coatings reduced Mg degradation and mineral deposition.

2.3.5.2. Media analysis after in vitro immersion of Mg-based biodegradable microelectrodes

The results of media analysis, including pH and ion concentrations of Mg^{2+} and Ca^{2+} are plotted in Figure 2-9. In Figure 9a, all immersion media with Mg-based microelectrodes showed significant pH increase at all the time points during 10 days of immersion, when compared with the aCSF blank control. Initially, PP_Mg showed lower pH in the immersion media than that of P_Mg and Mg. After 10 days, all the media for different types of samples showed a similar pH. In Figure 2-9b, Mg^{2+} ion concentration in the immersion media with PP_Mg was the lowest after 4 hours of immersion (even lower than the blank aCSF), indicating slower degradation and deposition of Mg-containing minerals, in agreement with the SEM and EDS results in Figure 2-8. The Mg control showed the highest Mg^{2+} ion concentration after 4 hours of immersion, indicating the fastest degradation at the beginning. At the time points of 1 day to 10 days, PP_Mg and P_Mg showed similar Mg^{2+} ion concentrations as the aCSF blank control, while pure Mg control showed the lowest Mg^{2+} ion concentration. Possibly for PP_Mg and P_Mg samples, Mg^{2+} ions formed a balance between release and deposition; the Mg control likely induced more deposition of Mg-containing minerals than the polymer coated Mg. In Figure 2-9c, Ca^{2+} ion concentrations in the immersion media with Mg-based microelectrodes were significantly lower than the aCSF blank control at most time points, indicating deposition of Ca-containing minerals onto these samples. The Mg control showed the lowest Ca^{2+} ion concentrations at the time points of 4 hours,

1 day and 3 days, and the PP_Mg group showed the lowest Ca^{2+} ion concentrations at the time points of 7 and 10 days. Ca^{2+} ion concentrations in Figure 2-9c indicated that Mg control induced more deposition of Ca-containing minerals than PP_Mg initially. Overall, pH and ion concentration change in the media could provide information of the activities occurred in the

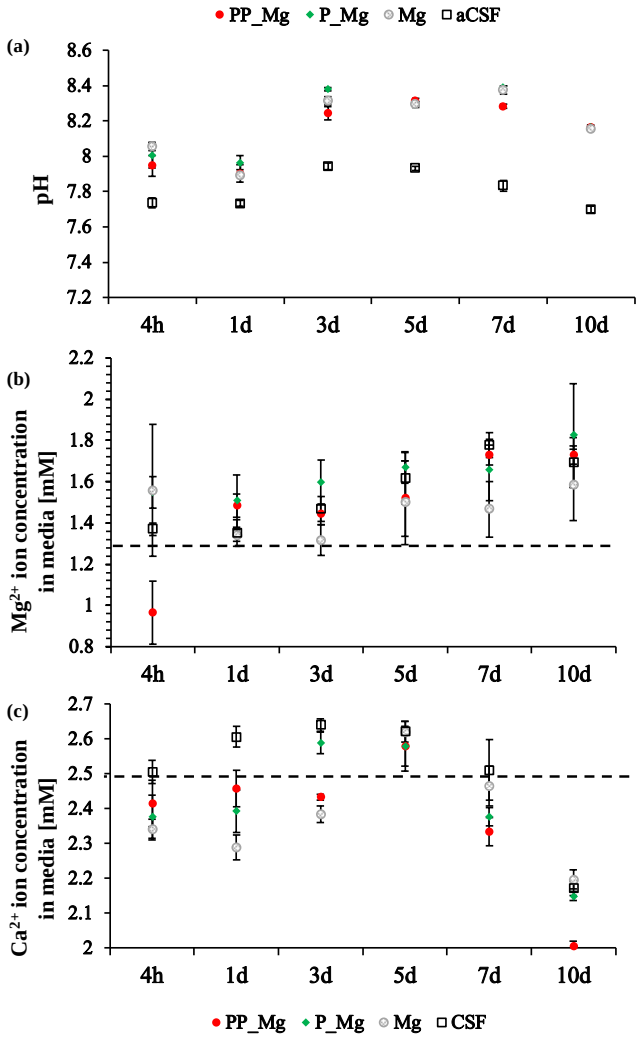

Figure 2-9. (a) The pH of collected aCSF after cultured with PP_Mg, P_Mg and Mg control at different time points. (b) Mg^{2+} ion concentrations in the collected aCSF after cultured with each sample at different time points. The Mg^{2+} ion concentration in the originally prepared aCSF was 1.3 mM. (b) Ca^{2+} ion concentrations in the collected aCSF after cultured with each sample at different time points. The Ca^{2+} ion concentration in the originally prepared aCSF was 2.5 mM. Data are mean ± standard deviation (N=3).

media due to the degradation of Mg, such as pH increasing, Mg^{2+} ions releasing, the deposition of Mg-containing and Ca-containing minerals. However, we could not conclude which sample degraded fastest just based on it. Taking together with the results of surface morphology and composition change in Figure 2-7 and Figure 2-8, we could have a comprehensive understanding of the degradation behavior of Mg-based microelectrodes and it is clear that PGS/PEDOT-coated Mg showed slower degradation rate than PEDOT-coated Mg while pure Mg is not suitable for neural recording because of quick oxidization.

2.3.5.3. Electrochemical impedance of Mg-based microelectrodes after immersion degradation

Figure 2-10 shows the electrical properties of Mg-based microelectrodes before and after 10 days of immersion in aCSF. At 1 kHz, the impedance of PP_Mg increased from 1105±67 Ω to 2695±181 Ω after 4 hours of immersion, and further increased to 214466±27555 Ω after 10 days of immersion. In contrast, the impedance of P_Mg was 45727±5648 Ω after 4 hours of immersion, which was much higher than that of PP_Mg. After 10 days of immersion, P_Mg microwires fractured, which was not suitable for impedance testing. The Mg control showed an impedance of 3260±320 Ω before immersion, and 11133±723 Ω and 21010±1486 Ω after 4 hours and 10 days of immersion, respectively.

Overall, PGS/PEDOT-coated Mg electrodes showed slower degradation than PEDOT-coated Mg electrodes in 10 days of *in vitro* immersion. The PGS coating protected PEDOT coating from delamination in the initial stage of immersion in aCSF. PGS/PEDOT-coated Mg showed less loss in mechanical and electrical properties than that of PEDOT-coated Mg, which is beneficial for *in vivo* neural recording at a longer period.

2.3.6. Potential of Mg-based biodegradable implantable microelectrodes toward clinical translation

PGS/PEDOT-coated Mg electrodes integrated the beneficial properties of Mg, PEDOT and PGS synergistically for neural recording and stimulation. Our results provided the first *in vivo* evidence on the feasibility, capability, and stability of Mg-based biodegradable microelectrodes for multi-unit neural recording. Based on the previous results on neuro-protective effects and biocompatibility of Mg [30, 83], electrical properties and biocompatibility of PEDOT [101-103], and mechanical properties and biocompatibility of PGS [85, 86] for medical applications, our assembly of PGS/PEDOT-coated Mg microwires is expected to provide controllable degradation, functional stability, and biocompatibility for implantable neural device applications.

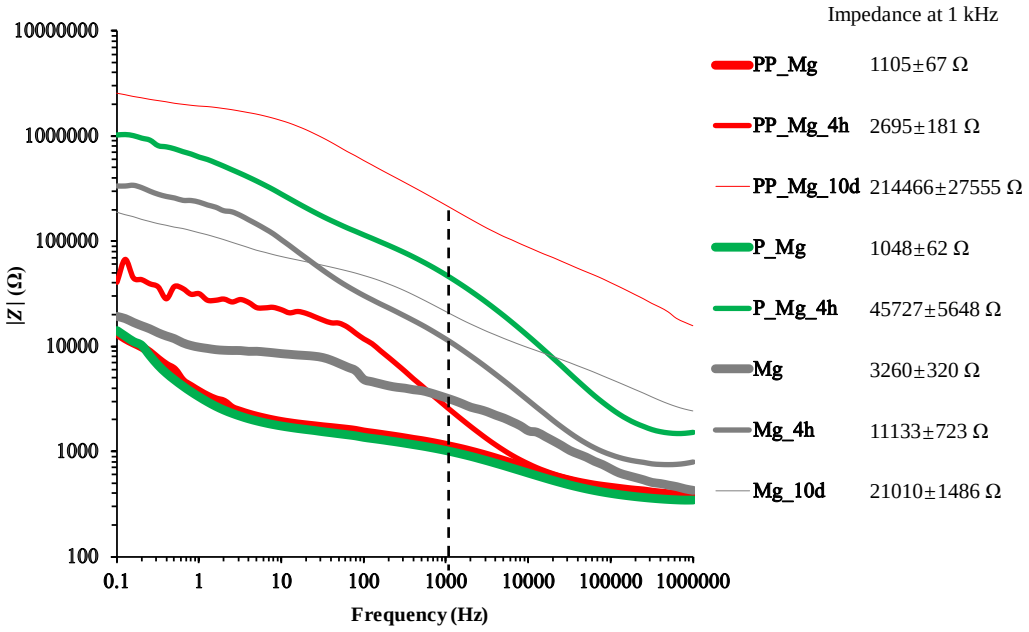

Figure 2-10. Bode representation of the typical impedance spectra for PP_Mg, P_Mg and Mg in aCSF before immersion, after 4 hours of immersion (labeled as _4h), and after 10 days of immersion (labeled as _10d). The average impedance value and standard deviation for each sample at 1000 Hz was listed on the right of respective sample labels.

2.3.6.1. Functional stability of Mg-based microelectrodes for neural recording

Conductive polymers, such as polypyrrole (PPy) and PEDOT, have been deposited onto traditional metallic electrodes to improve their electrical properties, reduce mechanical mismatch between tissue and electrodes, and enhance signal-to-noise ratio for recording [37, 98]. For electrodes with a size of 10 nm-10 μm, the impedance of conductive polymer-based electrodes at 1 kHz is typically around 10-100 kΩ, which is significantly less than the impedance of non-coated metal electrodes (typically around 200-500 kΩ) [25, 37, 55]. Moreover, polymer coating could provide a rough surface with large conducting surface area and charge density. Harris et al. used PPy and PEDOT doped with sulfate (SO_4^{2-}) or para-toluene sulfonate (pTS) to coat iridium electrodes for neural recording [55]. The coatings of conductive polymers provided greater charge density and lower impedance than non-coated electrodes. During recording, the coated electrodes showed a general decrease in background noise and increase in the signal-to-noise ratio and spike count. Venkatraman et al. prepared PEDOT coated Platinum Iridium (PtIr) electrodes for neural stimulation and recording [39]. During chronic testing in rat cortex *in vivo*, the PEDOT coated PtIr electrodes showed much higher signal-to-noise ratio in the recordings and greater charge injection than that of PtIr control electrodes. Therefore, conductive polymer coatings have been successfully used for inert metal electrodes. In addition to improving the electrical properties, polymer coatings on Mg substrates can serve as a protective layer and potentially moderate the degradation behaviors of Mg. As mentioned previously, PEDOT is a conductive polymer that has been deposited onto various metallic electrodes for neural applications due to its excellent biocompatibility and high electrical conductivity [32, 35, 37, 39, 40, 103-105]. Moreover, deposition of PEDOT onto Mg could potentially reduce the mechanical mismatch at the interface of electrode and neural tissues [25] due to the lower Young's modulus (E) of PEDOT than Mg (E_{PEDOT} = 1-5 GPa [84], E_{Mg} = 41-45 GPa [42]). However, the Young's

modulus of neural tissues (E_{CNS} = 3-10 kPa [40, 52], E_{PNS} = 400-700 kPa [53, 54]) is still much lower than PEDOT. Some researchers doped a second polymer or hydrogel into conductive polymers to form a conductive hybrid electrode [106, 107]. The key challenges in forming an appropriate hybrid electrode lie in combining the conductive polymer and non-conductive polymer component to achieve the overall balanced properties including desired electrical activities, and mechanical properties such as stiffness and elasticity. Therefore, a second polymer with similar Young's modulus as neural tissues, should be used as an insulating coating for PEDOT-coated Mg electrodes to further reduce the mechanical mismatch between the neural tissues and electrodes and to further decrease Mg degradation rate.

PGS is a promising biodegradable polymer widely studied for soft tissue engineering applications because of its flexible and elastomeric nature [85, 86, 108-117]. PGS has a Young's modulus of 20-1200 kPa [85, 86], which is much closer to neural tissues than metals and other polymers. Moreover, it has been well established that PGS undergoes surface degradation, which is preferred over bulk degradation for neural applications. Specifically, the loss of mechanical strength for surface-degrading polymers such as PGS is slow and gradual, while the mechanical strength of bulk-degrading polymers decreases dramatically in advance of mass loss. Moreover, all the degradation products of PGS, i.e., glycerol and sebacic acid can be metabolized naturally in the body [91, 118]. PGS was coated onto PEDOT surface as an insulating layer to further improve the interfacial compatibility of Mg-based electrodes with neural tissue, and thus reduce tissue trauma when inserting the electrodes. The very tip of electrode was coated with PEDOT but not PGS to retain conductivity for capturing electrical signals. In neural recording *in vivo*, PEDOT-coated Mg and non-coated Mg microelectrodes were not used as control electrodes for the following reasons. PEDOT coating on Mg could still delaminate while inserting the electrode into the mouse brain, even though the parameters for electrochemical deposition of PEDOT onto

Mg were optimized to achieve dense and uniform coating and improve the adhesion strength between PEDOT coating and Mg substrate [32, 90]. Moreover, the impedance of PEDOT-coated Mg significantly increased after 4 hours of immersion in aCSF (Figure 2-10). Thus, PEDOT-coated Mg microelectrodes were not stable to last long *in vivo*, because the delamination of PEDOT coating could induce fast degradation of Mg and unstable electrical properties of electrodes. Non-coated Mg microelectrodes became oxidized immediately in contact with body fluids before any signals being captured. As a result, the degradation layer containing magnesium oxide (MgO) and hydroxide ($Mg(OH)_2$) formed on Mg surface, which significantly increased the impedance after 4 hours of immersion in aCSF (Figure 2-10), making bare Mg unsuitable for neural recording. After 10 days immersion, the impedance of non-coated Mg microelectrodes just changed a bit when comparing with 4 hours immersion data point because of the protection of oxidized layers. The impedance of PGS/PEDOT-coated Mg exhibited no significant difference after 4 hours immersion due to the protection of PGS but increased a lot after 10 days immersion because of the combined effect of oxidation of Mg and changes in surface properties of PEDOT. However, it should still be able to perform neural recording since the integrity of electrode didn't loss. It is worth to mention that the degradation and functional service-time of Mg-based electrodes is related to the thickness of PEDOT and PGS coating. The PEDOT coating thickness has been previously investigated under different electrochemical deposition parameters [90]. The optimized parameters produced dense, uniform, and smooth PEDOT coating on Mg with a consistent PEDOT coating thickness of 15 μm that fully covered the Mg substrates. To achieve successful neural recording *in vivo*, PGS coating with a cone shape was applied on PEDOT-coated Mg microwires to protect PEDOT coating; the thickness of PGS coating at the bottom of the cone (the thickest part) was 118 μm (Figure 2-2a). However, a thinner PGS coating of around 5 μm was used for *in vitro* immersion degradation study so that we can observe PEDOT

delamination and Mg degradation in a period of 10 days. The functional service-time for PGS/PEDOT-coated Mg microelectrodes is expected to be at least 10 days based on the initial *in vitro* degradation study. The thickness of PGS coating can be easily adjusted to prolong or shorten the functional service time of Mg-based biodegradable microelectrodes, which will be explored in the future studies. Therefore, PGS coating is needed to protect PEDOT coating from delamination and reduce mechanical mismatch between tissue and electrodes; only PGS/PEDOT-coated Mg microwires demonstrated successful neural recording *in vivo* in the mouse brain.

2.3.6.2. Controllable degradation and biocompatibility of Mg-based microelectrodes for neural recording

Clearly, both PEDOT coating and PGS coating are needed to protect the Mg microwire substrate from rapid degradation, and to reduce the release of degradation products during the service period of Mg-based microelectrodes. PGS could degrade surface by surface during the initial functional time to prevent PEDOT and Mg from fast degradation. After serving the functions of recording or stimulation in the central nerve system, PGS coating has degraded totally and then the biodegradable substrates and conductive polymer coating, Mg and PEDOT, could slowly degrade in the brain and thus eliminate the necessity for surgical removal. At this time, it is desirable that the Mg substrate degrades slowly and releases Mg^{2+} ions gradually, which could provide neuro-protective effects for surrounding neuronal tissue [30, 83]; While PEDOT coating degrades as well and releases small PEDOT particles that could be safely eliminated from the body when the particle size and release rate are controlled at an acceptable level [88, 119].

It has been shown that PEDOT could undergo structural changes during the degradation process [119, 120]. The most probable stages involved in the degradation process are: 1)

Overoxidation results in stress generation in the PEDOT film. 2) Formation of cracks due to internal stress. 3) The products of the degradation of the polymer leave the polymer layer. 4) After the formation of the line cracks, the film stress is partially released. 5) The partial delamination of the polymer layer leads to the exposure of the underlying metal substrate to the solution [119, 120]. Our *in vitro* immersion study results (Figure 2-7 and Figure 2-8) have clearly showed the delamination of PEDOT during degradation, which is in agreement with previous findings. Both PEDOT [101-103] and its degradation products [88] possess excellent biocompatibility *in vitro* and *in vivo*. PEDOT was reported to be cytocompatible with cells, e.g., myocytes, and it successfully supported cellular proliferation and differentiation [101]. PEDOT also showed no cytotoxicity and no difference in immunological responses in cortical tissue when compared with pure Pt controls [102]. No inflammatory reactions were observed after PEDOT coated glass substrates were subcutaneously implanted into mice for a week [103]. More importantly, PEGylated PEDOT: PSS (polystyrene sulfonate) nanoparticles were intravenously injected into mice at a dosage of 10 mg/kg and showed no apparent toxicity after 40 days based on the blood tests and histological examination [88]. Since the mass of our whole microelectrode is less than 0.5 mg, the mass of PEDOT coating should be much smaller than 0.5 mg. Therefore, the degradation of PEDOT coating should not have toxicity during the long-term electrode implantation for neural recording. To further investigate the degradation and biocompatibility of PEDOT, we will do *in vivo* neural recording for an implantation period of weeks to months to investigate the electrode surface changes, PEDOT coating degradation pathway and their interactions with neural tissues.

PGS has excellent biocompatibility [85, 86] because all the degradation products of PGS can be metabolized naturally in the body. Glycerol is generally considered to be safe and is listed on the GRAS list, that is, generally regarded as safe, on the FDA website [118]. Sebacic acid is a

naturally occurring dicarboxylic acid and an intermediate metabolic product in ω-oxidation of certain fatty acids [91]. *In vitro* studies with Schwann cells revealed that PGS had no deleterious effect on the metabolic activity, attachment or proliferation of cells [85]. After *in vivo* implantation juxtaposed to the sciatic nerve, PGS demonstrated a favorable tissue response profile compared with PLGA, with significantly less inflammation and fibrosis and without detectable swelling during degradation [85]. These studies confirmed that PGS is a promising candidate material for neural applications [85]. Therefore, Our PGS/PEDOT-coated Mg microwires should provide good biocompatibility for implantable neural electrodes, but it is still necessary to perform long-term studies on the Mg-based microelectrodes *in vivo* in the future.

Overall, the PGS/PEDOT-coated Mg microwires showed great potential for use as implantable neural electrodes that degrade and disappear in the body after serving their recording or stimulation functions. Once PGS degrades to certain extent, PEDOT could release small particles *in vivo* that could be safely eliminated from the body when the particle size and release rate are controlled at an acceptable level. The body fluids could penetrate through PEDOT coating and react with Mg substrates to degrade the whole electrode eventually. The current assembly of Mg-based microelectrode is feasible for acute multi-unit neural recording in the brain and serves as the first step in demonstrating the capability and stability of Mg-based biodegradable electrodes as implants for neural recording. The design and assembly of Mg-based microelectrodes will be further optimized in the future studies to meet all the requirements for implantable neural electrodes, while being compatible with specific animal models for preclinical testing. To build the foundation for potential clinical translation, the degradation behaviors of Mg-based microelectrodes, their functional stability, and their interactions with neural tissues will also be investigated in the future for an *in vivo* implantation period of weeks to months.

2.4 Conclusions

This study provided the first *in vivo* evidence on the feasibility of Mg-based biodegradable microelectrodes for neural recording in the auditory cortex. Mg-based microwires with functional polymer coatings demonstrated excellent signal-to-noise ratio and repeatability with minimal tissue damage for neural recording inside the brain. We successfully designed and fabricated PGS/PEDOT-coated Mg microwires with high homogeneity in coating thickness, surface morphology and composition for biodegradable neutral electrode applications. Mg-based biodegradable microelectrodes could eliminate the necessity of additional surgeries for removing the electrodes when they are no longer needed clinically. The CSC of PGS/PEDOT-coated Mg microwire (1.72 mC/cm^2) was almost 5 times higher than the standard Pt microwire currently used in implantable electrodes for neural recording and stimulation. During *in vivo* neural recordings in the auditory cortex of a mouse, the PGS/PEDOT-coated Mg microelectrode exhibited excellent neural recording ability and stability. Specifically, the Mg-based microelectrode showed clear and stable onset response, low and consistent noise acquisition during 10-min spontaneous-activity recording and three repeated 10-min stimulus-evoked recordings at two different recording locations. After neural recordings in the brain of a mouse, the PGS/PEDOT-coated Mg microelectrode was still robust and showed similar surface morphology and elemental composition as before recording. During 10 days of *in vitro* degradation in aCSF, PGS/PEDOT-coated Mg microelectrodes showed slower degradation with less PEDOT delamination, and retained better structure with less impedance change than PEDOT-coated Mg electrodes because of the protection from biodegradable PGS coating. The functional service-time for PGS/PEDOT-coated Mg microelectrodes is expected to be at least 10 days based on the initial *in vitro* degradation study. Overall, the PGS/PEDOT-coated Mg microwires demonstrated promising potential as implantable and biodegradable microelectrodes

for neural applications; the *in vivo* degradation of Mg-based microelectrodes and their functional lifetime for neural recording and stimulation should be further studied in specific animal models toward clinical translation.

Chapter 3 Antimicrobial Bioresorbable Mg-Zn-Ca Alloys for Bone Repair in a Comparison Study with Mg-Zn-Sr Alloys and Pure Mg

Abstract

Magnesium-zinc-calcium (Mg–Zn–Ca) alloys have attracted increasing attention for biomedical implant applications, especially bone repair, because of their biocompatibility, biodegradability and similar mechanical properties to human bone. The objectives of this study were to characterize Mg–2wt.% Zn–0.5 wt.% Ca (named ZC21) alloy pins microstructurally and mechanically, and determine their degradation and interactions with host cells and pathogenic bacteria *in vitro* and *in vivo*. Specifically, the *in vitro* degradation and cytocompatibility of ZC21 pins with bone marrow derived mesenchymal stem cells (BMSCs) were investigated using both direct culture and direct exposure culture methods. The adhesion density of BMSCs on ZC21 pins (i.e., direct contact) was significantly higher than on pure Mg pins in both *in vitro* culture methods; the cell adhesion density around ZC21 pins (i.e., indirect contact) was similar to the cell-only positive control in both *in vitro* culture methods. Interestingly, ZC21 showed a higher daily degradation rate, crack width and crack area ratio in the direct exposure culture than in the direct culture, suggesting different culture methods did affect its *in vitro* degradation behaviors. When cultured with gram-positive bacteria *methicillin-resistant Staphylococcus aureus (MRSA)*, ZC21 reduced bacterial adhesion on the surface more significantly than that of Mg–4 wt.% Zn–1 wt.% strontium (named ZSr41) and Mg. The *in vivo* degradation and biocompatibility of the ZC21 pins for bone regeneration were studied in a mouse femoral defect model. The *in vivo* degradation rate of ZC21 pins was much slower than that of ZSr41 alloy and Mg control pins. After 12 weeks of implantation *in vivo*, the ZC21 group showed the shortest gap at the femoral defect, indicating that ZC21 pins promoted osteogenesis and bone healing more than ZSr41 and Mg control pins. Overall, the ZC21 alloy is promising for bone repair while providing antibacterial activities, and should be further studied toward clinical translation.

3.1 Introduction

Magnesium (Mg) and its alloys have emerged as a new class of bioresorbable materials that are promising for orthopedic and craniofacial implant applications. Mg alloys provide similar mechanical properties to human bone [121], support bone growth and potentially address the stress-shielding issues associated with titanium (Ti) alloys and cobalt-chromium (Co-Cr) alloys [3, 16, 122-126]. Mg naturally degrades in physiological fluids by reacting with water, and the degradation products can be metabolized effectively by human body, which eliminates the need for a secondary surgery for implant removal after the tissue has healed [13, 78, 127]. Unfortunately, pure Mg degrades too rapidly to be directly used for orthopedic implants, because rapid degradation causes a sharp increase of local pH, fast accumulation of hydrogen gas (H_2) bubbles, and premature loss of mechanical strength [2, 78, 82, 122]. Thus, it is critical to control and improve the degradation rate of Mg for successful clinical translations. Adding alloying elements to Mg has been extensively explored to slow Mg degradation and H_2 evolution [81, 128].

Selecting suitable alloying elements is critical to the mechanical properties, degradation behaviors and biological properties of Mg-based alloys, because alloying elements and compositions have crucial effects on the microstructure, phase distribution, and biocompatibility of Mg-based alloys [74, 128, 129]. Metallic alloying elements such as aluminum (Al) and yttrium (Y) are widely used to improve corrosion resistance and/or mechanical strength of Mg [130], but their biocompatibility poses a serious concern. Therefore, development of Mg-based alloys with elements that are naturally present in the human body, such as zinc (Zn), calcium (Ca), and strontium (Sr), have attracted increasing interest for medical implant applications [1-3, 77, 80, 131-138]. Zn is involved in over 300 enzymatic processes in the human body [139]. The addition of Zn as an alloying element in Mg could reduce grain size [140], enhance corrosion resistance,

provide solid solution and aging strengthening [128], and improve tensile and creep strength [141]. As reported, the addition of 1–4 wt.% Zn in Mg-Zn alloys increased the ultimate tensile strength and the alloy elongation significantly [142]. Therefore, the biocompatibility and corrosion resistance of Mg alloyed with 1-4 wt.% Zn have been widely studied *in vitro* and *in vivo* [1, 2, 137, 138, 141-144]. Mg–Zn alloys with low Zn content can be further modified by adding third alloying elements, such as Ca [80, 129, 145]. Ca is a major component of bone, and is essential for a variety of cellular functions [129]. Ca also shows a great microstructure-refining effect on Mg alloys [128]. As reported, adding 0.5–1.0 wt.% Ca reduced the grain size of Mg alloys [146]. However, the addition of larger amounts of Ca (>1.0 wt.%) accelerated the degradation rates of Mg alloys. Therefore, the optimal composition of Ca in Mg alloys should be less than (≤) 1.0 wt.% [147, 148].

In our previous study, as-cast Mg–2 wt.% Zn–0.5 wt.% Ca (named ZC21) alloy plates showed the best collective properties, including degradation properties and cytocompatibility with bone marrow derived mesenchymal stem cells (BMSCs), among four tested Mg–xZn–0.5 wt.% Ca (x = 0.5, 1.0, 2.0, 4.0 wt.%) alloy plates using the direct culture method *in vitro*[1]. Therefore, the ZC21 alloy was selected based on the previous results and fabricated into the form of wires (or pins) for further studies toward clinical translation. The objectives of this study are to determine the degradation of ZC21 alloy pins, and their interactions with host cells and pathogenic bacteria *in vitro* and in *vivo*. Specifically, the *in vitro* degradation and cytocompatibility of ZC21 pins with BMSCs in Dulbecco's modified Eagle medium (DMEM) were studied using both direct culture and direct exposure culture methods [149]. The direct culture method is suitable for evaluating attachment of directly seeded cells on the biomaterial surface, while the direct exposure culture method allows us to study the responses of well-established cells to ZC21 alloys and the effects of these established cells on alloy degradation *in*

vitro. Both direct culture and direct exposure culture methods resemble *in vivo* conditions closely with the presence of physiologically relevant ions, proteins, and cells [149]. Furthermore, ZC21, Mg–4 wt.% Zn–1 wt.% strontium (named ZSr41) and Mg pins were cultured with gram-positive bacteria methicillin-resistant Staphylococcus aureus (MRSA) to determine their antibacterial activities. Finally, a mouse femoral defect model was used to study *in vivo* degradation of ZC21 pins and associated biological responses for bone regeneration for the first time. This comparation study focuses on *in vitro* versus *in vivo* evaluation of ZC21 alloy pins for orthopedic applications, and bridges the critical knowledge gap on ZC21 alloys toward clinical translation in the future.

To highlight the significance of this study, recent development of Mg–Zn–Ca ternary alloys (since 2014) has been summarized in Table 3-1 [150-159]; and the history of Mg-Zn-Ca alloys for biomedical applications before 2014 has been reported in our previous publication [1]. As shown in Table 1, different aspects of Mg-Zn-Ca alloys have been studied in recent years; for example, some work focused on the degradation behaviors of Mg-Zn-Ca alloys *in vitro* [41, 42, 44, 46-49] while others focused on the biocompatibility of Mg-Zn-Ca alloys [43, 45, 50]. To our knowledge, this is the first comparison study on characterization, mechanical properties, degradation behaviors, antibacterial properties, and biocompatibility of a promising Mg-Zn-Ca alloy *in vitro* and *in vivo*, which provides a comprehensive picture on the potential of Mg-Zn-Ca alloys for clinical translation when compared with pure Mg and a previously studied Mg-Zn-Sr alloy [2, 3, 10, 87, 123, 160].

Table 3-1. The development of Mg–Zn–Ca ternary alloys since 2014[150-159]. Remarks summarize the key information of interest from the literature. Different Zn content and Ca content in Mg-Zn-Ca alloys are reviewed and listed in the table; the rest is Mg.

Year	Ref.	Processing	Zn content	Ca content	Focus	Remarks
2014	[150]	as-cast	1.74 wt.%	0.55 wt.%	Degradation *in vitro*	Microarc oxidation (MAO) coating on the surface of Mg alloy
2014	[151]	as-cast	3 wt.%	0.3 wt.%	Degradation *in vitro*	Studied the effects of secondary phase and grain size on the corrosion
2015	[1]	as-cast	0.5, 1.0, 2.0, 4.0 wt.%	0.5 wt.%	Degradation and cytocompatibility *in vitro*	the first report of *in vitro* cell responses at the dynamic interface and mechanisms
2015	[152]	extruded	5 wt.%	0.3 wt.%	Degradation *in vitro* and *in vivo*	Investigated the influence of trace impurities on degradation
2015	[153]	as-cast	30 at.% (52.5 wt.%) Zn with 4 at.% (4.3 wt.%) Ca; 35 at.% (58.0 wt.%) Zn with 5 at.% (5.1 wt.%) Ca		Degradation *in vitro*	Emphasized the role of partially amorphous structure and alloying elements on the corrosion behavior
2015	[154]	as-cast	1 wt.%	5 wt.%	Degradation and biocompatibility *in vivo*	1-year clinical study and systematic investigation of bone formation mechanism
2016	[155]	extruded	2 wt.%	0.2 wt.%	Fatigue behaviors	Compared the fatigue behaviors in air and simulated body fluid
2016	[156]	extruded	3 and 4 wt.%	0.2 wt.%	Degradation *in vitro*	Investigated the influences of Zn content on the microstructure, mechanical properties, and corrosion and wear behavior
2016	[157]	extruded	2 wt.%	0.24 wt.%	Degradation *in vitro*	Processed by high pressure torsion to improve the corrosion resistance
2018	[158]	as-cast	31 at.% (53.6 wt.%) Zn with 5 at.% (5.3 wt.%) Ca; 24 at.% (45.0 wt.%) Zn with 5 at.% (5.7 wt.%) Ca		Degradation *in vitro*	Explained the influence of microstructure and composition on degradation
2018	[159]	extruded	5.25 wt.%	0.6 wt.%	Biocompatibility *in vitro* and *in vivo*	Compared *in vitro* and *in vivo* corrosion performance
2019	This study	as-drawn	2 wt.%	0.5 wt.%	Degradation, antibaterial and biological performance *in vitro* and *in vivo*	Systematically investigated the biocompatibility, mechanical properties, corrosion, degradation behavior and antibacterial properties of a promising Mg-Zn-Ca alloy for the first time

3.2 Materials and Methods

3.2.1. Preparation of ZC21 pins and controls

ZC21 alloy in this study had a nominal composition of 2.0 wt.% Zn and 0.5 wt.% Ca in the Mg matrix. The alloy was produced by a metallurgical process consisting of melting, casting,

extrusion and drawing. Briefly, a stainless steel crucible was first preheated in an electrical-resistance furnace (Shenyang General Furnace Manufacturing Co., Ltd) to 400–500 ℃, with 1.515 MPa argon (Ar) gas blowing into the furnace at a flow rate of 5 L/min to remove air. Pure Mg ingots (99.94 wt. %; Boyu, Shenyang, China) were melted at a temperature of 700–730 ℃ in the stainless steel crucible under an Ar gas-protected environment to avoid oxidation, followed by removal of the surface scum. Commercially available bulk metallic Zn (99.5%; Boyu, Shenyang, China) and Mg-15Ca (wt.%) intermediate alloy (Boyu, Shenyang, China) were added to the molten Mg, stirred, and heated at 750℃ for 20 min with Ar protection. After degassing with hexachloroethane and deslaging to ensure purity of the alloy, the molten mixture was cast at 720 ℃ in a cone-shaped cast iron mold and cooled down in the air. The cone-shaped mold had a bottom diameter of 50 mm, a top diameter of 70 mm, a height of 135 mm, and a wall thickness of 10 mm. The as-cast ingots were machined to rods with a diameter of 40 mm and a length of 100 mm for extrusion, and homogenized at 450 ℃ for 6 h. The 40-mm rods were then hot extruded at 250 ℃ with an extrusion ratio of 10:1 using a four-column hydraulic press (300 tons; Shandong Machinery Factory) to produce ZC21 rods with a diameter of 4 mm. Finally, the 4mm alloy rods were drawn into a wire of1mm diameter at 20℃ through multiple passes, i.e., 4→3.5→3.0→2.8→2.7→2.6→2.5→2.4→2.3→2.2→2.1→2.0→1.9→1.8→1.7→1.6→1.5→1.4 →1.3→1.2→1.1→1.0 mm, using a continuous wire drawing machine. Heat treatment was performed for the work piece at 300℃ for 30 minutes between each drawing pass.

Pure Mg wires were prepared using the same Mg source of the same purity of 99.94% and the same processing parameters of melting, casting, extrusion and drawing as for producing ZC21 alloy wires, to serve as a pure Mg control in this study. ZSr41 alloy, i.e., Mg–4 wt.% Zn–1 wt.% strontium (Sr) alloy, was prepared using the same method as described in the previous publication [2], and was included for comparison because it has been studied both *in vitro* and *in*

vivo previously [2, 3, 10, 87, 123, 160, 161]. As-drawn titanium (Ti)-6 wt.% aluminum (Al)-4 wt.% vanadium (V) alloy wires with the same diameter of 1 mm (Baoti Group Ltd, Baoji, Shaanxi, China) were used as a non-degradable control in the *in vitro* studies with BMSCs and MRSA, because Ti alloys represent the non-degradable metals that are currently used in major medical implants, such as bone fixation devices. We refer to this Ti alloy as T64. The 1-mm diameter wires of ZC21, Mg and T64 were cut into pins 15 mm long for characterization and *in vitro* studies. Non-culture-treated glass disks (Fisher Scientific, 0.13-0.17 mm thick, Catalog No. 12-545-80) were used as a reference for *in vitro* culture with BMSCs and MRSA because it is a widely accepted standard for cell culture. For *in vitro* bacterial culture, ZC21, ZSr41, Mg and T64 were cut into 5-mm long pins and non-culture-treated glass disks were used as reference. For *in vivo* study, the wires of ZC21, ZSr41 and Mg were cut into 2-mm long pins to fit into the femoral defect created in the animal model.

Before *in vitro* cell culture, *in vitro* bacterial culture, and *in vivo* implantation, the ZC21, ZSr41, Mg and T64 pins were ground and polished using SiC paper (Ted Pella, USA) of 600 grit, 800 grit and 1200 grit sequentially, and cleaned in 100% ethanol (200 proof; Koptec) with sonication (Symphony, VWR) for 5 min in between. Afterwards, all samples were degreased in acetone (Sigma Aldrich, USA) for 15 min, cleaned in 100% ethanol for 15 min with sonication, and dried in air at room temperature.

3.2.2. Surface characterization of ZC21 pins and controls

The surface appearance of ZC21, Mg and T64 pins before and after polishing was examined using optical microscopy (SE303R-P, Amscope). The microstructure of ZC21, Mg, T64 pins and glass references after polishing was also characterized using scanning electron microscopy (SEM; Nova NanoSEM 450, FEI Co.) under the high vacuum mode. Surface elemental composition and distribution were analyzed using energy dispersive X-ray

spectroscopy (EDS; Aztec, Oxford instruments, Abingdon, UK). An accelerating voltage of 15 kV was used to capture SEM images and perform EDS analyses. Glass references were sputter coated with Pt/Pd using a supper coater (Model 108, Cressington Scientific Instruments Ltd., Watford, UK) at 20 mA for 40 seconds of sputter time. To measure the grain size, ZC21 and Mg pins were mounted into epoxy (PACE Technologies, AZ, USA) and the surface along the length of pin was exposed for polishing. The samples were first ground with SiC papers up to 1200 grit, and fine polished using polycrystalline diamond paste (Physical Test Solutions, Culver City, CA, USA) from 6 μm to 0.25 μm. The etching solution was prepared by adding 10 mL acetic acid (Sigma Aldrich, USA), 4.2 g picric acid (Sigma Aldrich, USA), and 10 mL distilled water into 70 mL ethanol. The mounted Mg pins were dipped into the etching solution for about 2-8s, while ZC21 pins were dipped for 15-20s until plenty of bubbles were observed. After etching, the samples were cleaned with ethanol, dried in air quickly at room temperature, and examined using a 3D laser microscope (VK-X150, Keyence, USA). Additionally, X-ray diffraction (XRD; Empyrean, PANalytical, Westborough, MA, USA) was used to analyze the crystal structures and phases present in ZC21alloy and Mg pins. All XRD spectra were acquired using Cu K_{α} radiation (45 kV, 40 mA) at a step size of 0.006° and dwell time of 50 seconds using a PIXcel 1D detector (PANalytical). Phase identification was performed using HighScore software (PANalytical).

3.2.3. Mechanical testing of ZC21 pins and controls

The compressive strength of ZC21 pins and Mg pins with a cylindrical geometry and a size of 1 mm in diameter and 2 mm in length was measured using a mechanical testing system (5969, Instron, Norwood, MA). The samples were photographed before and after compression testing. The mechanical properties of Mg-Zn-Ca alloys have been reported previously [142, 144, 148, 162], and the results showed that Mg-Zn-Ca alloys exhibited higher Young's modulus and higher tensile strength than pure Mg. Specifically, as-cast Mg had Young's modulus of 41GPa

and tensile strength of 86.8 MPa [148, 162]. As-cast Mg-4Zn-0.5Ca showed tensile strength of 180 MPa [142] while the extruded Mg–4.0Zn–0.2Ca alloy exhibited tensile strength of 297 MPa and Young's modulus of 45 GPa [144]. Based on these previous reports, ZC21 is expected to have higher mechanical strength than pure Mg. However, different processing parameters and testing conditions could affect the results, even when the alloy composition is the same or similar. Thus, the ZC21 pins that had the same processing parameters and sample dimension as the *in vivo* implants in mice were still mechanically tested to confirm. Both tensile and compressive properties are important for clinical applications, but we performed the compression test to mimic the condition of *in vivo* implantation in mouse femoral model in this study. Specifically, for compression testing, a strain rate of 1 mm/min was applied on the samples. The stress-strain curves for each sample were plotted to determine the ultimate compressive strength of each sample accordingly. After compression testing, the fracture surfaces of ZC21 and Mg were examined using SEM.

3.2.4. Corrosion testing of ZC21 pins and controls using electrochemical method

The corrosion properties of ZC21 pins and the control pins of ZSr41 and Mg were tested in a revised stimulated body fluids (rSBF) at 37 °C, using the electrochemical method established previously [2, 160]. Specifically, ZC21, ZSr41 and Mg pins with a cylindrical geometry and a size of 1 mm in diameter and 15 mm in length had about 2 mm immersed in rSBF for testing. Potentiodynamic polarization (PDP) curves were recorded at a voltage scan from -0.5 V to -3.0 V with a scanning rate of 10 mV/s using a potentiostat/galvanostat (Model 273A, Princeton Applied Research). The corrosion current I_{corr} and the corrosion potential E_{corr} were calculated by extrapolating the tangent line of the anodic and cathodic half of the curves according to the Tafel method in ASTM G102-89 standard. The corrosion current density J_{corr} was calculated by normalizing I_{corr} with the exposed surface area of each sample.

3.2.5. *In vitro* degradation and cytocompatibility of ZC21 pins and controls in the BMSC/DMEM culture system

3.2.5.1. Preparation of BMSC culture

Following the protocol approved by the Institutional Animal Care and Use Committee (IACUC) at the University of California at Riverside (UCR), rat BMSCs were harvested and cultured according to previously published procedures [1, 163]. Briefly, the distal and proximal ends of the femoral and tibial bones were dissected, and the bone marrow was flushed out of the bone cavity and collected using DMEM (Sigma Aldrich, St Louis, MO, USA) supplemented with 10% fetal bovine serum (FBS; HyClone, Logan, UT, USA) and 1% penicillin/streptomycin (P/S; Invitrogen, Grand Island, NY, USA). Hereafter, DMEM + 10%FBS + 1% P/S is referred to as DMEM. The collected cells were then filtered through a 70-μm nylon strainer (Fisher Scientific, NH, USA) to remove cell aggregates and tissue debris. The filtered BMSCs were cultured in DMEM under standard cell culture conditions (i.e., 37 ℃, 5%/95% CO_2/air, humidified, sterile environment) to 90–95% confluency. Subsequently, BMSCs were detached using Trypsin (Fisher Scientific) and cultured up to the second passage (P2) for the *in vitro* cell studies with ZC21 pins and controls.

3.2.5.2. BMSC culture with ZC21 pins and controls

The cleaned and dried ZC21, Mg and T64 samples were first weighed individually and then disinfected under ultraviolet (UV) radiation for 4 h before they were used in the cell studies. The glass references were disinfected under UV radiation for 2 h on each side. The wells of standard 12-well tissue culture treated plates were rinsed with 2 mL PBS and 2 mL DMEM to calibrate the osmotic pressure under sterile conditions. For the direct exposure culture method, BMSCs (P2) were first seeded into each well at a density of 20,000 cells/cm^2 and incubated in 3 mL of DMEM under standard cell culture conditions for 24 h. The disinfected samples were then

placed directly on top of the cell layer without changing media and cultured for another 24 h. For the direct culture method, the samples and references were first placed in the culture wells, and BMSCs (P2) were then seeded directly onto the surfaces of the samples at a density of 20,000 cells/cm^2 and incubated in 3 mL of DMEM under standard cell culture conditions for 24 h. A positive control, designated as the ‘‘cells’’ group, consisted of BMSCs cultured with only DMEM in the wells, i.e. without any samples. DMEM alone without cells and samples was also included as a blank reference and designated as the ‘‘media’’ group. All samples and references were run in triplicate.

3.2.5.3. Surface characterization of ZC21 pins and controls after in vitro cell culture

After the BMSC culture, the surfaces of ZC21, Mg and T64 pins were examined again using optical microscopy. The surface microstructure and elemental composition of ZC21, Mg, T64, and glass were further characterized using SEM and EDS at an accelerating voltage of 15 kV under high vacuum mode. All samples were sputter coated with Pt/Pd at 20 mA for 40 seconds of sputter time before SEM imaging. XRD was used to determine the phases present in ZC21 alloy and Mg control after direct exposure culture and direct culture. The chemical bonding of the degradation products on the surfaces of ZC21 alloy and Mg control after culture was determined using Fourier transform infrared spectroscopy (FTIR, Thermo Fisher Scientific Nicolet iS10).

3.2.5.4. Characterization of BMSC adhesion and morphology

After the prescribed cell culture, BMSCs attached on the samples and plates were fixed with 4% formaldehyde (10% neutral buffered formalin; VWR, Radnor, PA, USA) for 20 min. The fixed BMSCs were stained with Alexa Flour® 488-phalloidin (A12379, Life technologies) for F-actin for 20 min, and 4’,6-diamidino-2-phenylindole dilactate (DAPI, Invitrogen) for nuclei for 5 min. BMSCs attached on each sample (i.e., direct contact) and on the plate around each

sample (i.e., indirect contact) were imaged using a fluorescence microscope (Eclipse Ti and NIS software, Nikon, Melville, NY, USA). DAPI-stained nuclei were counted to determine cell adhesion density per unit area. At least five fluorescence images of BMSCs under direct contact conditions and nine fluorescence images of BMSCs under indirect contact conditions were used for cell counting and statistical analyses of the data.

3.2.5.5. In vitro degradation of ZC21 pins in the BMSC culture

After the prescribed cell culture, each sample was dried and weighed again. The initial and final mass of each sample were used to calculate the mass ratio, that is, final/initial mass. The pH of the post-culture media was measured using a pre-calibrated pH meter (Symphony™, Model SB70P, VWR) immediately after collection of the media. The concentrations of Mg^{2+}, Zn^{2+}, and Ca^{2+} ions in the post-culture media were measured using inductive coupled plasma - optical emission spectrometry (ICP-OES, Optima 8000, PerkinElmer). Before ICP-OES, the media of all groups were diluted in deionized (DI) water to minimize the matrix effects. For the measurements of Mg^{2+} and Ca^{2+} ions, the media were diluted in deionized water at a ratio of 1:100. For the measurement of Zn^{2+} ion, the media were diluted in deionized water at a ratio of 1:10. The ICP-OES was calibrated using Mg^{2+}, Zn^{2+} and Ca^{2+} standard solutions that were diluted to the ranges of 0.5~5.0 mg/L, 0.1~1.0 mg/L and 0.1~1.0 mg/L, respectively.

The degradation rates of ZC21 pins and Mg control pins were calculated as the daily release rate of Mg^{2+} ions into the culture media. According to the equation of the degradation reaction (Equation 1), Mg^{2+} ion release is a direct indicator of the degradation process.

$$Mg(\mathrm{s}) + 2H_2O(l) \rightarrow Mg^{2+} + 2OH^- + H_2(g) \quad (1)$$

The daily degradation rates of ZC21 and Mg into culture media were calculated following Equation 2.

$$R = \frac{(C_{Mg} - C_0) \times V}{A \times t} \quad (2)$$

In Equation 2, R represents the daily degradation rates, C_{Mg} represents the Mg^{2+} ion concentration in the media measured after 24-h culture with a sample, C_0 represents the mean Mg^{2+} ion concentration in the DMEM blank reference measured after 24h culture, V represents the volume of culture media in each culture well (i.e., 3mL), A represents the surface area of the sample, and t represents the culture time, i.e., t=1 day for the 24h period. C_0 is the baseline of Mg^{2+} ion concentration in the DMEM media for each group, and thus it should be subtracted from the measured total Mg^{2+} ion concentration in the post-culture media to obtain the actual concentration of Mg^{2+} ions released from degradation of Mg-based samples. The daily release rates of Mg^{2+} ions into the culture media could be used for direct comparison of the degradation rates of different sample groups, e.g., ZC21 pins and Mg controls. The width and area of corrosion cracks on the surfaces of ZC21 and Mg after direct exposure culture and direct culture were determined based on their corresponding SEM images, using quantitative image analysis tools in ImageJ. The crack width was defined as the gap distance between the two edges of the crack. The crack area ratio was defined as the ratio of crack area over the whole SEM image area. Specifically, the "straight line" tool was used to draw lines for determining crack width, while the "freehand selections" tool was used to outline the crack area and to determine the crack area ratio. The crack width and crack area ratio were measured in three images for each group, and five measurements were performed in each SEM image for statistical analyses of the data.

3.2.6. Bacterial culture with ZC21 alloy, ZSr41 alloy, and Mg pins *in vitro*

3.2.6.1. Preparation of bacterial culture

The frozen stock of methicillin-resistant *Staphylococcus aureus* (MRSA) was stored at -80℃. A sterile loop was used to transfer a portion of the frozen stock to the Tryptic Soy Broth (TSB; Fluka Analytical, Sigma-Aldrich). The frozen MRSA was retrieved and cultured in Tryptic Soy Broth (TSB; Fluka Analytical, Sigma-Aldrich) overnight using a shaker incubator (Incu-

shaker Mini, Benchmark Scientific) at 37℃ and 250 rpm for 16 h. A 10 μL of the bacteria stock was added into 5 mL of fresh TSB and incubated for another 4-6 hours at 37℃ and 250 rpm. The as-grown bacteria was then washed 3 times with revised simulated body fluid (rSBF) to remove any residual TSB and resuspended in rSBF supplemented with 10% FBS. The concentrations of MRSA were first determined using a hemocytometer (Hausser Bright-Line 3200, Hausser Scientific) and then the MRSA suspension was diluted to a concentration of 7.5×10^5 cells/mL in rSBF supplemented with 10% fetal bovine serum (FBS). The MRSA concentration of 7.5×10^5 cells/mL was used to match the reported concentration that causes orthopedic infections clinically [164]. After dilution to 7.5×10^5 cells/mL, 0.75 mL MRSA suspension was added to each well of a 48-well non-tissue culture treated polystyrene plate (Corning, Falcon 351143) that contained the samples and controls, and incubated for 24 h in the shaker incubator at 37℃ and 120 rpm. The initial seeding density was confirmed by plating the diluted MRSA stock onto the agar plates and counting the colony forming units (CFUs).

3.2.6.2. Characterization of MRSA concentration, adhesion and morphology

After 24-h bacterial culture, the post-culture broth was collected and the MRSA concentration in the collected broth was measured by counting the colony forming units (CFU) plated on the agar plates. For this purpose, each collected post-culture suspension was diluted using a suitable dilution factor that can lead to a reasonably countable number of CFUs. For agar plating, a 100 μL of diluted suspension was individually pipetted onto the agar plate, and evenly spread using a glass spreader. The agar plates were then inverted and incubated for 16-18 h.

To determine the density of bacteria adhered on the samples, two samples from each group were placed individually in microcentrifuge tubes with 2 mL rSBF. The microcentrifuge tubes were then sonicated in a sonication bath for 10 minutes, and at each 5 minutes they were vortexed for 5 seconds. After that, the adhered bacteria were detached from the sample surfaces

and collected in the rSBF. The MRSA concentration in the collected rSBF was measured by counting the colony forming units (CFU) plated on the agar plates following the same method of agar plating and CFU counting as described above.

To determine the adhesion and morphology of bacteria on the sample surfaces, one sample from each groups was analyzed using SEM imaging. The bacteria on the surface were first fixed with 10% glutaraldehyde (Sigma Aldrich) for 1 h and then rinsed 3 times with a Tris-buffered saline (Sigma Aldrich). The samples were then dehydrated using 25%, 75% and 100% ethanol for 30 mins each and air dried at room temperature for 24 h. The dried samples were sputter-coated with Pt/Pd for 60 s at 20 mA, prior to the SEM imaging.

3.2.6.3. In vitro degradation of ZC21 pins in the MRSA culture

The pH of the post-culture rSBF with 10% FBS was measured using a pre-calibrated pH meter (Symphony SB70P, VWR). The post-culture rSBF with 10% FBS was then diluted with DI water to 1:100 to analyze the Mg^{2+} and Ca^{2+} ion concentrations, and diluted with DI water to 1:10 to analyze the Sr^{2+} ion concentration in the media cultured with ZSr41 using ICP-OES similarly as described above in 2.4.5. All the groups were run in triplicates. Finally, the degradation rates of ZC21 pins, ZSr41 pins and Mg control pins were calculated as described above in 2.4.5.

3.2.7. *In vivo* degradation of ZC21 alloy, ZSr41 alloy, and Mg pins and bone regeneration in mouse femoral defects

3.2.7.1. Animal model and surgical procedures

Nine 10-week-old male mice were used in the present study and randomly assigned to three groups (n = 3 per group). The Institutional Animal Care & Use Committee (IACUC) at the University of Southern California approved the experimental protocol (#9320). Before initiation of anesthesia for each animal, buprenorphine (0.5mg/kg of animal weight; Buprenorphine SR-LAB 1mg/mL; ZooPharm, Windsor, CO, USA) was administered subcutaneously as a sedative

and preventive analgesic. The analgesic effect of this medication lasts at least 72 hours throughout surgery and post-operative recovery. Anesthesia was induced and maintained using ~2% isoflurane (Fluriso, NDC 13985-046, VETone, ID, USA) and 0.3 L/min of oxygen flow.

Anaesthetized mice were positioned on the operating table in a prone position with the left leg facing downwards. The operation site was aseptically prepared. A posterior-lateral approach was used to expose the lateral surface of the femur by separating the muscles. The periosteum of the femur was incised, and then the femur was exposed using a retractor. Following pre-drilling using a drill with a diameter of 0.31 mm on the posterior lateral side of the exposed femur, four stainless steel screws were used to stabilize the 6-hole plastic plate (RISystem AG, Davos, Switzerland) with a drill & saw guide (jig). Two Gigli saws (0.22mm; RISystem) were then inserted, one in each of the two slots in the jig, and a 2-mm long mid-diaphyseal femoral ostectomy was subsequently performed. The jig was then removed and the two end screws locked the plate in place. The surgical field was copiously lavaged with sterile isotonic saline. The defect was filled with the filling materials of interest, i.e., pins of ZC21 alloy, ZSr41 alloy, and pure Mg control. Sham designates the reference group with femoral defect only, i.e., no pin implant. In all animals, the fascia and subcutaneous planes were closed with a simple continuous suture pattern using 5-0 Vicryl rapid sutures. Skin closure was accomplished using a simple interrupted suture pattern using 4-0 Prolene.

3.2.7.2. Monitoring the healing of femoral defects and the degradation of pins

X-ray radiography (In-vivo Xtreme X-ray; Bruker) was used to monitor the degradation of pin implants and healing of femoral defects *in situ* at 4 weeks, 8 weeks and 12 weeks after surgery. The size of the gap created between the two cut ends of the femur was measured on the radiographs at each time point using ImageJ.

3.2.7.3. Characterization of the pin implants after 12 weeks of implantation

After 12 weeks of implantation in the femurs of mice, all tissues and samples were fixed and stored in 4% paraformaldehyde(PFA). The surfaces of ZC21, ZSr41 and Mg pins were examined using optical microscopy before and after 12weeks of *in vivo* implantation. Mg pins degraded completely after 12 weeks. All samples were weighed before and after 12 weeks of implantation. The initial and final masses of each sample were used to calculate the mass ratio, that is, final/initial mass.

The daily degradation rates of ZC21 and ZSr41were calculated following Equation 3.

$$R = \frac{(M - M_0)}{A \times t} \quad (3)$$

In Equation 3, R represents the daily degradation rate, M represents the mass of a sample after 12 weeks of implantation, M_0 represents the mass of a sample before implantation, A represents the surface area of a sample, t represents the implantation time, i.e., t=84 days for the 12-week period. SEM images were taken on the surface region of ZC21 and ZSr41 after the loose deposition layer was removed, to identify crack width and area using ImageJ.

Surface topography and elemental composition of the surfaces of ZC21 and ZSr41 pins after implantation for 12 weeks were characterized using SEM and EDS, respectively. Additionally, elemental distribution maps on the surfaces of dissected pins were obtained for Mg, carbon (C), oxygen(O), phosphorus (P), Ca, sodium (Na) and potassium (K) (K_α lines). XRD was used to determine the phases present on the surfaces of ZC21 and ZSr41 pins. The chemical bonding of the degradation products on the surfaces of ZC21 and ZSr41 pins were examined using FTIR. Experimental settings for SEM, EDS, XRD and FTIR were the same as described above in Section 2.3.

3.2.8. Statistical analyses

All numerical data used in this study were obtained from experiments run in triplicate. The numerical data on the adhesion density of BMSCs under direct contact and under indirect

contact conditions, sample mass ratio, pH in the culture media, ion concentrations in the culture media, daily release rates of Mg^{2+} ions, and width and area of corrosion cracks on the surfaces of ZC21 and Mg pins were examined using two-way analysis of variance (ANOVA) followed by post-hoc test. The statistical analysis was performed using GraphPad Prism 7 software. Statistically significant differences were considered to be $p<0.05$.

3.3 Results

3.3.1. Microstructure, elemental composition, mechanical properties and corrosion properties of ZC21 pins and controls

Figure 3-1a-b are the optical images of metallographic samples of ZC21 and Mg pins. Clearly, the microstructures in Figure 3-1a-b confirmed that the grain size of ZC21 was much smaller than that of Mg; that is, the addition of Zn and Ca into Mg substrate could refine the grain size. Figure 3-1c-g shows the SEM images and surface elemental compositions (wt. %) of ZC21 alloy pin, Mg pin, T64 pin, and glass reference. In Figure 3-1c, at low magnification (500x), ZC21 and Mg showed random white precipitates on the surface that could be traces of oxides or hydroxides, and T64 showed typical alloy microstructure with secondary phase on the surface. Polishing traces were barely visible in the low-magnification SEM images. However, at high magnification (5000x), polishing traces were visible on the surfaces of ZC21, Mg and T64 samples. The surface of the glass reference appeared smooth without any visible features at both low and high magnification. Figure 1d shows the elemental composition on the surface of ZC21 acquired by EDS area and point analyses. The EDS analysis of the whole image area of ZC21 at low magnification (500x) showed 95.6 wt.% Mg, 2.0 wt.% Zn and 0.4wt.% Ca, which confirmed the nominal composition of ZC21 alloy. The EDS point analyses at high magnification (5000x) showed consistent results, i.e., similar to the EDS area analysis on ZC21 alloy. Specifically, for

ZC21, Point 1 showed 94.5 wt.% Mg, 1.8 wt.% Zn and 0.4 wt.% Ca, while Point 2 showed 96.0 wt.% Mg, 2.0 wt.% Zn and 0.3 wt.% Ca. Figure 3-1e shows the EDS area and point analyses of Mg. Specifically, the EDS results of Mg at 500x and at Points 3 and 4 at 5000x showed 94.3 wt.% Mg, 94.6 wt.% Mg and 93.2 wt.% Mg, respectively; small amounts of carbon (C) and oxygen (O) were also detected. In Figure 3-1f, the EDS results of T64 at 500x and at Points 5 and 6 at 5000x all showed similar elemental composition. Specifically, T64 area analysis showed 88.6 wt.% titanium (Ti), 5.5 wt.% aluminum (Al) and 3.4 wt.% vanadium (V); Point 5 showed 88.6 wt.% Ti, 6.0 wt.% Al and 2.5 wt.% V; Point 6 showed 88.8 wt.% Ti, 6.0 wt.% Al and 3.4 wt.% V. As for glass reference, 41.1 wt.% silicon (Si), 15.1 wt.% sodium/potassium (Na/K), 1.6 wt.% carbon (C) and 42.3 wt.% oxygen (O) were detected in EDS area analysis at low magnification, as shown in Figure 3-1g.

The results of compression testing for ZC21 and Mg pins are shown in Figure 3-2. The samples were compressed to the point where they became fractured, as shown in Figure 3-2a-b. The representative stress-strain curves for ZC21 and Mg pins are plotted in Figure 3-2c. The ultimate compressive strength in Figure 3-2d and the compressive modulus in Figure 3-2e were determined based on all the stress-strain curves. ZC21 showed a statistically higher compressive strength and compressive modulus than Mg because of the addition of Zn and Ca as alloying elements. Specifically, the compressive strengths of ZC21 and Mg were 321.1±13.6 MPa and 262.7±8.3 MPa, respectively. The compressive modulus of ZC21 and Mg were 4.13±0.15 GPa and 3.10±0.10 GPa, respectively. Not surprisingly, the deformation of ZC21 and Mg pins under mechanical stress was observed in Figure 3-2f-g. The micro-cracks on the surface of fractured ZC21 sample appeared smaller than that of Mg.

Figure 3-3a shows the representative potentiodynamic polarization (PDP) curves of ZC21 pins and the control pins of ZSr41 and pure Mg. Figure 3-3b shows the corrosion potential (E_{corr})

and corrosion current density (J_{corr}) of ZC21 pins and the control pins of ZSr41 and pure Mg, which were extrapolated based on the Tafel method. ZC21 and Mg exhibited a statistically significant more negative E_{corr} than ZSr41. Mg showed statistically significant higher J_{corr} than ZC21 and ZSr41. Overall, the results indicated that Mg had the least corrosion resistance.

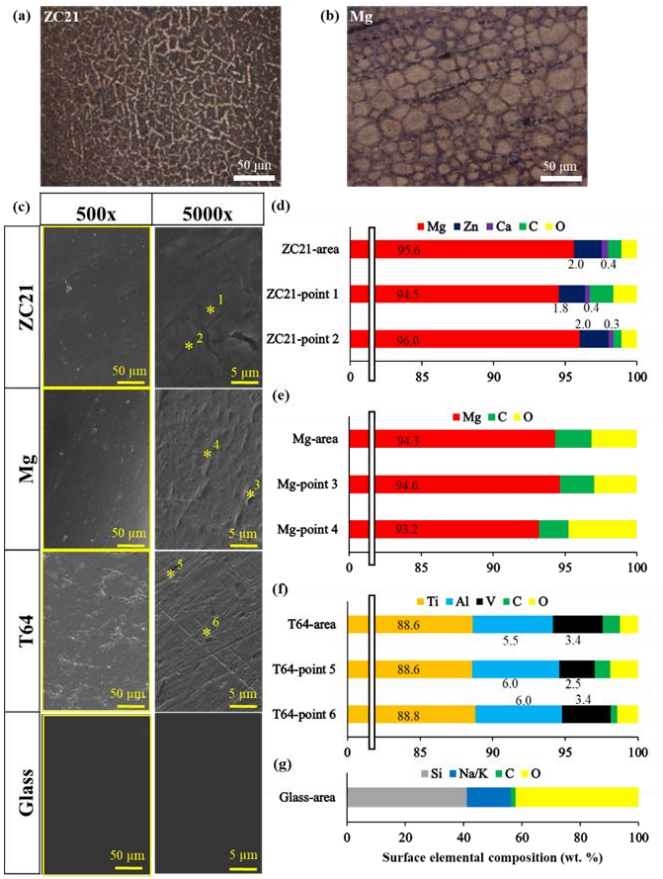

Figure 3-1. Optical images for metallographic microstructures of (a) ZC21 and (b) Mg. (c-g) SEM images and EDS surface elemental composition (wt. %) of ZC21, Mg, T64 and glass. (c) SEM images of the samples and controls at the 500x and 5000x original magnifications after polishing; (d) EDS area analysis (wt. %) of ZC21 at 500x original magnification and EDS point analysis of point 1 and 2 in ZC21; (e) EDS area analysis (wt. %) of Mg at 500x original magnification and EDS point analysis of point 3 and 4 in Mg; (f) EDS area analysis (wt. %) of T64 at 500x original magnification and EDS point analysis of point 5 and 6 in T64; (g) EDS area analysis (wt. %) of glass at 500x original magnification.

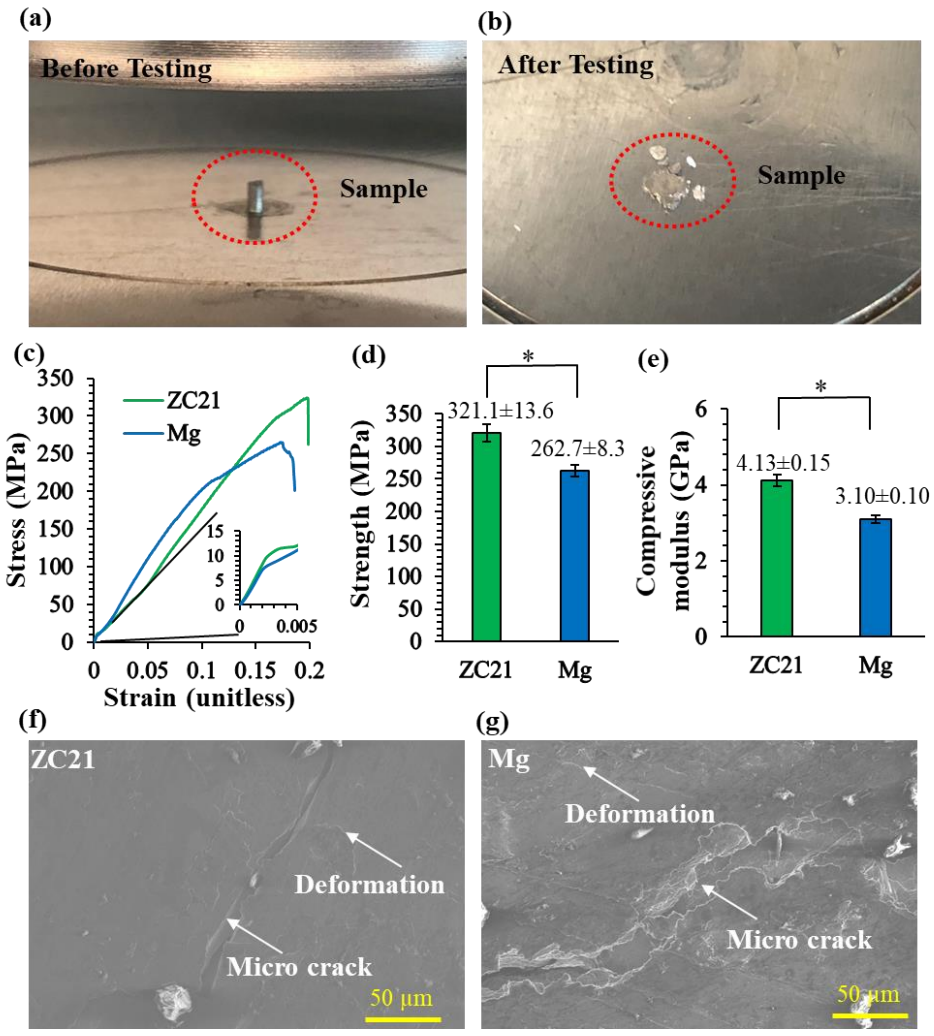

Figure 3-2. The results of compression testing for ZC21 and Mg pins. (a, b) Representative photographs of a sample (a) before and (b) after compression testing. (c) Representative stress-strain curves of ZC21 and Mg pins. (d) The average ultimate compression strengths and (e) compressive moduli of ZC21 and Mg pins. (f, g) SEM images of the fracture surfaces of (f) ZC21 and (g) Mg at 500x original magnification after compression testing.

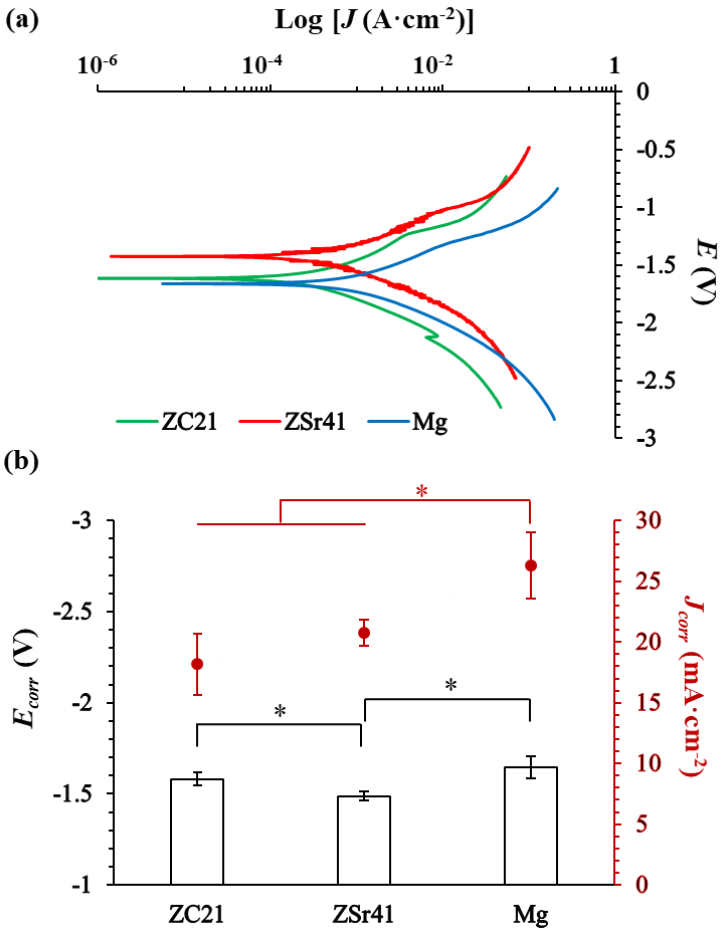

Figure 3-3. Corrosion properties of the ZC21 pins and the control pins of ZSr41 and Mg from electrochemical testing in rSBF. (a) Representative potentiodynamic polarization (PDP) curves for ZC21, ZSr41 and Mg pins. (b) Corrosion potential and corrosion current density extrapolated from the PDP curves according to the Tafel method. The bar graphs with their axis on the left show the corrosion potential (E_{corr}); and the red square symbols with their axis on the right show the corrosion current density (J_{corr}). Values are mean ± standard deviation (n=3). *p<0.05.

3.3.2. BMSC responses and degradation of ZC21 pins and controls *in vitro*

3.3.2.1. Surface analysis before and after in vitro BMSC culture

Figure 3-4 shows optical micrographs of ZC21, Mg and T64 pins before polishing, after polishing, after 24-h direct exposure culture, and after 24-h direct culture. Before polishing, the

surfaces of all metallic samples showed non-homogeneous oxidation with dark coloration. After polishing, the oxide layers were removed and the surface became shiny. After direct exposure culture and direct culture, white precipitates appeared on the surfaces of ZC21 and Mg, while the surface of T64 showed no visible change.

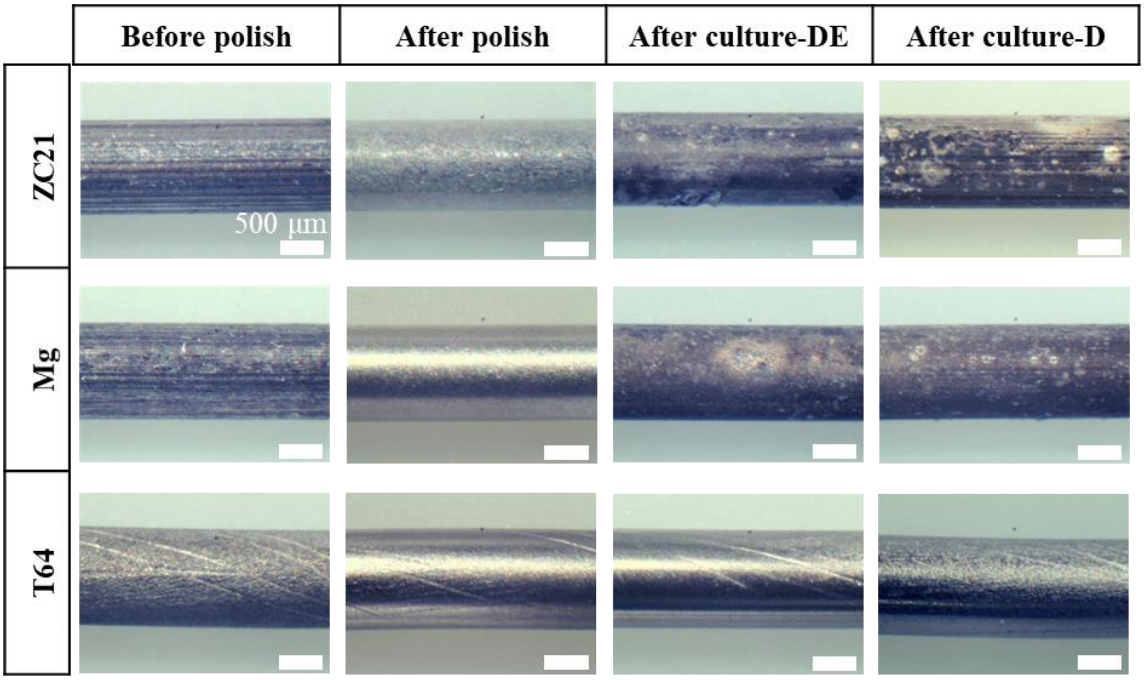

Figure 3-4. Optical images of ZC21, Mg and T64 before polishing, after polishing, after 24-h direct exposure culture (DE), and after 24-h direct culture (D) with BMSCs in DMEM. All samples were sequentially polished using the SiC papers of 600, 800, and 1200 grits. Scale bar = 500 μm for all images.

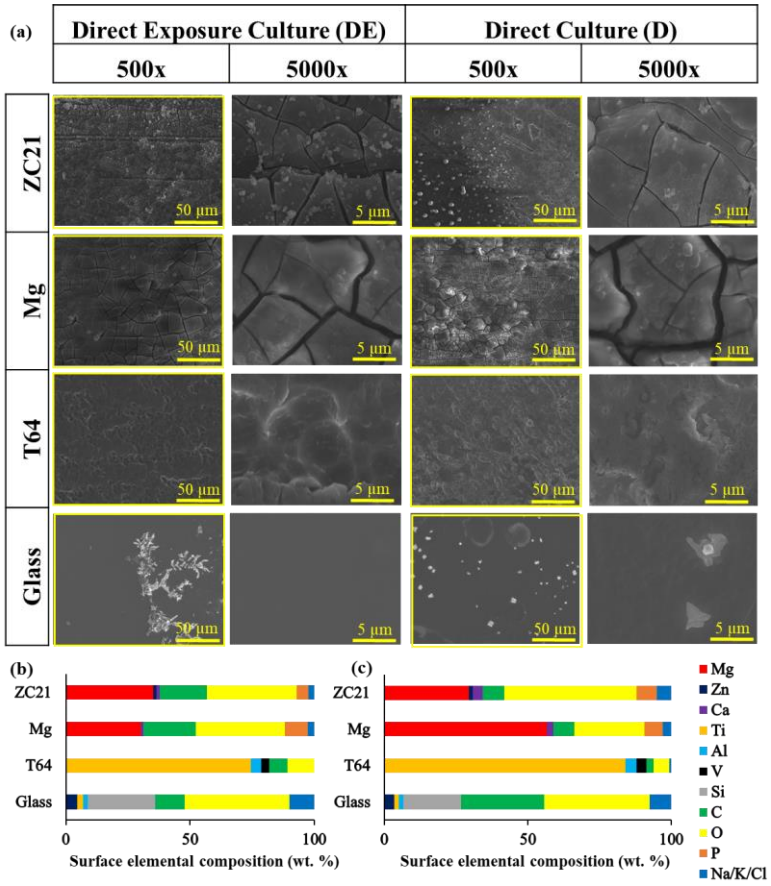

Figure 3-5. SEM images and EDS analysis of ZC21, Mg, T64 and glass after 24-h direct exposure culture and direct culture with BMSCs in DMEM. (a) SEM images of all samples at 500x and 5000x original magnification after culture; (b) Surface elemental composition (wt. %) of all samples at 500x original magnification after 24-h direct exposure culture; (c) Surface elemental composition (wt. %) of all samples at 500x original magnification after 24-h direct culture.

Figure 3-5 shows the SEM images and surface elemental compositions (wt. %) of ZC21, Mg, T64 and glass after 24-h direct exposure culture and 24-h direct culture. In Figure 3-5a, more white precipitates were observed on ZC21 at the low magnification of 500x than on Mg after both culture methods. At the high magnification of 5000x, localized corrosion and cracks became more visible on the surfaces of ZC21 and Mg when compared with the respective low-magnification SEM images. After direct culture, cracks on the ZC21 surface were slightly smaller than on the sample cultured using the direct exposure method. As for Mg, localized corrosion was

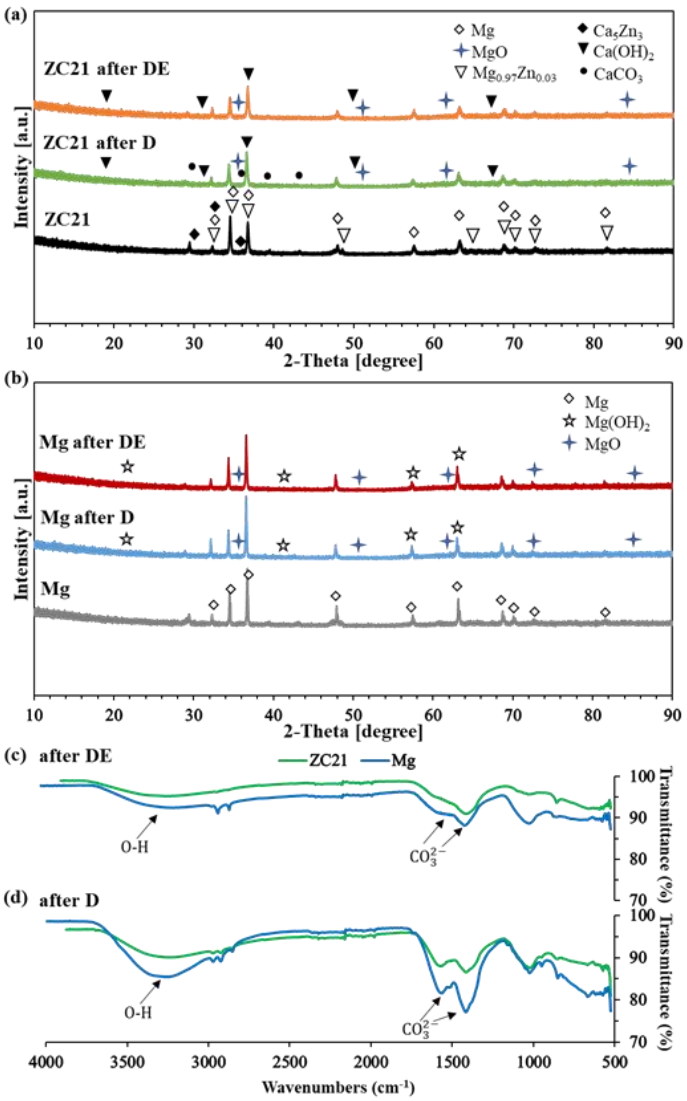

Figure 3-6. XRD and FTIR spectra of ZC21 and Mg. (a) XRD spectra of ZC21 after 24-h direct exposure culture (DE), after 24-h direct culture (D), and before cell culture. Phases were identified based on Mg (ICSD pattern 01-089-7195), MgO (ICSD pattern 01-070-9183), $Mg_{0.97}Zn_{0.03}$ (ICSD pattern 01-071-9628), Ca_5Zn_3(ICSD pattern 01-073-8016), $Ca(OH)_2$(ICSD pattern 01-073-8394) and $CaCO_3$ (ICSD pattern 01-085-1108). (b) XRD spectra of Mg after 24-h DE, after 24-h D, and before cell culture. Phases were identified based on Mg (ICSD pattern 01-089-7195), MgO (ICSD pattern 01-070-9183) and $Mg(OH)_2$(ICSD pattern 01-078-3960). (c) FTIR spectra of ZC21 and Mg after 24-h DE. (d) FTIR spectra of ZC21 and Mg after 24-h D.

more severe and cracks on the surface were significantly larger than on ZC21 in both culture methods. T64 showed the same surface morphology as before culture at the low magnification of 500x for both culture methods; at high magnification of the 5000x, some deposition on the T64

surface became visible, possibly from the cell culture. On the glass reference, salt deposition appeared on the surface after both culture methods. Figure 3-5b shows the surface elemental composition of all samples at low magnification of 500x after 24-h direct exposure culture. ZC21 showed a significant decrease in Mg (35.2 wt.%) and Zn (1.3 wt.%) content because of the degradation layers formed on the surface. However, more Ca (1.3 wt.%) was detected, which indicated that the degradation layers contain Ca deposited from the culture. Both C (18.9 wt.%) and O (36.2 wt.%) increased significantly, and new salt elements, including phosphorus (P), Na, K and chlorine (Cl), were also detected. The Mg sample showed a decrease of Mg (30.2 wt.%) and an increase of C (21.1 wt.%) and O (35.9 wt.%). Ca (1.0 wt.%), P (9.2 wt.%) and Na/K/Cl (2.5 wt.%) were new salt elements detected on the surface of Mg. As for T64, not surprisingly, less Ti (74.4 wt.%), Al (4.3 wt.%) and V (3.3 wt.%) but more C (7.3 wt.%) and O (10.7 wt.%) were detected. Glass had 9.9 wt.%Na/K/Cl after culture. When comparing the EDS results after direct exposure culture (Figure 3-5b) versus direct culture (Figure 3-5c), each sample showed a similar increasing or decreasing trend to the EDS results before culture; however, the exact elemental compositions of each sample differed under the two different culture methods.

Figure 3-6 shows XRD and FTIR spectra of ZC21 and Mg before and after cell culture. Specifically, in Figure 3-6a, XRD spectra of ZC21 before culture, after 24-h direct exposure culture, and after 24-h direct culture showed the presence of different phases before and after culture. The relevant phases were identified based on Mg (ICSD pattern 01-089-7195), MgO (ICSD pattern 01-070-9183), $Mg_{0.97}Zn_{0.03}$ (ICSD pattern 01-071-9628), Ca_5Zn_3(ICSD pattern 01-073-8016), $Ca(OH)_2$ (ICSD pattern 01-073-8394), and $CaCO_3$ (ICSD pattern 01-085-1108). The XRD pattern of ZC21 before culture indicated an α-Mg phase accompanied by $Mg_{0.97}Zn_{0.03}$and Ca_5Zn_3 phases. After direct exposure culture, MgO and $Ca(OH)_2$ phases were detected. After direct culture, MgO, $Ca(OH)_2$ and $CaCO_3$ phases were detected. Figure 6b shows XRD spectra of

Mg before culture, after 24-h direct exposure culture and after 24-h direct culture. The relevant phases were identified based on Mg (ICSD pattern 01-089-7195), MgO (ICSD pattern 01-070-9183) and $Mg(OH)_2$ (ICSD pattern 01-078-3960). After both culture methods, MgO and $Mg(OH)_2$ were detected on the Mg control samples. In the FTIR spectra, O-H and CO_3^{2-} functional groups were identified for ZC21 and Mg control samples after both culture methods, as shown in Figures 3-6c and 3-6d, respectively.

3.3.2.2. Cell morphology and adhesion after culture with ZC21 pins and controls

Figure 3-7 shows fluorescence images of BMSCs adhered on the sample surface (direct contact) and on the culture plates surrounding the respective samples (indirect contact) after 24-h direct exposure culture and 24-h direct culture. Under the direct contact conditions in the direct exposure culture, ZC21 had more cells attached to the surface than T64 or glass, but the surface of Mg had no cells attached. Under the direct contact conditions in the direct culture, BMSCs attached to the ZC21 surface but no cells attached to the Mg surface. T64 and glass had more cells attached on their surfaces under direct contact conditions in the direct culture than did their counterparts in the direct exposure culture. Under the indirect contact conditions, the ZC21, Mg and T64 groups showed greater cell adhesion than under the direct contact conditions in the same culture methods. All groups showed more BMSCs attached on the plate surrounding each sample in direct exposure culture than in direct culture, most likely because the BMSCs in the direct exposure culture were pre-cultured for 24 h.

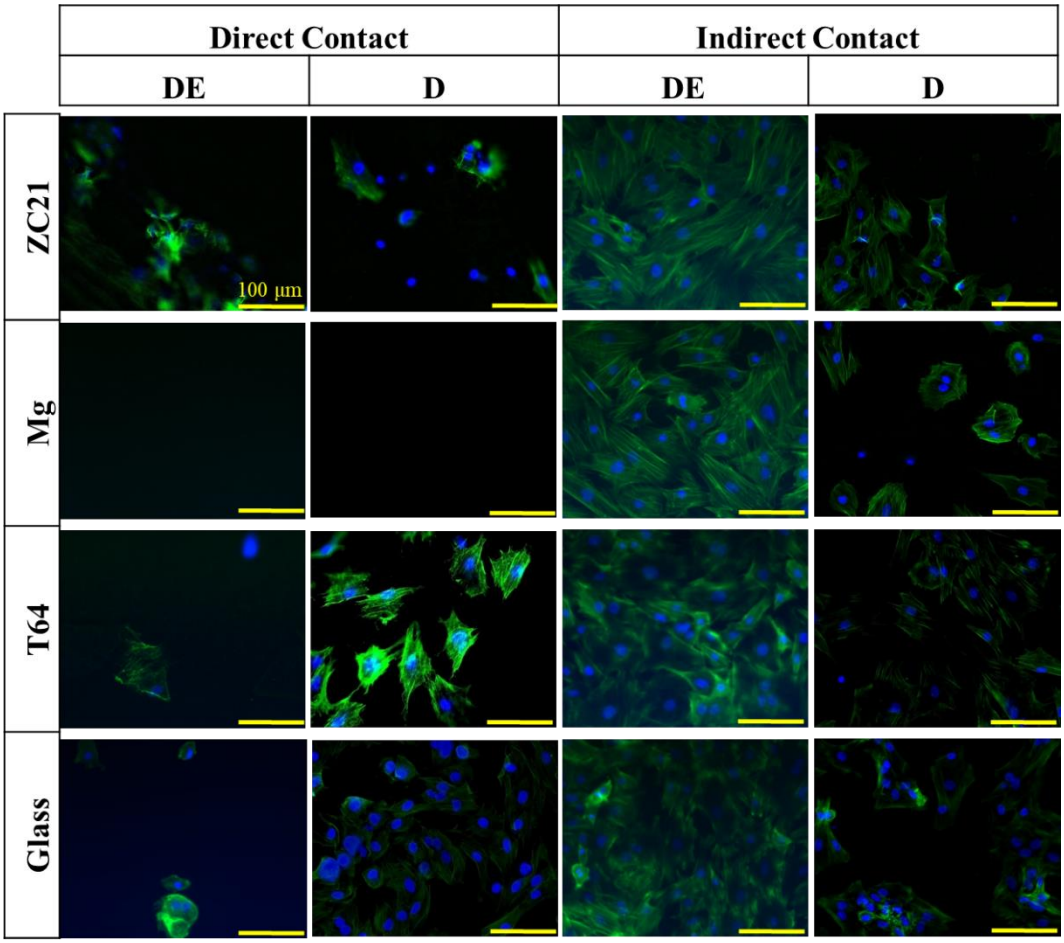

Figure 3-7. Representative fluorescence images of BMSCs adhered on the sample surface (direct contact) and on the culture plate surrounding each corresponding sample (indirect contact) after 24-h direct exposure culture and 24-h direct culture with each group of materials of interest. Scale bar = 100 μm for all images.

BMSC adhesion density was quantified based on the fluorescence images after 24-h direct exposure culture and 24-h direct culture, as shown in Figure 3-8. In direct exposure culture in Figure 3-8a, ZC21 showed statistically higher cell density in direct contact conditions than Mg, T64 and glass. In direct culture, ZC21, Mg and T64 showed statistically lower cell density under direct contact conditions than glass. Under direct contact conditions, the cell density on ZC21 samples was statistically greater than on Mg controls in both culture methods. The Mg control group showed a statistically lower cell density than T64 and glass under direct contact conditions

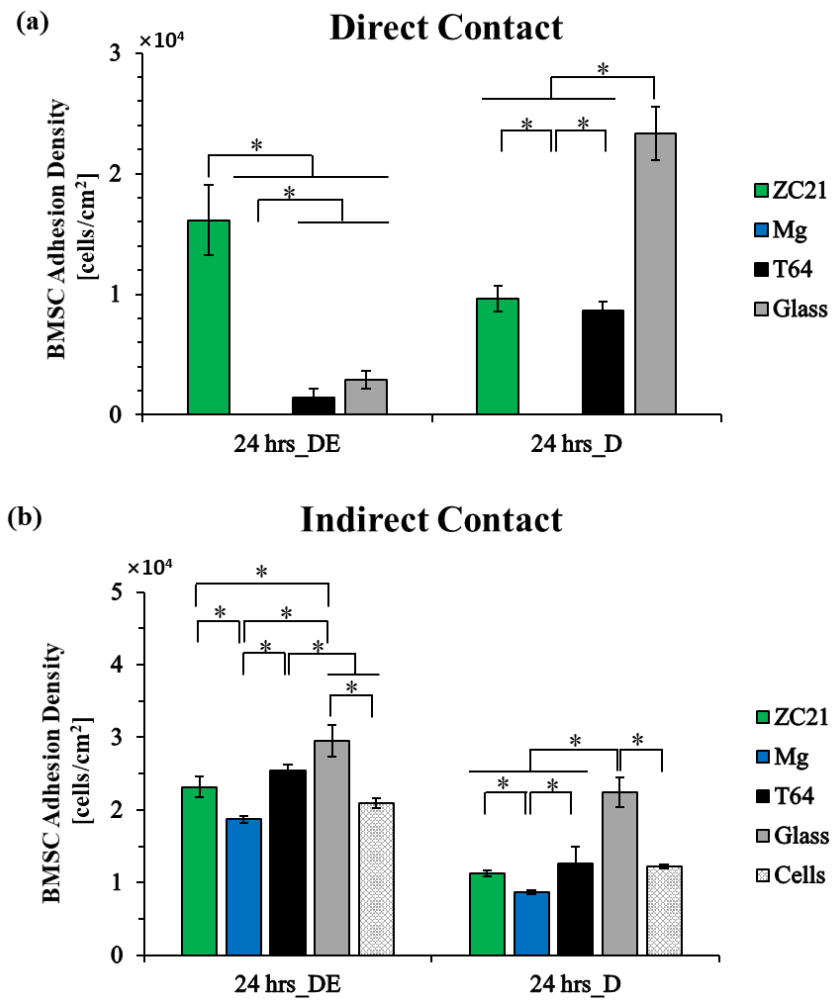

Figure 3-8. BMSC adhesion density after 24-h direct exposure culture and 24-h direct culture on ZC21, pure Mg control, T64 control, glass reference and cell-only control on (a) the sample surface (direct contact), and (b) the culture plate surrounding each corresponding sample (indirect contact). Initial cell seeding density was 2×10^4 cells/cm^2. Values are mean ± standard error of the means, n = 3; *p< 0.05.

in both culture methods. Figure 3-8b shows the quantified cell density under indirect contact conditions in each group, and importantly, ZC21 showed statistically higher cell density than Mg controls, but no statistical difference in cell density when compared with T64 and cell-only groups in both cell culture methods.

3.3.2.3. In vitro degradation of ZC21 and Mg pins in the BMSC/DMEM culture systems

Changes in sample mass, pH of post-culture media, and ion concentrations in the post-culture media are the key indicators of degradation of Mg-based samples. Figure 3-9 shows the mass ratio of the samples (that is, final mass/initial mass) and pH values of the media collected

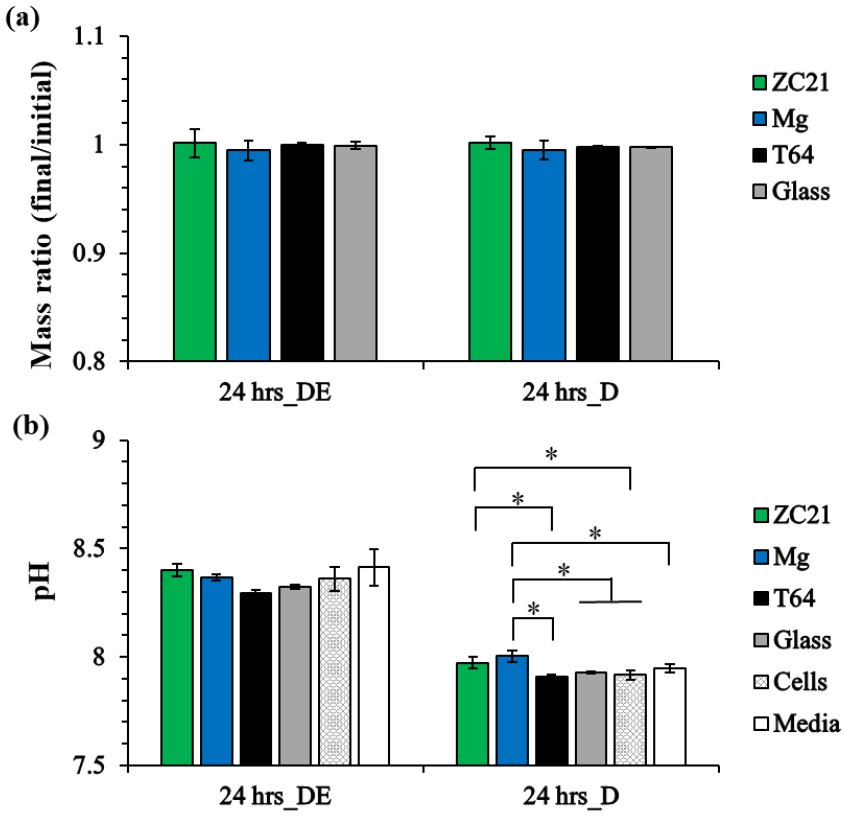

Figure 3-9. (a) Mass change ratio (final/initial mass) of ZC21, pure Mg control, T64 control and glass reference after 24h direct exposure culture and 24h direct culture; (b) pH values of the media collected from each well after 24h direct exposure culture and 24h direct culture. Data are expressed as mean ± standard deviation, n = 3; *p< 0.05.

from each well after 24-h direct exposure culture and 24-h direct culture. As expected, in both culture methods in Figure 3-9a, the mass change of all samples was small because of the short culture period. No statistically significant difference was found among the mass changes of all samples. As shown in Figure 3-9b, the pH values ranged from 8.3 to 8.4 among all the groups in direct exposure culture, and no statistically significant differences were found. In direct culture,

pH values ranged from 7.9 to 8 and the pH differences across the groups were small, even though statistically significant differences were found.

Figures 3-10a-c show the Mg^{2+}, Zn^{2+}, and Ca^{2+} ion concentrations in the media collected from each well after 24-h direct exposure culture and 24-h direct culture. In Figure 3-10a, in both culture methods, ZC21 and Mg control pins showed statistically higher Mg^{2+} ion concentrations than T64, glass, cell-only and media groups. After 24-h direct exposure culture, ZC21 showed the highest Mg^{2+} ion concentration, but no statistically significant difference was found between ZC21 and the Mg control group. Interestingly, after 24-h direct culture, Mg showed the highest Mg^{2+} ion concentration, but again no statistical difference between ZC21 and Mg was detected. In Figure 3-10b, as expected, the ZC21 group showed the highest Zn^{2+} ion concentration, which was statistically higher than all the other groups in both culture methods. In Figure 3-10c, after 24h direct exposure culture, ZC21 showed the lowest Ca^{2+} ion concentration in the post-culture media and a statistically significant difference was found between ZC21 and the cell-only control group. Interestingly, after 24-h direct culture, ZC21 showed the highest Ca^{2+} ion concentration, which was statistically higher than that of the T64, glass and media groups. Figure 3-10d shows the daily degradation rates of ZC21 and Mg, which were calculated based on the daily release rates of Mg^{2+} ions into the media after 24-h direct exposure culture and 24-h direct culture. In direct exposure culture, ZC21 showed a statistically higher degradation rate than Mg. In direct culture, Mg showed a higher average degradation rate than ZC21, but no statistically significant difference was found. Figures 3-10e-f show the crack width and crack area ratios on the surfaces of ZC21 and Mg, quantified based on SEM images after culture. In both culture methods, ZC21 showed statistically smaller crack width and crack area ratios than the Mg controls, indicating that ZC21 provided a more desirable degradation mode than Mg.

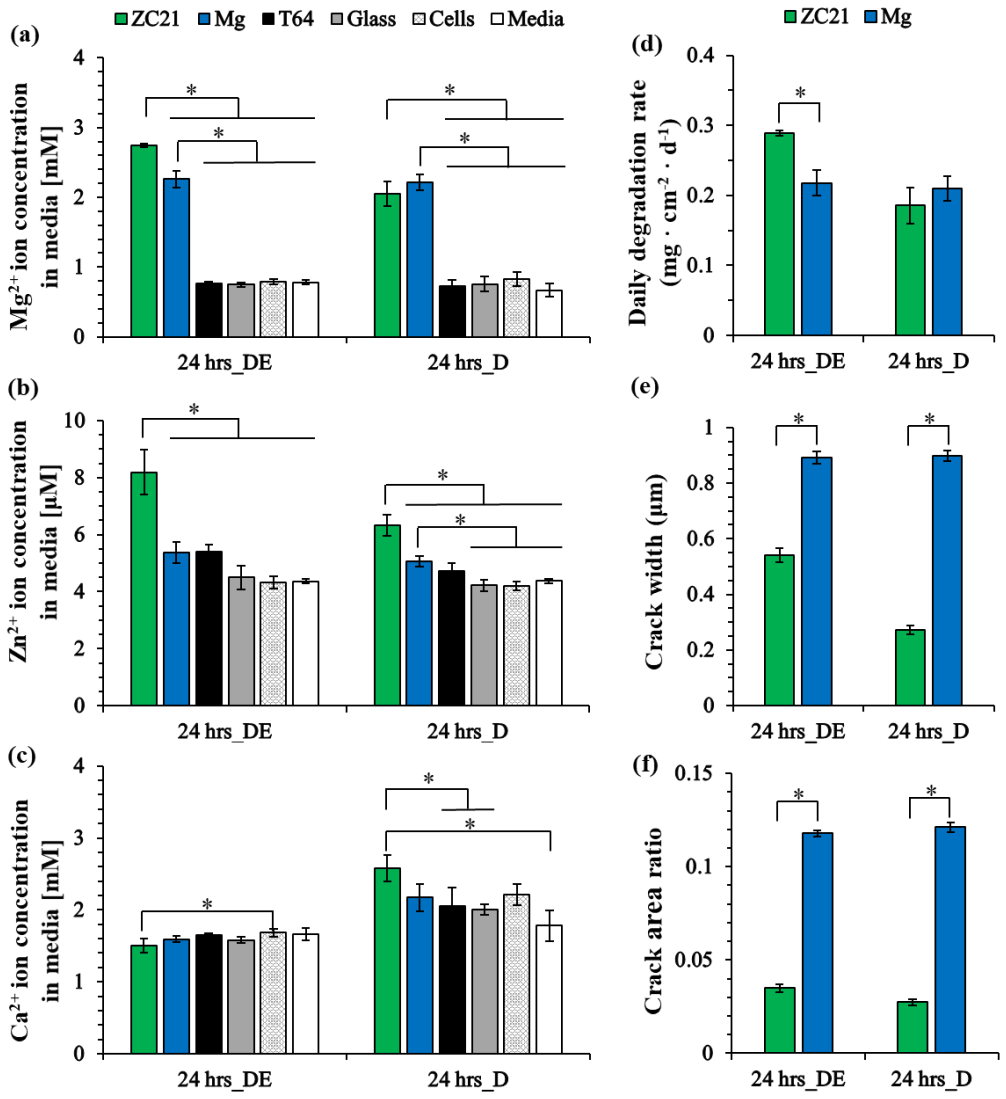

Figure 3-10. Degradation of ZC21 and Mg pins *in vitro* after 24-h direct exposure culture (DE) and 24-h direct culture (D). (a-c) Ion concentration in the media collected from each well after 24h DE and 24h D. (a) Mg^{2+} ion concentration; (b) Zn^{2+} ion concentration; (c) Ca^{2+} ion concentration. (d) The daily degradation rates of ZC21 and Mg after 24h DE and D.(e) Crack width on the surface of ZC21 and Mg after 24-h DE and D.(f) Crack area ratio on the surface of ZC21 and Mg after 24-h DE and D. Data are mean ± standard deviation, n = 3; *p< 0.05.

3.3.3. Antibacterial property of ZC21, ZSr41 and Mg pins *in vitro*

As shown in Figure 3-11a, after 24-h culture with MRSA, localized corrosion and cracks were observed on the surfaces of ZC21, ZSr41 and Mg in Figure 3-11a, and appeared more

clearly at the high original magnification of 5000x. Localized corrosion appeared more severe on the surface of ZSr41 when compared with that of ZC21 and Mg.

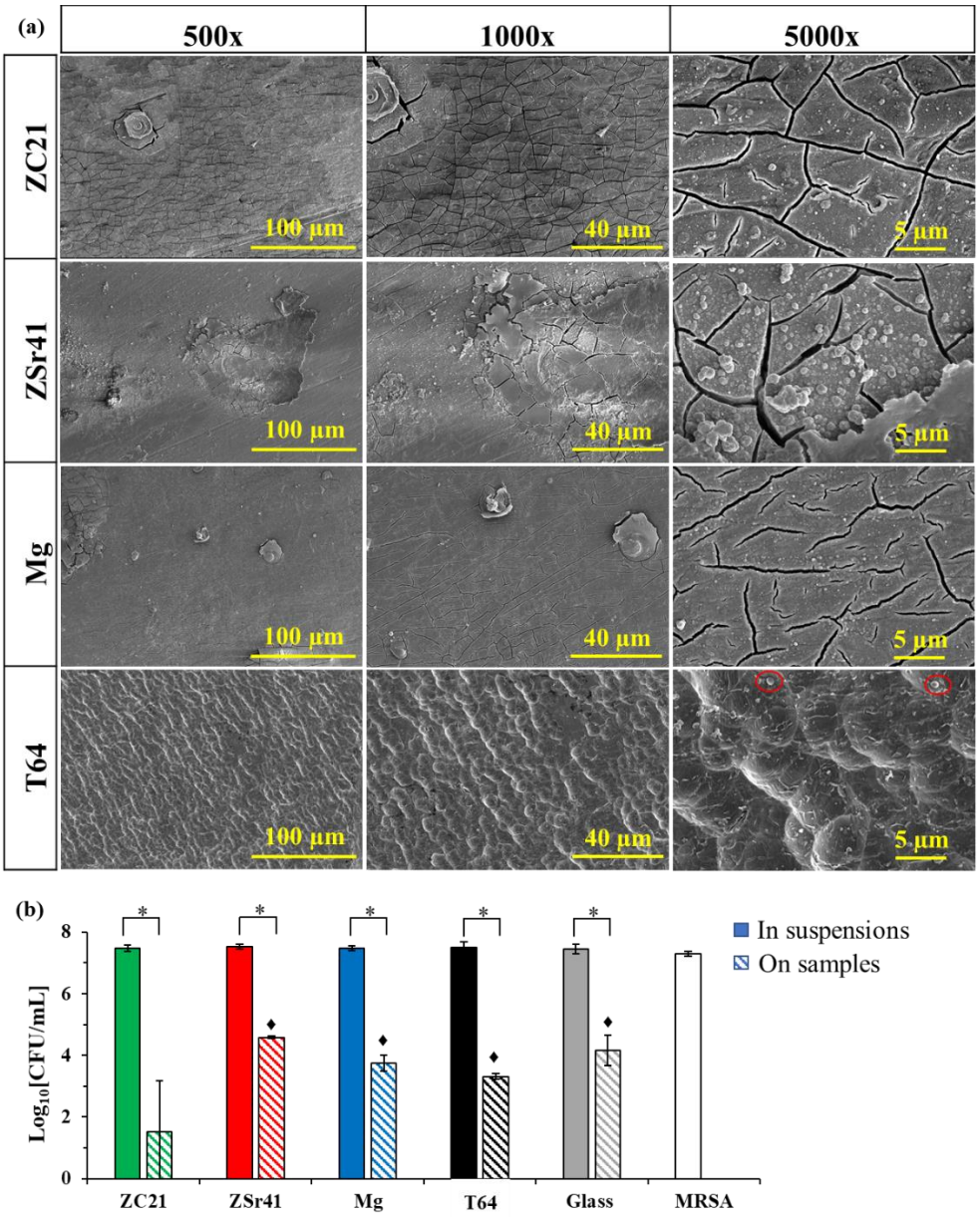

Figure 3-11. (a) SEM images of ZC21, ZSr41, Mg and T64 at the 500x, 1000x and 5000x original magnifications after 24-h culture with *methicillin-resistant Staphylococcus aureus (MRSA*). Red circles were used to highlight bacteria on the sample surface. (b) Colony forming units (CFU) quantified for the viable *MRSA* after 24-h culture with the samples and controls. Data are mean ± standard deviation, n = 3; *$p < 0.05$. ♦$p < 0.05$ when compared with the CFU on ZC21 samples.

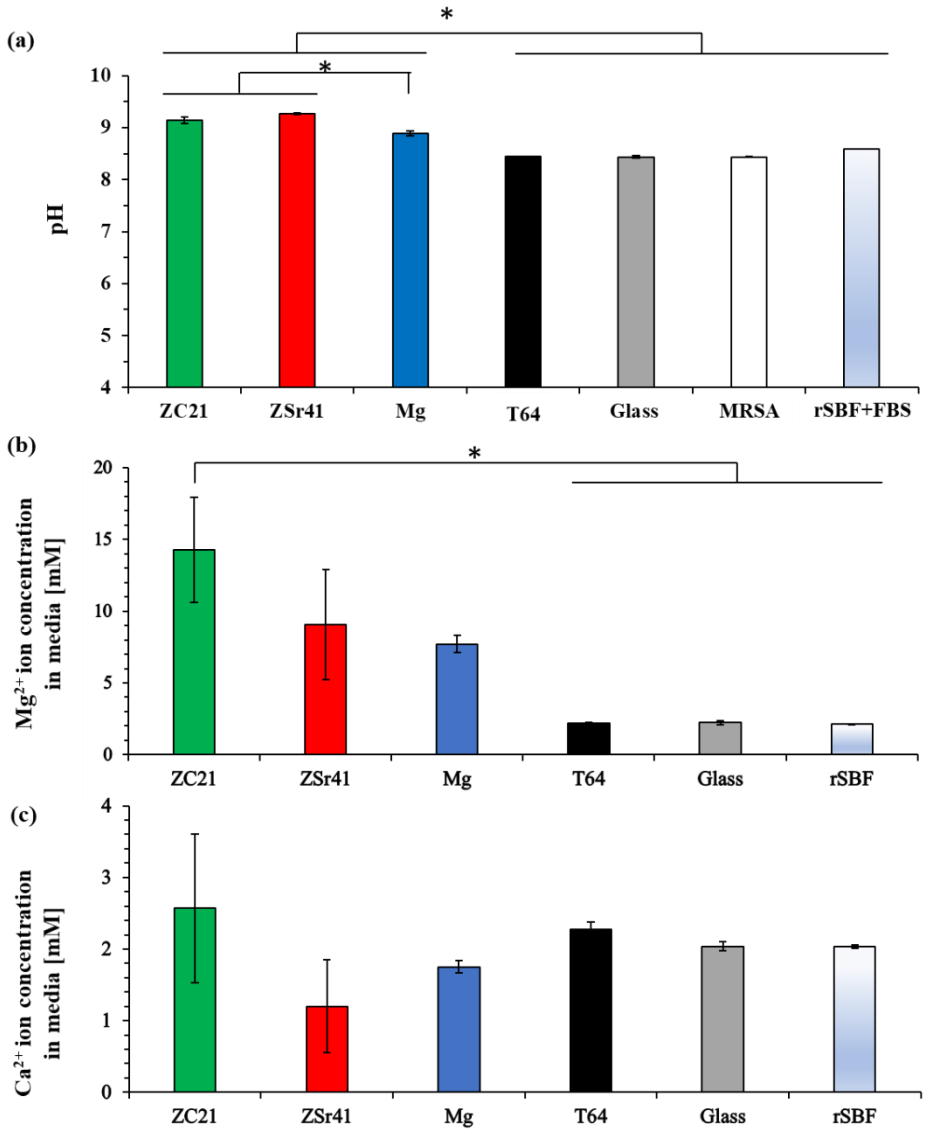

Figure 3-12. Degradation of ZC21, ZSr41 and Mg pins *in vitro* after 24-h bacterial culture with MRSA. (a) pH values of the media collected from each well after 24-h MRSA culture; (b) Mg^{2+} ion concentration and (c) Ca^{2+} ion concentration in the media collected from each well after 24-h MRSA culture. Data are mean ± standard deviation, n = 3; *$p < 0.05$.

The viable MRSA in the culture suspension and on the sample surface was quantified as the colony forming units (CFUs), after 24-h culture with each sample group, as shown in Figure

3-11b. No inhibition of MRSA growth in the culture suspensions was found for all groups. However, the CFUs of MRSA on Mg-based and control samples were all significantly lower than the respective CFU of MRSA in suspensions for the same sample or control groups. Generally, MRSA bacteria seem to grow in suspensions more than adhere onto the substrates, including the standard substrates of glass reference, which is in agreement with our previous finding [165]. Interestingly, the CFU of MRSA on the surface of ZC21 was significantly lower than the other groups including the T64 and glass control groups, indicating ZC21 surface had the strongest antibacterial activity against the adhesion and growth of MRSA.

As expected in Figure 3-12a, the pH values of post-culture broths collected from the groups of ZC21, ZSr41 and Mg were significantly higher than the control groups of T64, glass, MRSA only and broth only, because their degradation in rSBF with FBS released OH^- ions. The analysis of ionic concentrations in Figure 3-12b-c confirmed that Mg^{2+} ion concentrations in the groups of ZC21, ZSr41 and Mg were statistically higher than the control groups of T64, glass and rSBF only. The average Ca^{2+} ion concentrations in the groups of ZC21, ZSr41 and Mg were lower than the control groups because Ca-containing minerals deposited on the surface but no statistically significant difference was found.

3.3.4. *In vivo* study of ZC21, ZSr41 and Mg pins in mouse femoral defects

3.3.4.1. In vivo degradation of ZC21, ZSr41 and Mg pins and bone healing in the femoral defects

During the post-surgery observation period, neither wound complications nor implant failures occurred. Stable bone fixation was maintained in all animals throughout the *in vivo* study. Figure 3-13 shows representative radiographs of the mouse femoral bone defects at 4 weeks, 8 weeks and 12 weeks after implantation of ZC21, ZSr41 and Mg pins. The radiographs in Figure 12 confirmed the gradual degradation of ZC21, ZSr41 and Mg pins *in vivo*, and indicated different degrees of bone regeneration in the femoral defects in response to different pin implants.

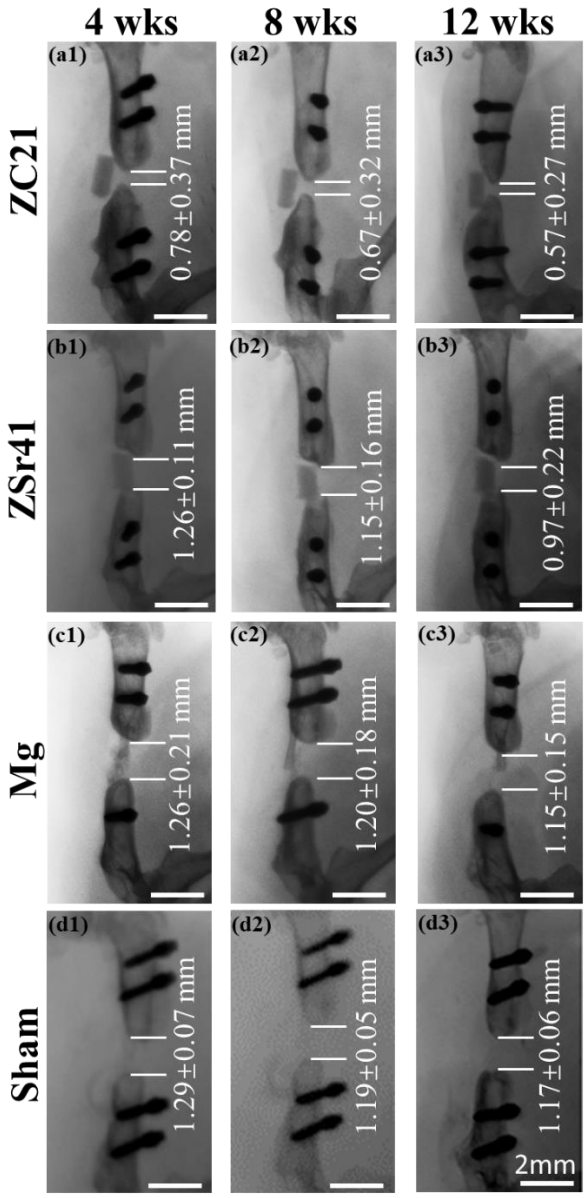

Figure 3-13. Representative radiographs of a mouse femoral bone with a defect filled with ZC21 (a1-a3), ZSr41 (b1-b3) and Mg (c1-c3) at 4 weeks, 8 weeks and 12 weeks after implantation. Sham designates the control group with a defect but no pin implant (d1-d3). The defect gap size at each time point is shown in each image; data are expressed as mean ± standard deviation. Scale bar = 2 mm for all radiographs.

Specifically, ZC21 pins (Figures 3-13a1-a3) and ZSr41 pins (Figures 3-13b1-b3) maintained their shape and structure with a slight volume reduction after 12 weeks of implantation. Mg pins (Figures 3-13c1-c3) had the fastest degradation among all of the Mg-based pins. After 8 weeks of

implantation, Mg pins became nearly invisible in radiographs. The ZC21 group achieved the most promising healing results when compared with the other two Mg-based groups and the sham group. In the ZC21 group, the sizes of the gaps between the bone ends reduced to 0.78±0.37mm, 0.67±0.32mm and 0.57±0.27mm at 4 weeks, 8 weeks and 12 weeks after implantation, respectively. The gaps in the ZSr41 group were 1.26±0.11 mm, 1.15±0.16 mm and 0.97±0.22 mm at 4 weeks, 8 weeks and 12 weeks after implantation, respectively. The gaps in the Mg group were 1.26±0.21 mm, 1.20±0.18 mm and 1.15±0.15 mm at 4 weeks, 8 weeks and 12 weeks after implantation, respectively. The sham group with no implants showed the gap sizes of 1.29±0.07 mm, 1.19±0.05 mm and 1.17±0.06 mm at 4 weeks, 8 weeks and 12 weeks after implantation, respectively. Clearly, the size of gap defect in the ZC21 group became the smallest at the prescribed time points when compared with the other groups, indicating that ZC21 pins had the highest osteogenic potential for bone healing and regeneration.

3.3.4.2. Surface characterization of ZC21 and ZSr41 pins after in vivo implantation

Figure 3-14 shows the surface morphology and degradation properties of ZC21, ZSr41 and Mg pins before and after 12 weeks of *in vivo* implantation in a mouse femoral defect. ZC21 retained its shape and showed a slight volume reduction. White degradation layers covered the surface of ZC21, as shown in Figure 3-14a. ZSr41 also developed white deposits on the surface, similar to ZC21, but ZSr41 had more volume reduction than ZC21. Mg completely degraded after 12 weeks. After 12 weeks of implantation, the average mass ratio (final/initial mass) was 0.32 for ZC21, 0.14 for ZSr41, and 0 for Mg, as shown in Figure 3-14b. These ratios serve as an indicator of the *in vivo* degradation of ZC21, ZSr41 and Mg pins. Specifically, the daily degradation rates of ZC21, ZSr41 and Mg were calculated to be 0.28±0.09 $mg \cdot cm^{-2} \cdot d^{-1}$, 0.37±0.09 $mg \cdot cm^{-2} \cdot d^{-1}$, and 0.63 $mg \cdot cm^{-2} \cdot d^{-1}$, respectively (Figure 3-14c). The daily degradation rate of Mg was calculated based on the initial sample mass and 12-week degradation time, since Mg pins fully degraded by

12 weeks. The crack width and crack area on the surfaces of ZC21 and ZSr41 were identified on the SEM images of the pin samples in Figures 3-14d-e after implantation. The cracks on the exposed surfaces of ZC21 and ZSr41 are clearly visible in these figures. Figures 3-14f and 3-14g show the quantified crack width and crack area ratios for ZC21 and ZSr41, respectively. Specifically, ZC21 showed a mean crack width of 8.05±0.23 μm, which was significantly greater than that of ZSr41. However, the average crack area ratio of ZC21 was slightly less than that of ZSr41, though there was no statistically significant difference.

The residual ZC21 and ZSr41 pins that were dissected out after 12 weeks of implantation in a mouse femur were characterized, as shown in Figure 3-15. Degradation products covered most of the surfaces of ZC21 and ZSr41 pins, as shown in Figures 3-15a1 and 3-15b1, respectively. The corresponding EDS elemental distribution maps in Figures 3-15a2-a8 and 3-15b2-b8 revealed the deposition of Ca and P *in vivo* and the presence of Mg, C, O, Na and K on the surfaces of both ZC21 and ZSr41, which were confirmed by the surface elemental composition (wt. %) quantified through EDS area analyses in Figure 3-15c. Specifically, the ZC21 pin had (wt.%) 10.5% Mg, 13.0% C, 44.8% O, 18.2% P, 5.8% Ca, 7.7% Na/K on the surface; the ZSr41 pin showed (wt.%) 9.6% Mg, 11.7% C, 45.4% O, 17.2% P, 9.0% Ca, 7.1% Na/K on the surface. XRD results in Figure 3-15d confirmed the presence of $Mg_3(PO_4)_2 \cdot 8H_2O$, $MgCO_3 \cdot 3H_2O$ and $CaCO_3$ phases on the surfaces of ZC21 and ZSr41 pins after 12 weeks of implantation. Additionally, in Figure 3-15e, O-H, C=C, and CO_3^{2-} functional groups were identified in the FTIR spectra of ZC21 and ZSr41 after *in vivo* implantation.

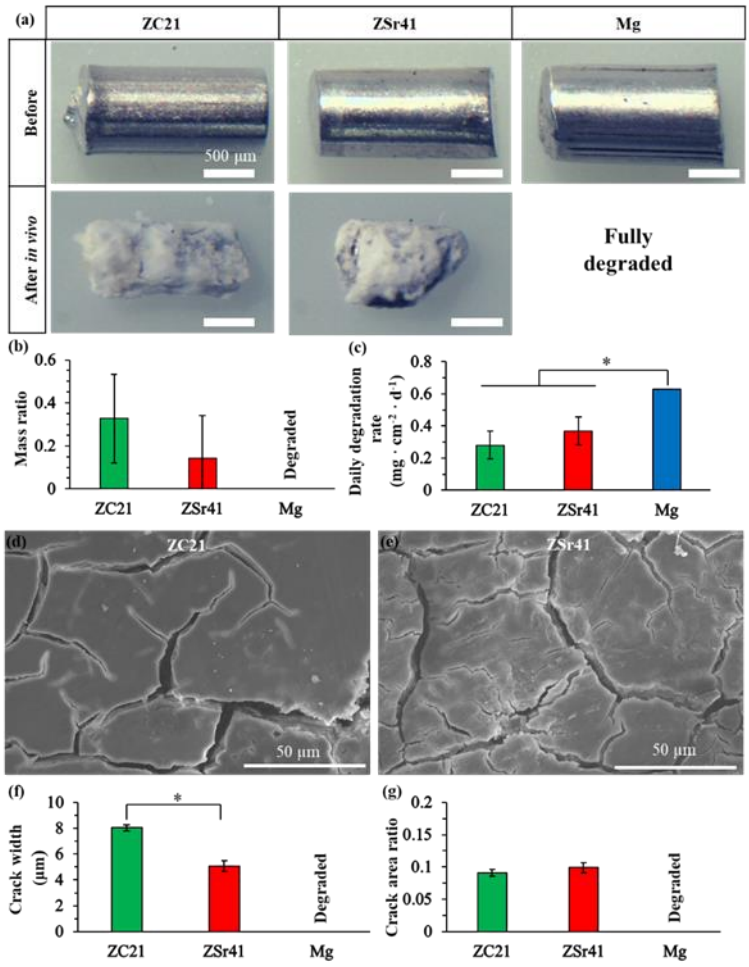

Figure 3-14. Surface morphology, mass change and degradation characterization of ZC21, ZSr41 and Mg before and after 12weeks of *in vivo* implantation in mouse femoral defects. (a) Microscopic images of ZC21, ZSr41 and Mg before and after 12-week *in vivo* implantation. Scale bar = 500 μm for all images; (b) Mass ratio (final/initial mass) of ZC21, ZSr41 and Mg after 12-week *in vivo* implantation; (c) Daily degradation rate of ZC21, ZSr41 and Mg during 12-week *in vivo* implantation; (d) SEM image of ZC21 surface at an original magnification of 1000x. Image was taken on the surface region of ZC21 where the loose degradation layer was removed to identify crack width and area; (e) SEM image of ZSr41 surface at an original magnification of 1000x. Image was taken on the surface region of ZSr21 where the loose degradation layer was removed to identify crack width and area; (f) Crack width on the surface of ZC21 and ZSr41 after 12-week *in vivo* implantation; (f) Crack area ratio on the surface of ZC21 and ZSr41 after 12-week *in vivo* implantation. Data are expressed as mean ± standard deviation, n = 3; *p< 0.05.

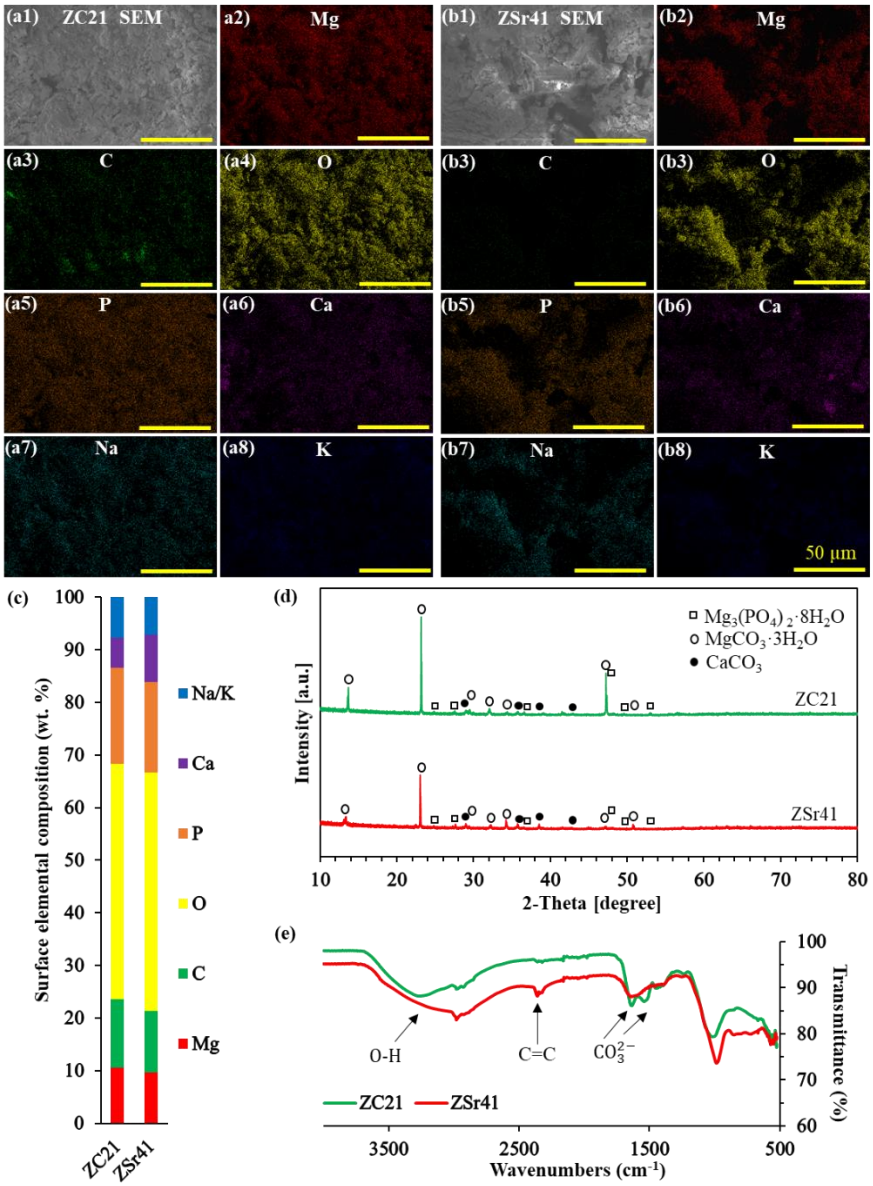

Figure 3-15. Characterization of residual ZC21 and ZSr41 intramedullary pins dissected out after implantation in mouse femoral defects for 12 weeks. (a1-a8) SEM images of the deposition on ZC21 surface and corresponding surface elemental distribution maps (Mg, C, O, P, Ca, Na and K).(b1-b8) SEM image of the deposition on ZSr41 surface and corresponding surface elemental distribution maps (Mg, C, O, P, Ca, Na and K).(c) Surface elemental composition (wt. %) quantified through EDS area analysis on SEM images of ZC21 and ZSr41 in (a1) and (b1).(d) XRD spectra of the surface of the residual ZC21 and ZSr41 intramedullary pins.(e) FTIR spectra of the surface of the residual ZC21 and ZSr41 intramedullary pins. Original magnification was 1000x and scale bar = 500 μm for all SEM images and EDS maps.

3.4 Discussions

In this study, we investigated the degradation and cytocompatibility of Mg–Zn–Ca alloy in two different cell culture methods, studied the effects of soluble and insoluble degradation products on cell adhesion and viability *in vitro*, analyzed different degradation behaviors of Mg–Zn–Ca alloy *in vitro* and *in vivo*, compared the antibacterial effects of Mg–Zn–Ca alloy and degradation in bacterial culture with a previous Mg-Zn-Sr alloy, and compared the degradation rates of Mg alloys of interest in different *in vitro* culture systems (including both BMSC culture and MRSA bacterial culture) versus *in vivo* in an animal model.

3.4.1. Improved *in vitro* cytocompatibility and antibacterial property and enhanced bone regeneration *in vivo* for ZC21 pins

Cytocompatibility of various as-cast Mg-Zn-Ca alloys with bone marrow derived mesenchymal stem cells (BMSCs) has been studied previously using the direct culture method *in vitro* [1]. It is still necessary to study the as-drawn ZC21 pins in BMSC culture, because the different processing conditions for as-cast Mg-Zn-Ca alloy plates versus as-drawn wires could lead to different cell responses, even when the alloy composition is the same. In addition to the direct culture method, the direct exposure culture method was included in this study to mimic the *in vivo* interactions of the ZC21 pin implants with established BMSCs in the body. The ZC21 alloy was found to be cytocompatible with BMSCs under direct contact and indirect contact conditions in both of the culture methods in this study. The cells face different surface and local environment under the direct versus indirect contact conditions even in the same culture wells. Generally, the factors that affect BMSC adhesion and function on and around Mg-based materials include surface microstructure and composition as well as the presence of degradation products, both soluble and insoluble. Soluble degradation products include the ions such as Mg^{2+}, Zn^{2+}, Ca^{2+}, and OH^- ions that affect media pH and composition when they were released into the media.

Insoluble degradation products include non-degradable compounds formed on the surface of Mg alloys during the degradation and precipitation processes such as hydroxides, carbonates and phosphates. Under the direct contact condition, surface microstructure and insoluble degradation products on the sample surface play key roles on cell adhesion, while the dynamic pH and ion concentrations at the sample surface affect cell adhesion and functions as well. In contrast, under indirect contact condition, soluble degradation products released into the media, i.e. media pH and ion concentrations, are the key factors that influence cell adhesion and functions, because cells have no contact with sample surface. When the chemistry and microstructure at the sample surface are beneficial for cell growth, it is possible to have higher cell density in direct contact condition than indirect contact condition. For example, the cell density on ZC21 surface (direct contact) was higher than that on plate (indirect contact) in both culture methods; in contrast, the cell density on Mg surface was lower than that on plate in both culture methods. Because the ZC21 and Mg pins were polished following the same method before cell culture, we expected them to have similar surface roughness. Thus, this factor was not considered as primarily responsible for the differences observed in BMSC adhesion and spreading between the ZC21 and Mg groups in this study. Comprehensive characterization of their surface microstructure and composition suggested that the formation of Ca-containing minerals on the surface of ZC21 likely created a more favorable interface for the attachment and spreading of BMSCs under direct contact conditions. Specifically, after BMSC culture, more deposits appeared on the surface of ZC21 than on Mg (Figures 3-4 and 3-5a). Based on EDS analyses (Figure 3-5), the Ca content on ZC21 was higher than on pure Mg after both direct exposure and direct cultures, indicating more Ca deposition on the surface of ZC21. The XRD spectra (Figure 3-6) confirmed the presence of $Ca(OH)_2$ phase on the surface of ZC21 after direct exposure culture and the presence of $Ca(OH)_2$ and $CaCO_3$ phases after direct culture, but no Ca-containing minerals were detected on the surface

of Mg in either culture method. In direct exposure culture, Ca^{2+} ion concentration in the culture with ZC21 alloy was the lowest among all groups, suggesting that some Ca in the media might have been deposited into the degradation layer on the ZC21 surface. Interestingly, in direct culture, the ZC21 alloy showed the highest Ca^{2+} ion concentration among all groups, indicating possible Ca^{2+} release from the ZC21 alloy to the media. Intracellular Ca^{2+} released from BMSCs should not contribute much to the Ca^{2+} ion concentration in the media because the intracellular Ca concentrations for most cells are in the range of 0.1 - 1 μM [166], which is much lower than the Ca levels of 1 - 3mM in the culture media. The results in Figure 8c confirmed this, since no significant difference was found in Ca^{2+} ion concentrations between the cell-only and media-only reference groups. Therefore, insoluble Ca-containing degradation products on the surface of ZC21, deposited from the media or originating from the ZC21 alloy, could be the main factor that promoted BMSC adhesion on ZC21 pins to a greater extent than on pure Mg pins under the direct contact conditions of both culture methods.

Soluble degradation products are the major factors that affect BMSC behaviors in indirect contact conditions. The soluble degradation products include OH^- ions and metallic ions such as Mg^{2+}, Zn^{2+} and Ca^{2+}. The pH values of the media as well as the Mg^{2+}, Zn^{2+} and Ca^{2+} ion concentrations in the media of all groups in both culture methods of this study were well below cytotoxic values reported in literature [1, 87]. Accordingly, BMSCs showed high viability under indirect contact conditions in both culture methods for all groups. As shown in Figure 8b, the pH values of all groups were around 8.4 in direct exposure culture and were around 8.0 for all groups in direct culture. Our previous study showed that BMSC viability reduced significantly at pH 9.5, but BMSCs showed no statistical difference in viability when the media pH was initially adjusted to 8-9 [1]. Since our results showed that BMSCs remained viable on and around ZC21 pins in both culture methods, the local pH probably had little influence on cell viability. The bicarbonate

buffering system of DMEM, which is similar to the buffering system in the human body, could effectively mediate the alkalinity (transient pH<9.0) back to normal conditions for cell culture [1, 167]. As for Mg^{2+} ions, attached and viable BMSCs with similar densities were observed after 24 h of culture in DMEM supplemented with 0–27.6 mM Mg^{2+} ion concentration in the previous study [1]. In this study, Mg^{2+} ion concentrations in all groups after 24 h culture in the range of 0.7-3.0 mM, as shown in Figure 10a, are in the cytocompatible range. ZC21 also released Zn^{2+} and Ca^{2+} ions during degradation, but the amounts of Zn^{2+} and Ca^{2+} ions released from ZC21 were much lower than that of Mg^{2+} ions, as Zn and Ca were alloying elements present in smaller amounts in the samples. More importantly, the measured 4-8 μM Zn^{2+} and 1.5-2.6 mM Ca^{2+} ion concentrations for all groups in both culture methods in this study were well below their respective cytotoxic values reported in literature (60 μM for Zn and 30 mM for Ca) [168].

Cytocompatibility of ZSr41 alloys with BMSCs has been reported in our previous publications [2, 3]. The behaviors of BMSCs in the direct culture with four as-rolled Mg-4Zn-xSr alloys (x = 0.15, 0.5, 1.0, 1.5 wt %) were first studied, and the results showed that BMSCs exhibited higher viability on Mg-4Zn-1Sr (ZSr41) and Mg-4Zn-1.5Sr than Mg-4Zn-0.5Sr and Mg-4Zn-0.15Sr [3]. The as-rolled Mg-Zn-Sr alloy samples had a dimension of 5mm×5mm×1mm. Collectively considering the properties of the four Mg-4Zn-xSr alloys, ZSr41 was chosen to be further studied as intramedullary pins *in vitro* with BMSCs and *in vivo* in rat tibia [2]. The as-drawn ZSr41 pins showed a general trend of increasing cell densities with increasing incubation time from 24 to 72 hours, when they were cultured with BMSCs using the exposure culture method, which indicated cell proliferation over time [2]. The as-drawn ZSr41 pins showed a complete resorption time of 8 weeks and a significant net bone growth because of stimulatory effects of the metallic ions released, when they were implanted as intramedullary pins in rat tibia. Therefore, the same as-drawn ZSr41 pins as previously studied [2] were included in the bacterial

culture with MRSA and implanted in the mouse femoral defect *in vivo* in this study for comparison. The ZSr41 alloy has been previously studied in BMSC culture [2, 3], but this was the first study to examine the ZSr41 alloy in bacterial culture and in femoral defects, along with the ZC21 alloy and pure Mg control.

ZC21 pins showed the strongest capacity for osteogenic induction and bone healing in a mouse femoral segmental defect *in vivo*. The addition of Zn and Ca alloying elements in ZC21 improved the biocompatibility and degradation properties while promoting bone healing. The x-ray images of mouse femur clearly showed that the ZC21 group induced bone growth and reduced the defect gap more than the ZSr41 group and pure Mg group. The *in vitro* bacterial study demonstrated that MRSA adhesion significantly reduced on the surface of ZC21 when compared with ZSr41 and pure Mg. Overall, bioresorbable ZC21 alloy is promising for antimicrobial bone implant applications, such as internal fixation devices (IFDs) for repairing bone fractures, to replace current standard IFDs made of Ti alloys or stainless steels to reduce infections and eliminate the need of secondary surgeries for implant removal. Further *in vivo* studies on bone remodeling in an infection model using microcomputed tomography (microCT) and histological methods are necessary to fully elucidate the relationships between alloy degradation and the associated biological responses. Surface modifications or coatings could be applied to the ZC21 alloy to further reduce the alloy degradation while improving bone regeneration to meet the requirements for specific clinical applications.

3.4.2. Degradation behaviors of ZC21 pins *in vitro* and *in vivo* in comparison with controls

The daily degradation rates, corrosion crack width and crack area ratio on the surface were quantified to compare the degradation behaviors of ZC21and Mg pins *in vitro* and *in vivo*. In the 24-h BMSC/DMEM culture system *in vitro*, the daily degradation rate of ZC21 was statistically faster than that of Mg in the direct exposure culture, but was lower in the direct

culture and no statistical difference was detected. However, for both culture methods, the crack width and crack area ratio on the surface of ZC21 were statistically smaller than Mg, indicating more desirable degradation mode. Larger corrosion cracks on Mg might cause severe corrosion in the longer term than 24 h and might release larger pieces of degradation products, which could cause catastrophic failure later. Even though ZC21 showed higher degradation rate than Mg in 24-h direct exposure culture, the degradation mode of ZC21 may lead to more uniform and slower degradation in the longer term *in vivo*. Indeed, after 12 weeks of implantation in mouse femoral defect model, ZC21 pins still largely retained their shape but Mg pins were completely degraded, confirming that ZC21 pins degraded much slower than Mg pins *in vivo*.

Intrinsic properties such as the composition, microstructure, processing conditions, dimension, geometry, and surface conditions of samples are key factors that could affect the degradation behaviors of Mg-based materials. However, the effects of these material factors on sample degradation are manifested differently when coupled with different environmental conditions present *in vitro* and *in vivo*. The cells, proteins, and ions in the *in vitro* BMSC/DMEM culture system could affect the degradation behaviors of Mg-based materials. Interestingly, ZC21 showed a higher daily degradation rate, coupled with a greater crack width and crack area ratio in the direct exposure culture than in the direct culture, suggesting different culture methods did affect its *in vitro* degradation behaviors. Furthermore, in the direct exposure culture, cells that had already been established for 24 h before the introduction of ZC21 pins could release acidic metabolites into the media. The presence of pre-established cells and acidic metabolites prior to introduction of the sample pins appeared to affect the degradation of ZC21 more than that of pure Mg, as shown in Figure 3-10d-f.

The *in vivo* environment is more dynamic and complex than *in vitro* culture systems, and more factors such as the selection of different animal models, the location of implantation, and

the conditions of fluid flow and loading at the implantation sites could affect the *in vivo* degradation of Mg-based materials. For example, the addition of Zn as an alloying element could improve tensile and creep strength [141] and enhance the corrosion resistance of Mg alloys. However, such benefits may not be clearly shown in the *in vitro* culture systems because of the relatively static environment, lack of mechanical stress, and short culture duration. In contrast, the beneficial roles of Zn and Ca alloying elements on Mg-based materials were clearly expressed in the *in vivo* system used here because of the dynamic environment with systemic fluid flow and mechanical stress. ZC21 demonstrated significantly better degradation performance than pure Mg after 12 weeks of implantation *in vivo*. In this study, the ZSr41 control pins also partially retained their shape and had a slower degradation rate than Mg pins after 12 weeks of implantation in a mouse femoral defect. In a previous study, ZSr41pins had a significantly faster degradation rate than pure Mg pins in a rat tibia model during *in vivo* implantation for 47 days [2]. The difference in the degradation behaviors of ZSr41 pins in these two studies was most likely caused by the differences in the animal models (segmental defect in a mouse femur versus medullary cavity in a rat tibia), and different fluid flow and loading conditions at the two different implantation sites.

Finally, the average daily degradation rates of ZC21, ZSr41 and Mg pins *in vitro* and *in vivo* from this study were compared with the values from the previous *in vitro* and *in vivo* studies, and the results are summarized in Figure 3-16. It is important to pay attention to all the key parameters included in Figure 3-16 that could affect the degradation results, including sample dimension, different processing parameters, and experimental conditions such as medium type and animal model, even when the alloy composition is the same. When the experimental conditions varied, the calculated average daily degradation rates of the alloys that had the same composition might be different. Specifically, the results from the following studies were compared with the degradation results of this study: the average daily degradation rates of ZC21

and Mg sheets in the direct culture (abbreviated as D) with BMSCs in DMEM media (averaged from 3 days) [1], ZSr41 and Mg intramedullary pins in rat tibia (averaged from 47 days) [2], ZSr41 and Mg pins in exposure culture (abbreviated as E, i.e., samples were placed in Transwell® inserts in the culture well with BMSCs in DMEM media) that were averaged from 3 days [2], and the average daily degradation rates of ZSr41 and Mg sheets in direct culture (D) with BMSCs in DMEM media (averaged from 3 days)[3]. The comparison in Figure 3-16 demonstrated that the degradation rates of ZC21, ZSr41 and Mg varied dramatically under different experimental conditions *in vitro* and *in vivo*. In addition to the alloy composition, material factors such as processing conditions, sample geometry, and sample dimension, as well as environmental factors associated with the differences between *in vitro* culture methods and *in vivo* models, could influence the degradation behaviors of the samples, which should be carefully considered when comparing the degradation behaviors *in vitro* and *in vivo*. ZC21 showed similar degradation rates in the direct culture and direct exposure culture with BMSCs in DMEM because of the same sample dimension, the same type of culture media and the same volume of culture media. However, the degradation rate of ZC21 increased dramatically in the culture with MRSA in rSBF+FBS in comparison with the BMSC+DMEM culture system, likely because of the differences in the sample size (5 mm length versus 15 mm length), the culture media (rSBF+FBS versus DMEM), and the volume of culture media (0.75 mL versus 3 mL). The degradation rate of ZC21 *in vivo* was close to that in the BMSC+DMEM culture system. Overall, the *in vitro* cell culture systems with relevant cell and media types could simulate certain *in vivo* physiological conditions with the presence of relevant ions, proteins and cells, which is useful for initial screening studies of Mg-based materials, but *in vivo* studies in relevant animal models are still necessary.

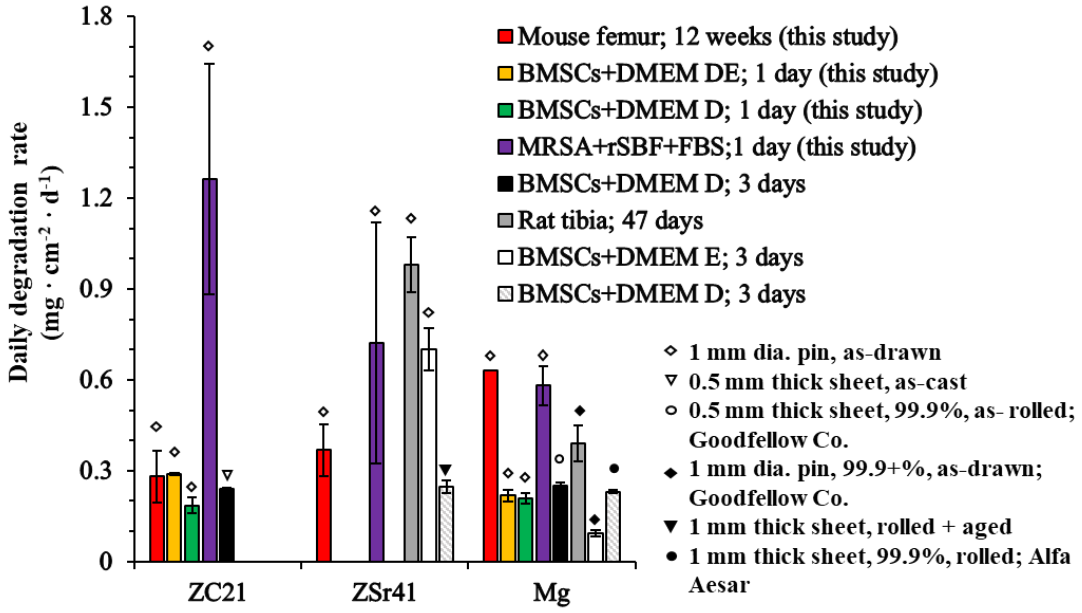

Figure 3-16. Average daily degradation rates of ZC21, ZSr41 and Mg pins *in vitro* and *in vivo* from this study, in comparison with the daily degradation rates of these materials from previous studies [1-3]. The color and pattern of each bar designate the model system, i.e. culture system, media type, culture method, and culture time for *in vitro* studies, and animal model type, anatomical location, and implantation time for *in vivo* studies. The icon above each bar designates the properties of respective samples (i.e. geometry, purity, processing conditions for customized Mg and its alloys, and the source for commercially procured pure Mg).

3.5 Conclusions

This article reported for the first time on the cytocompatibility and *in vitro* degradation of ZC21 pins in the direct exposure culture and direct culture, the antibacterial activities of ZC21 against MRSA bacteria, and on the *in vivo* degradation and osteogenic potential of ZC21 pins in a mouse femoral defect model. The BMSC adhesion density on ZC21 pins was significantly higher than on Mg pins in both *in vitro* culture methods; the cell adhesion density around ZC21 pins was similar to the cell-only positive control in both *in vitro* culture methods, which confirmed that ZC21 is cytocompatible with BMSCs. The ZC21 pins showed fewer corrosion cracks on the surface than Mg pins after 24-h *in vitro* culture, and significantly slower degradation than pure

Mg pins after 12 weeks of *in vivo* implantation. ZC21 surface showed more significant antibacterial properties than ZSr41 and Mg in the 24-h culture with MRSA. Furthermore, the ZC21 group demonstrated the most promising bone healing in mouse femoral defects when compared with ZSr41 alloy and Mg pins after 12 weeks of *in vivo* implantation. Thus, ZC21 alloys should be further studied toward clinical translation for biodegradable implant applications.

References

[1] A.F. Cipriano, A. Sallee, R.G. Guan, Z.Y. Zhao, M. Tayoba, J. Sanchez, H.N. Liu, Investigation of magnesium-zinc-calcium alloys and bone marrow derived mesenchymal stem cell response in direct culture, Acta Biomater 12 (2015) 298-321.

[2] A.F. Cipriano, J.J. Lin, A. Lin, A. Sallee, B. Le, M.C.C. Alcaraz, R.G. Guan, G. Botimer, S. Inceoglu, H.N. Liu, Degradation of Bioresorbable Mg-4Zn-1Sr Intramedullary Pins and Associated Biological Responses in Vitro and in Vivo, ACS Appl Mater Interfaces 9(51) (2017) 44332-44355.

[3] A.F. Cipriano, A. Sallee, R.G. Guan, A. Lin, H.N. Liu, A Comparison Study on the Degradation and Cytocompatibility of Mg-4Zn-xSr Alloys in Direct Culture, Acs Biomater Sci Eng 3(4) (2017) 540-550.

[4] Y. Zhang, J. Xu, Y.C. Ruan, M.K. Yu, M. O'Laughlin, H. Wise, D. Chen, L. Tian, D. Shi, J. Wang, S. Chen, J.Q. Feng, D.H. Chow, X. Xie, L. Zheng, L. Huang, S. Huang, K. Leung, N. Lu, L. Zhao, H. Li, D. Zhao, X. Guo, K. Chan, F. Witte, H.C. Chan, Y. Zheng, L. Qin, Implant-derived magnesium induces local neuronal production of CGRP to improve bone-fracture healing in rats, Nat Med 22(10) (2016) 1160-1169.

[5] W.S. Jiang, Q.M. Tian, T. Vuong, M. Shashaty, C. Gopez, T. Sanders, H.N. Liu, Comparison Study on Four Biodegradable Polymer Coatings for Controlling Magnesium Degradation and human Endothelial Cell Adhesion and Spreading, Acs Biomater Sci Eng 3(6) (2017) 936-950.

[6] J.Y. Lock, E. Wyatt, S. Upadhyayula, A. Whall, V. Nunez, V.I. Vullev, H. Liu, Degradation and antibacterial properties of magnesium alloys in artificial urine for potential resorbable ureteral stent applications, J Biomed Mater Res A 102(3) (2014) 781-792.

[7] C. Zhang, N. Driver, Q. Tian, W. Jiang, H. Liu, Electrochemical deposition of conductive polymers onto magnesium microwires for neural electrode applications, J Biomed Mater Res A 0(0) (2018).

[8] M. Sebaa, T.Y. Nguyen, S. Dhillon, S. Garcia, H.N. Liu, The effects of poly(3,4-ethylenedioxythiophene) coating on magnesium degradation and cytocompatibility with human embryonic stem cells for potential neural applications, J Biomed Mater Res A 103(1) (2015) 25-37.

[9] I. Johnson, K. Akari, H.N. Liu, Nanostructured hydroxyapatite/poly(lactic-co-glycolic acid) composite coating for controlling magnesium degradation in simulated body fluid, Nanotechnology 24(37) (2013).

[10] R.G. Guan, A.F. Cipriano, Z.Y. Zhao, J. Lock, D. Tie, T. Zhao, T. Cui, H.N. Liu, Development and evaluation of a magnesium-zinc-strontium alloy for biomedical applications - Alloy processing, microstructure, mechanical properties, and biodegradation, Mater Sci Eng C Mater Biol Appl 33(7) (2013) 3661-3669.

[11] I. Johnson, H. Liu, A Study on Factors Affecting the Degradation of Magnesium and a Magnesium-Yttrium Alloy for Biomedical Applications, Plos One 8(6) (2013).

[12] S. Bagherifard, D.J. Hickey, S. Fintová, F. Pastorek, I. Fernandez-Pariente, M. Bandini, T.J. Webster, M. Guagliano, Effects of nanofeatures induced by severe shot peening (SSP) on mechanical, corrosion and cytocompatibility properties of magnesium alloy AZ31, Acta Biomater 66 (2018) 93-108.

[13] X.J. Wang, D.K. Xu, R.Z. Wu, X.B. Chen, Q.M. Peng, L. Jin, Y.C. Xin, Z.Q. Zhang, Y. Liu, X.H. Chen, G. Chen, K.K. Deng, H.Y. Wang, What is going on in magnesium alloys?, J Mater Sci Technol (2017).

[14] J. Zhang, S. Hiromoto, T. Yamazaki, J. Niu, H. Huang, G. Jia, H. Li, W. Ding, G. Yuan, Effect of macrophages on in vitro corrosion behavior of magnesium alloy, J Biomed Mater Res A 104(10) (2016) 2476-2487.

[15] I. Johnson, S.M. Wang, C. Silken, H. Liu, A systemic study on key parameters affecting nanocomposite coatings on magnesium substrates, Acta Biomater 36 (2016) 332-349.

[16] D.W. Zhao, F. Witte, F.Q. Lu, J.L. Wang, J.L. Li, L. Qin, Current status on clinical applications of magnesium-based orthopaedic implants: A review from clinical translational perspective, Biomaterials 112 (2017) 287-302.

[17] A. Witecka, A. Yamamoto, W. Swieszkowski, Influence of SaOS-2 cells on corrosion behavior of cast Mg-2.0Zn0.98Mn magnesium alloy, Colloids Surf B Biointerfaces 150 (2017) 288-296.

[18] W. Jiang, A.F. Cipriano, Q. Tian, C. Zhang, M. Lopez, A. Sallee, A. Lin, M.C.C. Alcaraz, Y. Wu, Y. Zheng, H. Liu, In Vitro Evaluation of MgSr and MgCaSr Alloys via Direct Culture with Bone Marrow Derived Mesenchymal Stem Cells, Acta Biomater (2018).

[19] Q. Tian, H. Liu, Electrophoretic deposition and characterization of nanocomposites and nanoparticles on magnesium substrates, Nanotechnology 26(17) (2015).

[20] A.F. Cipriano, J.J. Lin, C. Miller, A. Lin, M.C.C. Alcaraz, P. Soria, H.N. Liu, Anodization of magnesium for biomedical applications - Processing, characterization, degradation and cytocompatibility, Acta Biomater 62 (2017) 397-417.

[21] J.H. Lee, H. Kim, J.H. Kim, S.H. Lee, Soft implantable microelectrodes for future medicine: prosthetics, neural signal recording and neuromodulation, Lab Chip 16(6) (2016) 959-76.

[22] V.S. Polikov, P.A. Tresco, W.M. Reichert, Response of brain tissue to chronically implanted neural electrodes, J Neurosci Methods 148(1) (2005) 1-18.

[23] J.W. Jeong, G. Shin, S.I. Park, K.J. Yu, L. Xu, J.A. Rogers, Soft materials in neuroengineering for hard problems in neuroscience, Neuron 86(1) (2015) 175-86.

[24] D.H. Kim, R. Ghaffari, N. Lu, J.A. Rogers, Flexible and stretchable electronics for biointegrated devices, Annu Rev Biomed Eng 14 (2012) 113-28.

[25] A.C. Patil, N.V. Thakor, Implantable neurotechnologies: a review of micro- and nanoelectrodes for neural recording, Med Biol Eng Comput 54(1) (2016) 23-44.

[26] I. Johnson, K. Akari, H. Liu, Nanostructured hydroxyapatite/poly(lactic-co-glycolic acid) composite coating for controlling magnesium degradation in simulated body fluid, Nanotechnology 24(37) (2013) 375103.

[27] H. Liu, The effects of surface and biomolecules on magnesium degradation and mesenchymal stem cell adhesion, J Biomed Mater Res A 99(2) (2011) 249-60.

[28] R.G. Guan, A.F. Cipriano, Z.Y. Zhao, J. Lock, D. Tie, T. Zhao, T. Cui, H. Liu, Development and Evaluation of a Magnesium-Zinc-Strontium Alloy for Biomedical Applications – Alloy Processing, Microstructure, Mechanical Properties, and Biodegradation, Materials Science and Engineering: C 33(7) (2013) 3661-3669.

[29] Y.F. Zheng, X.N. Gu, F. Witte, Biodegradable metals, Materials Science and Engineering: R: Reports 77(0) (2014) 1-34.

[30] V.K. Gupta, Intravenous magnesium for neuroprotection in acute stroke: Clinical hope versus basic neuropharmacology, Stroke 35(12) (2004) 2758-2758.

[31] J.L. Saver, C. Kidwell, M. Eckstein, S. Starkman, F.-M.P.T. Investigators, Prehospital neuroprotective therapy for acute stroke: results of the Field Administration of Stroke Therapy-Magnesium (FAST-MAG) pilot trial, Stroke 35(5) (2004) e106-8.

[32] M.A. Sebaa, S. Dhillon, H. Liu, Electrochemical deposition and evaluation of electrically conductive polymer coating on biodegradable magnesium implants for neural applications, J Mater Sci Mater Med 24(2) (2013) 307-16.

[33] M. Sebaa, T.Y. Nguyen, S. Dhillon, S. Garcia, H. Liu, The effects of poly(3,4-ethylenedioxythiophene) coating on magnesium degradation and cytocompatibility with human embryonic stem cells for potential neural applications, J Biomed Mater Res A 103(1) (2015) 25-37.

[34] X. Luo, X.T. Cui, Electrochemical deposition of conducting polymer coatings on magnesium surfaces in ionic liquid, Acta Biomater 7(1) (2011) 441-6.

[35] S.M. Richardson-Burns, J.L. Hendricks, B. Foster, L.K. Povlich, D.H. Kim, D.C. Martin, Polymerization of the conducting polymer poly(3,4-ethylenedioxythiophene) (PEDOT) around living neural cells, Biomaterials 28(8) (2007) 1539-52.

[36] S.C. Luo, E. Mohamed Ali, N.C. Tansil, H.H. Yu, S. Gao, E.A. Kantchev, J.Y. Ying, Poly(3,4-ethylenedioxythiophene) (PEDOT) nanobiointerfaces: thin, ultrasmooth, and functionalized PEDOT films with in vitro and in vivo biocompatibility, Langmuir 24(15) (2008) 8071-7.

[37] X.Y. Cui, D.C. Martin, Electrochemical deposition and characterization of poly(3,4-ethylenedioxythiophene) on neural microelectrode arrays, Sensors and Actuators B-Chemical 89(1-2) (2003) 92-102.

[38] M.G. Urbanchek, B.S. Shim, Z. Baghmanli, B. Wei, K. Schroeder, N.B. Langhals, R.M. Miriani, B.M. Egeland, D.R. Kipke, D.C. Martin, P.S. Cederna, Conduction Properties Of Decellularized Nerve Biomaterials, IFMBE Proc 32 (2010) 430-433.

[39] S. Venkatraman, J. Hendricks, Z.A. King, A.J. Sereno, S. Richardson-Burns, D. Martin, J.M. Carmena, In vitro and in vivo evaluation of PEDOT microelectrodes for neural stimulation and recording, IEEE Trans Neural Syst Rehabil Eng 19(3) (2011) 307-16.

[40] M.A. Green, L.E. Bilston, R. Sinkus, In vivo brain viscoelastic properties measured by magnetic resonance elastography, NMR Biomed 21(7) (2008) 755-64.

[41] K. Narita, E. Kobayashi, T. Sato, Sintering Behavior and Mechanical Properties of Magnesium/β-Tricalcium Phosphate Composites Sintered by Spark Plasma Sintering, Materials Transactions 57(9) (2016) 1620-1627.

[42] C.E. Wen, M. Mabuchi, Y. Yamada, K. Shimojima, Y. Chino, T. Asahina, Processing of biocompatible porous Ti and Mg, Scripta Materialia 45(10) (2001) 1147-1153.

[43] C. Li, H. Bai, G. Shi, Conducting polymer nanomaterials: electrosynthesis and applications, Chem Soc Rev 38(8) (2009) 2397-409.

[44] S. Sadki, P. Schottland, N. Brodie, G. Sabouraud, The mechanisms of pyrrole electropolymerization, Chem. Soc. Rev. 29(5) (2000) 283-293.

[45] J. Roncali, CONJUGATED POLY(THIOPHENES) - SYNTHESIS, FUNCTIONALIZATION, AND APPLICATIONS, Chem. Rev. 92(4) (1992) 711-738.

[46] P. Audebert, P. Hapiot, Fast electrochemical studies of the polymerization mechanisms of pyrroles and thiophenes. Identification of the first steps. Existence of pi-dimers in solution, Synth. Met. 75(2) (1995) 95-102.

[47] H. Natter, R. Hempelmann, Nanocrystalline copper by pulsed electrodeposition: The effects of organic additives, bath temperature, and pH, J Phys Chem-Us 100(50) (1996) 19525-19532.

[48] I. Johnson, S.M. Wang, C. Silken, H. Liu, A systemic study on key parameters affecting nanocomposite coatings on magnesium substrates, Acta Biomater 36 (2016) 332-49.

[49] Artificial cerebrospinal fluid (ACSF), Cold Spring Harbor Protocols 2011(9) (2011) pdb.rec065730.

[50] X.S. Wang, H.P. Tang, X.D. Li, X. Hua, Investigations on the Mechanical Properties of Conducting Polymer Coating-Substrate Structures and Their Influencing Factors, International Journal of Molecular Sciences 10(12) (2009) 5257-5284.

[51] C.S. Suchand Sangeeth, M. Jaiswal, R. Menon, Correlation of morphology and charge transport in poly(3,4-ethylenedioxythiophene)-polystyrenesulfonic acid (PEDOT-PSS) films, J Phys Condens Matter 21(7) (2009) 072101.

[52] T. Ware, D. Simon, D.E. Arreaga-Salas, J. Reeder, R. Rennaker, E.W. Keefer, W. Voit, Fabrication of Responsive, Softening Neural Interfaces, Adv. Funct. Mater. 22(16) (2012) 3470-3479.

[53] G.H. Borschel, K.F. Kia, W.M. Kuzon, Jr., R.G. Dennis, Mechanical properties of acellular peripheral nerve, J Surg Res 114(2) (2003) 133-9.

[54] A.B. Mathur, A.M. Collinsworth, W.M. Reichert, W.E. Kraus, G.A. Truskey, Endothelial, cardiac muscle and skeletal muscle exhibit different viscous and elastic properties as determined by atomic force microscopy, Journal of Biomechanics 34(12) (2001) 1545-1553.

[55] A.R. Harris, S.J. Morgan, J. Chen, R.M.I. Kapsa, G.G. Wallace, A.G. Paolini, Conducting polymer coated neural recording electrodes, Journal of Neural Engineering 10(1) (2013).

[56] S.F. Cogan, Neural stimulation and recording electrodes, Annual Review of Biomedical Engineering 10 (2008) 275-309.

[57] B.S. Kim, B. Kim, K.D. Suh, Electrorheological properties of carbon nanotube/polyelectrolyte self-assembled polystyrene particles by layer-by-layer assembly, J Polym Sci Pol Chem 46(3) (2008) 1058-1065.

[58] M.P. Ward, P. Rajdev, C. Ellison, P.P. Irazoqui, Toward a comparison of microelectrodes for acute and chronic recordings, Brain Res 1282 (2009) 183-200.

[59] Y.S. Singh, L.E. Sawarynski, P.D. Dabiri, W.R. Choi, A.M. Andrews, Head-to-Head Comparisons of Carbon Fiber Microelectrode Coatings for Sensitive and Selective Neurotransmitter Detection by Voltammetry, Anal Chem 83(17) (2011) 6658-6666.

[60] S. Gupta, G. Huang, H.B. Lu, A.A. Mamedov, Characterization of layer-by-layer assembled carbon nanotube/polyelectrolyte films., Abstr Pap Am Chem S 229 (2005) U942-U942.

[61] E. Jan, J.L. Hendricks, V. Husaini, S.M. Richardson-Burns, A. Sereno, D.C. Martin, N.A. Kotov, Layered Carbon Nanotube-Polyelectrolyte Electrodes Outperform Traditional Neural Interface Materials, Nano Letters 9(12) (2009) 4012-4018.

[62] B. Kumar, Y.T. Park, M. Castro, J.C. Grunlan, J.F. Feller, Fine control of carbon nanotubes-polyelectrolyte sensors sensitivity by electrostatic layer by layer assembly (eLbL) for the detection of volatile organic compounds (VOC), Talanta 88 (2012) 396-402.

[63] Y. Tian, J.G. Park, Q.F. Cheng, Z.Y. Liang, C. Zhang, B. Wang, The fabrication of single-walled carbon nanotube/polyelectrolyte multilayer composites by layer-by-layer assembly and magnetic field assisted alignment, Nanotechnology 20(33) (2009).

[64] D.Z. Zhang, K. Wang, J. Tong, B.K. Xia, Layer-by-Layer Nanoassembly Fabrication and Humidity Sensing Behaviors of Multi-Walled Carbon Nanotubes/Polyelectrolyte Hybrid Film, Journal of Nanoscience and Nanotechnology 16(7) (2016) 6705-6710.

[65] S.F. Cogan, A.A. Guzelian, W.F. Agnew, T.G.H. Yuen, D.B. McCreery, Over-pulsing degrades activated iridium oxide films used for intracortical neural stimulation, J Neurosci Meth 137(2) (2004) 141-150.

[66] S. Negi, R. Bhandari, L. Rieth, R. Van Wagenen, F. Solzbacher, Neural electrode degradation from continuous electrical stimulation: Comparison of sputtered and activated iridium oxide, J Neurosci Meth 186(1) (2010) 8-17.

[67] D.J. Garrett, K. Ganesan, A. Stacey, K. Fox, H. Meffin, S. Prawer, Ultra-nanocrystalline diamond electrodes: optimization towards neural stimulation applications, Journal of Neural Engineering 9(1) (2012).

[68] M. Irimia-Vladu, "Green" electronics: biodegradable and biocompatible materials and devices for sustainable future (vol 43, pg 588, 2014), Chem. Soc. Rev. 43(17) (2014) 6470-6470.

[69] M. Irimia-Vladu, E.D. Glowacki, G. Voss, S. Bauer, N.S. Sariciftci, Green and biodegradable electronics, Materials Today 15(7-8) (2012) 340-346.

[70] D.H. Kim, N.S. Lu, R. Ma, Y.S. Kim, R.H. Kim, S.D. Wang, J. Wu, S.M. Won, H. Tao, A. Islam, K.J. Yu, T.I. Kim, R. Chowdhury, M. Ying, L.Z. Xu, M. Li, H.J. Chung, H. Keum, M. McCormick, P. Liu, Y.W. Zhang, F.G. Omenetto, Y.G. Huang, T. Coleman, J.A. Rogers, Epidermal Electronics, Science 333(6044) (2011) 838-843.

[71] S.K. Kang, R.K.J. Murphy, S.W. Hwang, S.M. Lee, D.V. Harburg, N.A. Krueger, J.H. Shin, P. Gamble, H.Y. Cheng, S. Yu, Z.J. Liu, J.G. McCall, M. Stephen, H.Z. Ying, J. Kim, G. Park, R.C. Webb, C.H. Lee, S.J. Chung, D.S. Wie, A.D. Gujar, B. Vemulapalli, A.H. Kim, K.M. Lee, J.J. Cheng, Y.G. Huang, S.H. Lee, P.V. Braun, W.Z. Ray, J.A. Rogers, Bioresorbable silicon electronic sensors for the brain, Nature 530(7588) (2016) 71-+.

[72] S.W. Hwang, J.K. Song, X. Huang, H.Y. Cheng, S.K. Kang, B.H. Kim, J.H. Kim, S. Yu, Y.G. Huang, J.A. Rogers, High-Performance Biodegradable/Transient Electronics on Biodegradable Polymers, Advanced Materials 26(23) (2014) 3905-3911.

[73] D.H. Kim, J. Viventi, J.J. Amsden, J.L. Xiao, L. Vigeland, Y.S. Kim, J.A. Blanco, B. Panilaitis, E.S. Frechette, D. Contreras, D.L. Kaplan, F.G. Omenetto, Y.G. Huang, K.C. Hwang, M.R. Zakin, B. Litt, J.A. Rogers, Dissolvable films of silk fibroin for ultrathin conformal bio-integrated electronics, Nat Mater 9(6) (2010) 511-517.

[74] C.X. Zhang, J.J. Lin, H.N. Liu, Magnesium-based Biodegradable Materials for Biomedical Applications, Mrs Adv 3(40) (2018) 2359-2364.

[75] I. Johnson, H. Liu, A study on factors affecting the degradation of magnesium and a magnesium-yttrium alloy for biomedical applications, PLoS One 8(6) (2013) e65603.

[76] A.F. Cipriano, A. Sallee, R.-G. Guan, Z.-Y. Zhao, M. Tayoba, J. Sanchez, H. Liu, Investigation of magnesium-zinc-calcium alloys and bone marrow derived mesenchymal stem cell response in direct culture, Acta Biomaterialia 12 (2015) 298-321.

[77] L. Liu, N. Li, T. Lei, K. Li, Y. Zhang, The in vitro biological properties of Mg-Zn-Sr alloy and superiority for preparation of biodegradable intestinal anastomosis rings, Medical Science Monitor 20 (2014) 1056-1066.

[78] A.H.M. Sanchez, B.J.C. Luthringer, F. Feyerabend, R. Willumeit, Mg and Mg alloys: How comparable are in vitro and in vivo corrosion rates? A review, Acta Biomater 13 (2015) 16-31.

[79] F. Gao, C.Y. Xu, H.T. Hu, Q. Wang, Y.Y. Gao, H. Chen, Q.N. Guo, D.Z. Chen, D. Eder, Biomimetic synthesis and characterization of hydroxyapatite/graphene oxide hybrid coating on Mg alloy with enhanced corrosion resistance, Mater Lett 138 (2015) 25-28.

[80] W. Jiang, A.F. Cipriano, Q. Tian, C. Zhang, M. Lopez, A. Sallee, A. Lin, M.C. Cortez Alcaraz, Y. Wu, Y. Zheng, H. Liu, In vitro evaluation of MgSr and MgCaSr alloys via direct culture with bone marrow derived mesenchymal stem cells, Acta Biomater 72 (2018) 407-423.

[81] Q.M. Tian, C.X. Zhang, M. Deo, L. Rivera-Castaneda, N. Masoudipour, R.G. Guan, H.N. Liu, Responses of human urothelial cells to magnesium-zinc-strontium alloys and associated insoluble degradation products for urological stent applications, Mater Sci Eng C Mater Biol Appl 96 (2019) 248-262.

[82] K. Narita, Q. Tian, I. Johnson, C. Zhang, E. Kobayashi, H. Liu, Degradation behaviors and cytocompatibility of Mg/β-tricalcium phosphate composites produced by spark plasma sintering, J Biomed Mater Res B 9999B (2019) 1-16.

[83] J.L. Saver, C. Kidwell, M. Eckstein, S. Starkman, F.-M.P.T. Investigators, Prehospital neuroprotective therapy for acute stroke - Results of the field administration of stroke therapy-magnesium (FAST-MAG) pilot trial, Stroke 35(5) (2004) E106-E108.

[84] J. Qu, L. Ouyang, C.C. Kuo, D.C. Martin, Stiffness, strength and adhesion characterization of electrochemically deposited conjugated polymer films, Acta Biomater 31 (2016) 114-121.

[85] C.A. Sundback, J.Y. Shyu, Y.D. Wang, W.C. Faquin, R.S. Langer, J.P. Vacanti, T.A. Hadlock, Biocompatibility analysis of poly(glycerol sebacate) as a nerve guide material, Biomaterials 26(27) (2005) 5454-5464.

[86] R. Rai, M. Tallawi, A. Grigore, A.R. Boccaccini, Synthesis, properties and biomedical applications of poly(glycerol sebacate) (PGS): A review, Progress in Polymer Science 37(8) (2012) 1051-1078.

[87] A.F. Cipriano, T. Zhao, I. Johnson, R.-G. Guan, S. Garcia, H. Liu, In vitro degradation of four magnesium-zinc-strontium alloys and their cytocompatibility with human embryonic stem cells, J Mater Sci Mater Med 24(4) (2013) 989-1003.

[88] L. Cheng, K. Yang, Q. Chen, Z. Liu, Organic Stealth Nanoparticles for Highly Effective in Vivo Near-Infrared Photothermal Therapy of Cancer, Acs Nano 6(6) (2012) 5605-5613.

[89] D. Alemu, H.Y. Wei, K.C. Ho, C.W. Chu, Highly conductive PEDOT:PSS electrode by simple film treatment with methanol for ITO-free polymer solar cells, Energ Environ Sci 5(11) (2012) 9662-9671.

[90] C.X. Zhang, N. Driver, Q.M. Tian, W.S. Jiang, H.N. Liu, Electrochemical deposition of conductive polymers onto magnesium microwires for neural electrode applications, J Biomed Mater Res A 106(7) (2018) 1887-1895.

[91] Y.D. Wang, G.A. Ameer, B.J. Sheppard, R. Langer, A tough biodegradable elastomer, Nature Biotechnology 20(6) (2002) 602-606.

[92] T.H. Wen, S. Afroz, S.M. Reinhard, A.R. Palacios, K. Tapia, D.K. Binder, K.A. Razak, I.M. Ethell, Genetic Reduction of Matrix Metalloproteinase-9 Promotes Formation of Perineuronal Nets Around Parvalbumin-Expressing Interneurons and Normalizes Auditory Cortex Responses in Developing Fmr1 Knock-Out Mice, Cerebral Cortex 28(11) (2018) 3951-3964.

[93] S. Rotschafer, K. Razak, Altered auditory processing in a mouse model of fragile X syndrome, Brain Res 1506 (2013) 12-24.

[94] J.D. Weiland, D.J. Anderson, M.S. Humayun, In vitro electrical properties for iridium oxide versus titanium nitride stimulating electrodes, Ieee T Bio-Med Eng 49(12) (2002) 1574-1579.

[95] J.Y. Yang, D.H. Kim, J.L. Hendricks, M. Leach, R. Northey, D.C. Martin, Ordered surfactant-templated poly(3,4-ethylenedioxythiophene) (PEDOT) conducting polymer on microfabricated neural probes, Acta Biomater 1(1) (2005) 125-136.

[96] S. Yaeli, E. Binyamin, S. Shoham, Form-function relations in cone-tipped stimulating microelectrodes, Frontiers in Neuroengineering 2(13) (2009).

[97] M. Sessolo, D. Khodagholy, J. Rivnay, F. Maddalena, M. Gleyzes, E. Steidl, B. Buisson, G.G. Malliaras, Easy-to-Fabricate Conducting Polymer Microelectrode Arrays, Advanced Materials 25(15) (2013) 2135-2139.

[98] K.A. Ludwig, J.D. Uram, J.Y. Yang, D.C. Martin, D.R. Kipke, Chronic neural recordings using silicon microelectrode arrays electrochemically deposited with a poly(3,4-ethylenedioxythiophene) (PEDOT) film, Journal of Neural Engineering 3(1) (2006) 59-70.

[99] X.T. Cul, D.D. Zhou, Poly (3,4-ethylenedioxythiophene) for chronic neural stimulation, Ieee T Neur Sys Reh 15(4) (2007) 502-508.

[100] J. Rae, K. Cooper, P. Gates, M. Watsky, Low Access Resistance Perforated Patch Recordings Using Amphotericin-B, J Neurosci Meth 37(1) (1991) 15-26.

[101] R.M. Miriani, M.R. Abidian, D.R. Kipke, Cytotoxic Analysis of the Conducting Polymer PEDOT using Myocytes, Ieee Eng Med Bio (2008) 1841-1844.

[102] M. Asplund, E. Thaning, J. Lundberg, A.C. Sandberg-Nordqvist, B. Kostyszyn, O. Inganas, H. von Holst, Toxicity evaluation of PEDOT/biomolecular composites intended for neural communication electrodes, Biomedical Materials 4(4) (2009).

[103] S.-C. Luo, E.M. Ali, N.C. Tansil, H.-H. Yu, S. Gao, E.A.B. Kantchev, J.Y. Ying, Poly(3,4-ethylenedioxythiophene) (PEDOT) nanobiointerfaces: Thin, ultrasmooth, and functionalized PEDOT films with in vitro and in vivo biocompatibility, Langmuir 24(15) (2008) 8071-8077.

[104] X. Luo, X.T. Cui, Electrochemical deposition of conducting polymer coatings on magnesium surfaces in ionic liquid, Acta Biomater 7(1) (2011) 441-446.

[105] M.G. Urbanchek, B.S. Shim, Z. Baghmanli, B. Wei, K. Schroeder, N.B. Langhals, R.M. Miriani, B.M. Egeland, D.R. Kipke, D.C. Martin, P.S. Cederna, Conduction Properties Of Decellularized Nerve Biomaterials, in: K.E. Herold, W.E. Bentley, J. Vossoughi (Eds.), 26th Southern Biomedical Engineering Conference: Sbec 20102010, pp. 430-+.

[106] R.A. Green, R.T. Hassarati, J.A. Goding, S. Baek, N.H. Lovell, P.J. Martens, L.A. Poole-Warren, Conductive Hydrogels: Mechanically Robust Hybrids for Use as Biomaterials, Macromolecular Bioscience 12(4) (2012) 494-501.

[107] L.M. Yee, H.N.M.E. Mahmud, A. Kassim, W.M.M. Yunus, Polypyrrole-polyethylene glycol conducting polymer composite films: Preparation and characterization, Synth. Met. 157(8-9) (2007) 386-389.

[108] R.A. Allen, W. Wu, M.Y. Yao, D. Dutta, X.J. Duan, T.N. Bachman, H.C. Champion, D.B. Stolz, A.M. Robertson, K. Kim, J.S. Isenberg, Y.D. Wang, Nerve regeneration and elastin formation within poly(glycerol sebacate)-based synthetic arterial grafts one-year post-implantation in a rat model, Biomaterials 35(1) (2014) 165-173.

[109] Q.Z. Chen, A. Bismarck, U. Hansen, S. Junaid, M.Q. Tran, S.E. Harding, N.N. Ali, A.R. Boccaccini, Characterisation of a soft elastomer poly(glycerol sebacate) designed to match the mechanical properties of myocardial tissue, Biomaterials 29(1) (2008) 47-57.

[110] Q.Z. Chen, H. Ishii, G.A. Thouas, A.R. Lyon, J.S. Wright, J.J. Blaker, W. Chrzanowski, A.R. Boccaccini, N.N. Ali, J.C. Knowles, S.E. Harding, An elastomeric patch derived from poly(glycerol sebacate) for delivery of embryonic stem cells to the heart, Biomaterials 31(14) (2010) 3885-3893.

[111] J. Gao, A.E. Ensley, R.M. Nerem, Y.D. Wang, Poly(glycerol sebacate) supports the proliferation and phenotypic protein expression of primary baboon vascular cells, J Biomed Mater Res A 83A(4) (2007) 1070-1075.

[112] J. Hu, D. Kai, H.Y. Ye, L.L. Tian, X. Ding, S. Ramakrishna, X.J. Loh, Electrospinning of poly(glycerol sebacate)-based nanofibers for nerve tissue engineering, Mater Sci Eng C Mater Biol Appl 70 (2017) 1089-1094.

[113] Y.T. Jia, W.Z. Wang, X.J. Zhou, W. Nie, L. Chen, C.L. He, Synthesis and characterization of poly(glycerol sebacate)-based elastomeric copolyesters for tissue engineering applications, Polymer Chemistry 7(14) (2016) 2553-2564.

[114] X.J. Loh, A.A. Karim, C. Owh, Poly(glycerol sebacate) biomaterial: synthesis and biomedical applications, Journal of Materials Chemistry B 3(39) (2015) 7641-7652.

[115] X.L. Zhang, C.L. Jia, X.Y. Qiao, T.Y. Liu, K. Sun, Porous poly(glycerol sebacate) (PGS) elastomer scaffolds for skin tissue engineering, Polymer Testing 54 (2016) 118-125.

[116] F. Yi, D.A. Lavan, Poly(glycerol sebacate) nanofiber scaffolds by core/shell electrospinning, Macromolecular Bioscience 8(9) (2008) 803-806.

[117] Y.D. Wang, Y.M. Kim, R. Langer, In vivo degradation characteristics of poly(glycerol sebacate), J Biomed Mater Res A 66A(1) (2003) 192-197.

[118] H. Zhang, M.W. Grinstaff, Recent Advances in Glycerol Polymers: Chemistry and Biomedical Applications, Macromol Rapid Comm 35(22) (2014) 1906-1924.

[119] G.G. Lang, M. Ujvari, S. Vesztergom, V. Kondratiev, J. Gubicza, K.J. Szekeres, The Electrochemical Degradation of Poly(3,4-ethylenedioxythiophene) Films Electrodeposited from Aqueous Solutions, Z Phys Chem 230(9) (2016) 1281-1302.

[120] M. Ujvari, G.G. Lang, S. Vesztergom, K.J. Szekeres, N. Kovacs, J. Gubicza, Structural changes during the overoxidation of electrochemically deposited poly(3,4-ethylenedioxythiophene) films, J Electrochem Sci En 6(1) (2016) 77-88.

[121] M.P. Staiger, A.M. Pietak, J. Huadmai, G. Dias, Magnesium and its alloys as orthopedic biomaterials: a review, Biomaterials 27(9) (2006) 1728-1734.

[122] F. Witte, N. Hort, C. Vogt, S. Cohen, K.U. Kainer, R. Willumeit, F. Feyerabend, Degradable biomaterials based on magnesium corrosion, Current Opinion in Solid State & Materials Science 12(5-6) (2008) 63-72.

[123] A.F. Cipriano, R.-G. Guan, T. Cui, Z.-Y. Zhao, S. Garcia, I. Johnson, H. Liu, Ieee, In vitro Degradation and Cytocompatibility of Magnesium-Zinc-Strontium Alloys with Human Embryonic Stem Cells, 2012 Annual International Conference of the Ieee Engineering in Medicine and Biology Society2012, pp. 2432-2435.

[124] H. Waizy, J.-M. Seitz, J. Reifenrath, A. Weizbauer, F.-W. Bach, A. Meyer-Lindenberg, B. Denkena, H. Windhagen, Biodegradable magnesium implants for orthopedic applications, Journal of Materials Science 48(1) (2013) 39-50.

[125] R.-g. Guan, A.F. Cipriano, Z.-y. Zhao, J. Lock, D. Tie, T. Zhao, T. Cui, H. Liu, Development and evaluation of a magnesium-zinc-strontium alloy for biomedical applications - Alloy processing, microstructure, mechanical properties, and biodegradation, Materials Science & Engineering C-Materials for Biological Applications 33(7) (2013) 3661-3669.

[126] M. Peron, J. Torgersen, F. Berto, Mg and Its Alloys for Biomedical Applications: Exploring Corrosion and Its Interplay with Mechanical Failure, Metals-Basel 7(7) (2017).

[127] C. Zhang, N. Driver, Q. Tian, W. Jiang, H. Liu, Electrochemical deposition of conductive polymers onto magnesium microwires for neural electrode applications, Journal of Biomedical Materials Research Part A 106(7) (2018) 1887-1895.

[128] Y.F. Zheng, X.N. Gu, F. Witte, Biodegradable metals, Materials Science & Engineering R-Reports 77 (2014) 1-34.

[129] Y.F. Ding, C.E. Wen, P. Hodgson, Y.C. Li, Effects of alloying elements on the corrosion behavior and biocompatibility of biodegradable magnesium alloys: a review, Journal of Materials Chemistry B 2(14) (2014) 1912-1933.

[130] S.S. Abd El-Rahman, Neuropathology of aluminum toxicity in rats (glutamate and GABA impairment), Pharmacol Res 47(3) (2003) 189-194.

[131] H. Li, Q. Peng, X. Li, K. Li, Z. Han, D. Fang, Microstructures, mechanical and cytocompatibility of degradable Mg-Zn based orthopedic biomaterials, Materials & Design 58 (2014) 43-51.

[132] Y. Jeong, W. Kim, Enhancement of mechanical properties and corrosion resistance of Mg–Ca alloys through microstructural refinement by indirect extrusion, Corrosion Science 82 (2014) 392-403.

[133] S.Y. Cho, S.-W. Chae, K.W. Choi, H.K. Seok, Y.C. Kim, J.Y. Jung, S.J. Yang, G.J. Kwon, J.T. Kim, M. Assad, Biocompatibility and strength retention of biodegradable Mg-Ca-Zn alloy bone implants, Journal of Biomedical Materials Research Part B-Applied Biomaterials 101B(2) (2013) 201-212.

[134] B. Wang, J. Gao, L. Wang, S. Zhu, S. Guan, Biocorrosion of coated Mg-Zn-Ca alloy under constant compressive stress close to that of human tibia, Mater Lett 70 (2012) 174-176.

[135] H.S. Brar, J. Wong, M.V. Manuel, Investigation of the mechanical and degradation properties of Mg-Sr and Mg-Zn-Sr alloys for use as potential biodegradable implant materials, Journal of the Mechanical Behavior of Biomedical Materials 7 (2012) 87-95.

[136] H.R. Bakhsheshi-Rad, M.R. Abdul-Kadir, M.H. Idris, S. Farahany, Relationship between the corrosion behavior and the thermal characteristics and microstructure of Mg-0.5Ca-xZn alloys, Corrosion Science 64 (2012) 184-197.

[137] B. Zhang, Y. Hou, X. Wang, Y. Wang, L. Geng, Mechanical properties, degradation performance and cytotoxicity of Mg-Zn-Ca biomedical alloys with different compositions, Mater Sci Eng C Mater Biol Appl 31(8) (2011) 1667-1673.

[138] Z. Xu, C. Smith, S. Chen, J. Sankar, Development and microstructural characterizations of Mg-Zn-Ca alloys for biomedical applications, Materials Science and Engineering B-Advanced Functional Solid-State Materials 176(20) (2011) 1660-1665.

[139] J.E. Coleman, Zinc Proteins - Enzymes, Storage Proteins, Transcription Factors, and Replication Proteins, Annual Review of Biochemistry 61 (1992) 897-946.

[140] S. Farahany, H.R. Bakhsheshi-Rad, M.H. Idris, M.R.A. Kadir, A.F. Lotfabadi, A. Ourdjini, In-situ thermal analysis and macroscopical characterization of Mg-xCa and Mg-0.5Ca-xZn alloy systems, Thermochimica Acta 527 (2012) 180-189.

[141] C.J. Boehlert, K. Knittel, The microstructure, tensile properties, and creep behavior of Mg-Zn alloys containing 0-4.4 wt.% Zn, Materials Science and Engineering a-Structural Materials Properties Microstructure and Processing 417(1-2) (2006) 315-321.

[142] B.P. Zhang, Y. Wang, L. Geng, Research on Mg-Zn-Ca Alloy as Degradable Biomaterial, Biomaterials - Physics and Chemistry (2011) 183-204.

[143] F. Rosalbino, S. De Negri, A. Saccone, E. Angelini, S. Delfino, Bio-corrosion characterization of Mg-Zn-X (X = Ca, Mn, Si) alloys for biomedical applications, J Mater Sci Mater Med 21(4) (2010) 1091-1098.

[144] Y. Sun, B. Zhang, Y. Wang, L. Geng, X. Jiao, Preparation and characterization of a new biomedical Mg-Zn-Ca alloy, Materials & Design 34 (2012) 58-64.

[145] P. Yin, N.F. Li, T. Lei, L. Liu, C. Ouyang, Effects of Ca on microstructure, mechanical and corrosion properties and biocompatibility of Mg-Zn-Ca alloys, J Mater Sci Mater Med 24(6) (2013) 1365-1373.

[146] E. Zhang, L. Yang, Microstructure, mechanical properties and bio-corrosion properties of Mg-Zn-Mn-Ca alloy for biomedical application, Materials Science and Engineering a-Structural Materials Properties Microstructure and Processing 497(1-2) (2008) 111-118.

[147] Y.C. Li, M.H. Li, W.Y. Hu, P. Hodgson, C. Wen, Biodegradable Mg-Ca and Mg-Ca-Y alloys for Regenerative Medicine, Mater Sci Forum 654-656 (2010) 2192-+.

[148] Z.J. Li, X.N. Gu, S.Q. Lou, Y.F. Zheng, The development of binary Mg-Ca alloys for use as biodegradable materials within bone, Biomaterials 29(10) (2008) 1329-1344.

[149] Q.M. Tian, M. Deo, L. Rivera-Castaneda, H.N. Liu, Cytocompatibility of Magnesium Alloys with Human Urothelial Cells: A Comparison of Three Culture Methodologies, Acs Biomater Sci Eng 2(9) (2016) 1559-1571.

[150] Y.K. Pan, S.Y. He, D.G. Wang, D.L. Huang, T.T. Zheng, S.Q. Wang, P. Dong, C.Z. Chen, In vitro degradation and electrochemical corrosion evaluations of microarc oxidized pure Mg, Mg-Ca and Mg-Ca-Zn alloys for biomedical applications, Mater Sci Eng C Mater Biol Appl 47 (2015) 85-96.

[151] Y. Lu, A.R. Bradshaw, Y.L. Chiu, I.P. Jones, Effects of secondary phase and grain size on the corrosion of biodegradable Mg-Zn-Ca alloys, Mater Sci Eng C Mater Biol Appl 48 (2015) 480-486.

[152] J. Hofstetter, E. Martinelli, S. Pogatscher, P. Schmutz, E. Povoden-Karadeniz, A.M. Weinberg, P.J. Uggowitzer, J.F. Loffler, Influence of trace impurities on the in vitro and in vivo degradation of biodegradable Mg-5Zn-0.3Ca alloys, Acta Biomater 23 (2015) 347-353.

[153] M. Ramya, S.G. Sarwat, V. Udhayabanu, S. Subramanian, B. Raj, K.R. Ravi, Role of partially amorphous structure and alloying elements on the corrosion behavior of Mg-Zn-Ca bulk metallic glass for biomedical applications, Materials & Design 86 (2015) 829-835.

[154] J.W. Lee, H.S. Han, K.J. Han, J. Park, H. Jeon, M.R. Ok, H.K. Seok, J.P. Ahn, K.E. Lee, D.H. Lee, S.J. Yang, S.Y. Cho, P.R. Cha, H. Kwon, T.H. Nam, J.H. Lo Han, H.J. Rho, K.S. Lee, Y.C. Kim, D. Mantovani, Long-term clinical study and multiscale analysis of in vivo biodegradation mechanism of Mg alloy, Proceedings of the National Academy of Sciences of the United States of America 113(3) (2016) 716-721.

[155] D. Bian, W.R. Zhou, Y. Liu, N. Li, Y.F. Zheng, Z.L. Sun, Fatigue behaviors of HP-Mg, Mg-Ca and Mg-Zn-Ca biodegradable metals in air and simulated body fluid, Acta Biomater 41 (2016) 351-360.

[156] H. Li, D.B. Liu, Y. Zhao, F. Jin, M.F. Chen, The Influence of Zn Content on the Corrosion and Wear Performance of Mg-Zn-Ca Alloy in Simulated Body Fluid, J Mater Eng Perform 25(9) (2016) 3890-3895.

[157] C.Z. Zhang, S.J. Zhu, L.G. Wang, R.M. Guo, G.C. Yue, S.K. Guan, Microstructures and degradation mechanism in simulated body fluid of biomedical Mg-Zn-Ca alloy processed by high pressure torsion, Materials & Design 96 (2016) 54-62.

[158] V. Roche, G.Y. Koga, T.B. Matias, C.S. Kiminami, C. Bolfarini, W.J. Botta, R.P. Nogueira, A.M. Jorge, Degradation of biodegradable implants: The influence of microstructure and composition of Mg-Zn-Ca alloys, Journal of Alloys and Compounds 774 (2019) 168-181.

[159] X.N. Gu, F. Wang, X.H. Xie, M.Y. Zheng, P. Li, Y.F. Zheng, L. Qin, Y.B. Fan, In vitro and in vivo studies on as- extruded Mg-5.25 wt.% Zn-0.6wt.% Ca alloy as biodegradable metal, Sci China Mater 61(4) (2018) 619-628.

[160] A.F. Cipriano, A. Sallee, M. Tayoba, M.C.C. Alcaraz, A. Lin, R.G. Guan, Z.Y. Zhao, H.N. Liu, Cytocompatibility and early inflammatory response of human endothelial cells in direct culture with Mg-Zn-Sr alloys, Acta Biomater 48 (2017) 499-520.

[161] T.Y. Nguyen, A.F. Cipriano, R.-G. Guan, Z.-Y. Zhao, H. Liu, In vitro interactions of blood, platelet, and fibroblast with biodegradable magnesium-zinc-strontium alloys, J Biomed Mater Res A 103(9) (2015) 2974-2986.

[162] X. Gu, Y. Zheng, Y. Cheng, S. Zhong, T. Xi, In vitro corrosion and biocompatibility of binary magnesium alloys, Biomaterials 30(4) (2009) 484-498.

[163] C.L. Wetteland, N.Y. Nguyen, H. Liu, Concentration-dependent behaviors of bone marrow derived mesenchymal stem cells and infectious bacteria toward magnesium oxide nanoparticles, Acta Biomater 35 (2016) 341-56.

[164] C.L. Wetteland, N.-Y.T. Nguyen, H.J.A.b. Liu, Concentration-dependent behaviors of bone marrow derived mesenchymal stem cells and infectious bacteria toward magnesium oxide nanoparticles, 35 (2016) 341-356.

[165] N.Y.T. Nguyen, N. Grelling, C.L. Wetteland, R. Rosario, H.N. Liu, Antimicrobial Activities and Mechanisms of Magnesium Oxide Nanoparticles (nMgO) against Pathogenic Bacteria, Yeasts, and Biofilms, Sci Rep 8 (2018).

[166] M.J. Berridge, P. Lipp, M.D. Bootman, The versatility and universality of calcium signalling, Nat Rev Mol Cell Bio 1(1) (2000) 11-21.

[167] G. Song, Control of biodegradation of biocompatable magnesium alloys, Corrosion Science 49(4) (2007) 1696-1701.

[168] P.R. Cha, H.S. Han, G.F. Yang, Y.C. Kim, K.H. Hong, S.C. Lee, J.Y. Jung, J.P. Ahn, Y.Y. Kim, S.Y. Cho, J.Y. Byun, K.S. Lee, S.J. Yang, H.K. Seok, Biodegradability engineering of biodegradable Mg alloys: Tailoring the electrochemical properties and microstructure of constituent phases, Sci Rep 3 (2013).